Flow and Heat Transfer of Impinging Synthetic Jets

Arnau Miró Jané

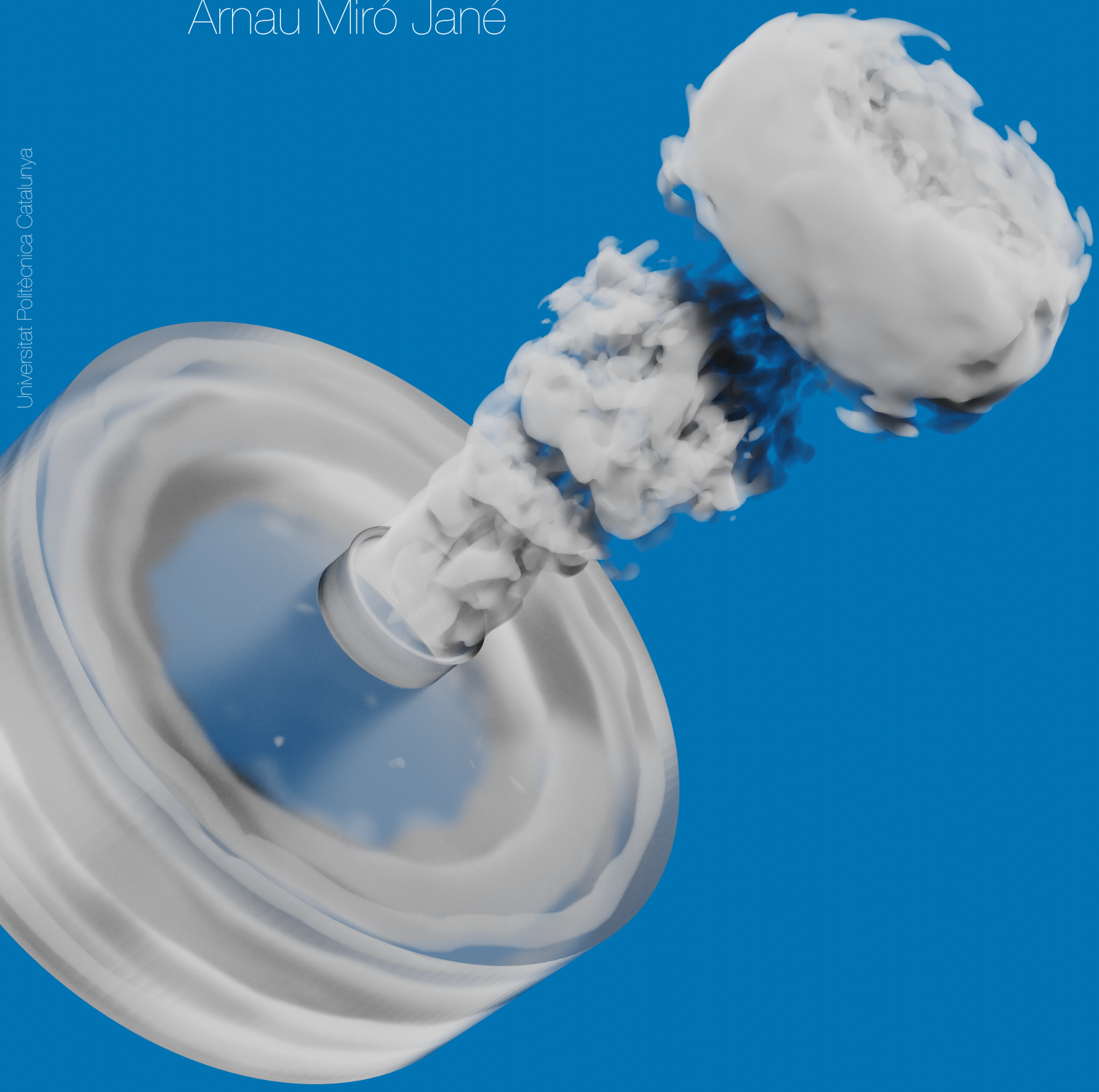

Universitat Politècnica Catalunya

UNIVERSITAT POLITÈCNICA
DE CATALUNYA
BARCELONATECH

Flow and Heat Transfer of Impinging Synthetic Jets

by

Arnau Miró Jané

Thesis submitted to obtain the doctoral degree by Universitat Politècnica de Catalunya(UPC)

Student name: **Arnau Miró Jané**
ORCID ID: 0000-0002-2772-6050
Divisió d'Enginyeria Aeroespacial (DFIS), Universitat Politècnica de Catalunya (UPC), ESEIAAT, C. Colom, 11, 08222, Terrassa, Spain

Supervisor/s: **Manel Soria Guerrero**
ORCID ID: 0000-0002-4112-6078
Divisió d'Enginyeria Aeroespacial (DFIS), Universitat Politècnica de Catalunya (UPC), ESEIAAT, C. Colom, 11, 08222, Terrassa, Spain

Juan-Carlos Cajas
ORCID ID: 0000-0002-5472-8385
Computer Applications in Science and Engineering (CASE), Barcelona Supercomputing Center (BSC), Edif. Nexus II, C. Jordi Girona, 29, 08034 Barcelona, Spain

Program: Mechanical, Fluids and Aerospace Engineering
Date: Terrassa, April 2019

CC BY NC SA

UNIVERSITAT POLITÈCNICA DE CATALUNYA BARCELONATECH

"A central lesson of science is that to understand complex issues (or even simple ones), we must try to free our minds of dogma and to guarantee the freedom to publish, to contradict, and to experiment. Arguments from authority are unacceptable."

Carl Sagan (1934 - 1996)

Abstract

Synthetic jets are produced by the oscillatory movement of a membrane inside a cavity, causing fluid to enter and leave through a small orifice. This results in a net jet that is able to transfer kinetic energy and momentum to a fluid medium without the need of an external fluid source. This is why synthetic jets are interesting and will have key roles in a wide range of relevant applications such as active flow control, thermal cooling or fuel mixing. From the phenomenological point of view, synthetic jets are formed by elaborate flow patterns given their non-linear nature and, under certain conditions, unstable complex flows can be observed.

The present dissertation is focused on the investigation of the fluid flow and thermal performance of synthetic jets. Two different synthetic jet actuator geometries (i.e., slotted and circular) are studied. The jets in both configurations are confined by two parallel isothermal plates with an imposed temperature difference, and impinge into a heated plate located at a certain distance from the actuator orifice. The unsteady three-dimensional Navier-Stokes equations are solved for a range of Reynolds numbers using time-accurate numerical simulations. Moreover, a detailed model of the actuator that uses Arbitrary Lagrangian-Eulerian (ALE) formulation to account for the movement of the actuator membrane is developed. This model, based on the governing numbers of the flow, is used to conduct the numerical analyses.

The flows obtained in both configurations are noticeably different and three-dimensional for almost all the Reynolds numbers considered. The jet in the slotted configuration is formed by a pair of vortices that undergo turbulent transition and eventually coalesce into the jet. The external flow is dominated by two major recirculation structures that find their counterparts inside the actuator cavity. A new vortical structure, observed in confined slotted jets, appears as an interaction of the synthetic jet flow with the bottom wall and results in a change on the jet's heat transfer mechanisms. On the other hand, the jet in the circular configuration presents three different flow regions that have been identified according to the literature: the main vortex ring, the trailing jet and the potential core. In this case, the external flow is dominated by the main vortex ring and the trailing jet, thus presenting a different morphology and heat transfer behavior than the slotted configuration. A detailed analysis of the vortex trajectories has shown that the advected vortices on the circular configuration reach the impingement before their slotted counterparts. Distributions of turbulent kinetic energy at the expulsion and vortex swirl and shear strength have revealed that the flow

on the circular jet is mostly concentrated near the jet centerline, while it is more spread for the slotted configuration. For these reasons, at the same jet ejection velocity and actuator geometry, synthetic jet formation on the circular configuration can occur at higher frequencies than on the slotted configuration.

The analysis of the synthetic jet outlet temperature has shown that assuming a uniform profile is reasonable if the Reynolds number is high enough. Moreover, the outlet jet temperature is significantly higher than the cold plate temperature. The two configurations present different impinging behaviors due to the differences on the flow. Heat transfer analysis on the hot wall has revealed that the circular configuration reaches a higher heat transfer peak than the slotted configuration, however, heat transfer decays faster in the circular configuration when moving away from the jet centerline. Eventually, correlations for the heat transfer at the hot wall and the outlet temperature with the Reynolds number are proposed. They can be useful to include the cavity effects when using simplified models that do not account for actuator cavity.

Keywords: ALE; DNS; Heat Transfer; LES; Numerical Simulation; Synthetic Jet Actuator; Vortex

Flow and Heat Transfer of Impinging Synthetic Jets

by Arnau Miró Jané

Terrassa, April 2019

Preface

This dissertation is the culmination of more than ten years of studies, that started back in 2008 when I was an undergraduate freshman in Universitat Politècnica de Catalunya. Throughout these years, I developed a passion for aeronautics, numerical modeling (especially computational fluid dynamics) and high performance computing. This research is based on this motivation and a device, a synthetic jet actuator, that becomes more and more important nowadays, when there is a need for high aeronautical and thermal performances.

This work has been performed inside the research group TUAREG (TUrbulence and Aerodynamics REsearch Group), in collaboration with Barcelona Supercomputing Center's (BSC) Computer Applications in Science and Engineering (CASE) department. Financial support has been obtained from the Ministry project (MEC) FIS2016-77849-R; as well as the competitive projects by Red Española de Surpercomputación (RES, refs. FI-2016-3-0014 and FI-2017-2-0017) that (along with the collaboration with BSC CASE) awarded time in MareNostrum III and MareNostrum IV. Part of this work has also been performed under the project HPC-EUROPA3 (INFRAIA-2016-1-730897), with the support of the EC Research Innovation Action under the H2020 Programme; in particular, the author gratefully acknowledges the support of Scientific Computing Department of STFC Daresbury Laboratory and the computer resources and technical support provided by EPCC. This work also used the ARCHER UK National Supercomputing Service (http://www.archer.ac.uk).

Moreover, I could not have achieved my current level of success without a strong support group. First, my supervisor Dr. Manel Soria for encouraging me to start this path and for his enthusiasm and support during all these years. My co-supervisor, Dr. Juan Carlos Cajas, for all the patience and support of teaching me all the workarounds in Alya. Also, Dr. Ivette Rodriguez and Dr. Oriol Lehmkuhl for all the interesting discussions and expertise in CFD. Second, to Dr. Guillaume Houzeaux and Mariano Vazquez for letting me be part of CASE and use their computational resources. Also to Prof. David Emerson and Dr. Charles Moulinec for hosting me in STFC Daresbury Laboratory and providing me access to the UK supercomputing facilities and the countless support with Code_Saturne.

I would also like to express my gratitude to my colleagues and friends Rocío Martín and David de la Torre for cheering me up and the nice conversations during lunch time, as well as providing useful insight on the realization of this dissertation. To my parents, who supported me with love

and understanding. And finally my most sincere gratitude to Esma Karagöz, for being always at my side and pushing and supporting me so I could give my best.

Thank you all for your unwavering support.

Contents

Abstract ii

Preface iv

Contents vi

List of Figures viii

List of Tables x

Abbreviations xi

Symbols xii

1 Introduction 1
- 1.1 Literature Review . . . 5
  - 1.1.1 Synthetic jet formation and characterization . . . 6
  - 1.1.2 Flow dynamics of a SJA . . . 7
  - 1.1.3 Synthetic jet impingement . . . 11
  - 1.1.4 Numerical methodologies for representing SJA . . . 13
  - 1.1.5 Applications of SJA . . . 14
- 1.2 Objectives and scope . . . 18
- 1.3 Approach and Outline . . . 19

I Mathematical and Numerical Description 21

2 Mathematical Model for Synthetic Jet Actuators 22
- 2.1 Geometry and Configurations Studied . . . 22
- 2.2 Dimensional Analysis of the Governing Equations . . . 24
- 2.3 Actuator Membrane Model . . . 26
- 2.4 Analysis of the Governing Parameters . . . 30

3 Turbulence Modeling 36
- 3.1 Modeling of the Navier-Stokes equations using RANS/URANS . . . 37
  - 3.1.1 The mean flow equations . . . 37
  - 3.1.2 Additional unknowns in RANS . . . 38
  - 3.1.3 A transport equation for k . . . 39

3.1.4 Scalar transport equation . . . 41
3.1.5 RANS models . . . 42
3.1.6 The $k-\omega$ SST model . . . 43
3.2 Modeling of the Navier-Stokes equations using LES . . . 44
3.2.1 The filtered equations . . . 45
3.2.2 The Smagorinsky model . . . 47
3.2.3 The wall-adapting local eddy viscosity model (WALE) . . . 47
3.3 Modeling of the Navier-Stokes equations using Direct Numerical Simulation (DNS) . . . 48
3.3.1 Flow statistics . . . 49
3.4 Energy preserving in the Navier-Stokes equations . . . 49

II Results and Discussion **51**

4 Domain Analysis and Grid Sensitivity Studies **52**
4.1 Computational domain and boundary conditions . . . 53
4.2 Data reduction . . . 54
4.3 Computational grid analysis . . . 55
4.4 Temporal convergence study . . . 58

5 Dynamics of Synthetic Jet Flow **61**
5.1 Instantaneous flow . . . 62
5.1.1 Slotted configuration . . . 62
5.1.2 Circular configuration . . . 65
5.1.3 Frequency analysis of the flow . . . 70
5.2 Time and phase averaged flow . . . 73
5.2.1 Slotted configuration . . . 73
5.2.2 Circular configuration . . . 76
5.3 Comparison of the slotted and circular configurations . . . 78

6 Heat Transfer Analysis of Impinging Synthetic Jets **84**
6.1 Instantaneous and time and phase averaged temperature . . . 84
6.1.1 Slotted configuration . . . 85
6.1.2 Circular configuration . . . 87
6.1.3 Frequency analysis of the temperature . . . 88
6.2 Instantaneous and time-averaged heat transfer . . . 90
6.2.1 Slotted configuration . . . 90
6.2.2 Circular configuration . . . 95
6.3 Comparison of the slotted and circular configurations . . . 97

7 Conclusions and Future Work **99**
7.1 Conclusions . . . 99
7.2 Future Work . . . 102
7.3 Publications derived of this work . . . 103

List of Figures

1.1 Depiction of a synthetic jet actuator . . . 1
1.2 Example of the flow of a SJA . . . 2
1.3 Examples of SJA configurations . . . 4
1.4 Two dimensional synthetic jet flow at $Re = 50$ . . . 8
1.5 Vortex dipole formation by the action of a piston . . . 9
1.6 Squid jet propulsion . . . 10
1.7 Schematic representation of the flow morphology of a round synthetic jet . . . 11
1.8 Schematic of a synthetic jet impinging into a heated wall . . . 12
1.9 Vortex dynamics at the impinging wall . . . 13
1.10 SJA implementations for thermal control . . . 17

2.1 Geometry of the analyzed configurations . . . 23
2.2 Ratio of f_0 and f_h for various Re and $d = 1$ mm . . . 24
2.3 Membrane profile functions for a slotted actuator . . . 28
2.4 Membrane profile functions for a circular membrane . . . 29
2.5 Evolution of the jet formation criteria with Sk and Re . . . 33
2.6 Effect of the jet formation criteria in the slotted geometry . . . 34
2.7 Effect of the jet formation criteria in the circular geometry . . . 35

4.1 Geometry of the analyzed configurations . . . 53
4.2 Computational grid examples . . . 56
4.3 Grid convergence study at $Re = 500$ for both configurations . . . 57
4.4 Two point correlation at different Re using the finest grid . . . 58
4.5 Time evolution of the temperature at the orifice at $Re = 500$ . . . 60

5.1 Q-isocontours at different phase $t = 0$ for the slotted configuration . . . 63
5.2 Q-isocontours at different phase $t = \tau/4$ for the slotted configuration . . . 63
5.3 Q-isocontours at different phase $t = \tau/2$ for the slotted configuration . . . 64
5.4 Q-isocontours at different phase $t = 3\tau/4$ for the slotted configuration . . . 64
5.5 Q-isocontours at different phase $t = 0$ for the circular configuration . . . 66
5.6 Q-isocontours at different phase $t = \tau/4$ for the circular configuration . . . 67
5.7 Q-isocontours at different phase $t = \tau/2$ for the circular configuration . . . 68
5.8 Q-isocontours at different phase $t = 3\tau/4$ for the circular configuration . . . 69
5.9 Temporal evolution of the stream-wise velocity for both configurations at $Re = 500$ . . . 71
5.10 Energy spectrum of the stream-wise velocity for both configurations at $Re = 500$ . . . 72
5.11 Time averaged velocity streamlines for the slotted configuration at $Re = 500$ . . . 73
5.12 Coordinates of the vortex centers for the slotted configuration . . . 74
5.13 Jet half-width with the domain height for the slotted configuration . . . 74
5.14 Phase averaged velocity streamlines for the slotted configuration at $Re = 500$ . . . 75

5.15 Phase averaged velocity profiles at the actuator orifice for the slotted configuration . 77
5.16 Time averaged velocity streamlines for the circular configuration at $Re = 500$ 78
5.17 Phase averaged velocity streamlines for the circular configuration at $Re = 500$ . . . 79
5.18 Phase averaged velocity profiles at the actuator orifice for the circular configuration . 80
5.19 ime averaged distributions of the swirl and shear strength parameter 81
5.20 Distribution of the turbulent kinetic energy at the expulsion stroke 82
5.21 Temporal evolution of Θ_1 vortex for both configurations 83
5.22 Jet half-width with the domain height for both configurations 83

6.1 Time evolution of the temperature at the SJA outlet for the slotted configuration . . . 85
6.2 Phase averaged temperature profiles at the actuator orifice for the slotted configuration 86
6.3 Phase averaged outlet temperature during suction for the slotted configuration . . . 87
6.4 Time evolution of the temperature at the SJA outlet for the circular configuration . . 88
6.5 Phase averaged temperature profiles at the actuator orifice for the circular configuration 89
6.6 Temporal evolution of the temperature for both configurations at $Re = 500$ 91
6.7 Energy spectrum of the temperature for both configurations at $Re = 500$ 92
6.8 Instantaneous local Nusselt number at the hot wall for the slotted configuration at phase $t = 0$. 93
6.9 Instantaneous local Nusselt number at the hot wall for the slotted configuration at phase $t = \tau/4$. 93
6.10 Instantaneous local Nusselt number at the hot wall for the slotted configuration at phase $t = \tau/2$. 93
6.11 Instantaneous local Nusselt number at the hot wall for the slotted configuration at phase $t = 3\tau/4$. 93
6.12 Time and span-wise averaged Nusselt number for the slotted configuration 94
6.13 Nusselt number correlation with Reynolds number for the slotted configuration . . . 95
6.14 Instantaneous local Nusselt number at the hot wall for the circular configuration at phase $t = 0$. 96
6.15 Instantaneous local Nusselt number at the hot wall for the circular configuration at phase $t = \tau/4$. 96
6.16 Instantaneous local Nusselt number at the hot wall for the circular configuration at phase $t = \tau/2$. 96
6.17 Instantaneous local Nusselt number at the hot wall for the circular configuration at phase $t = 3\tau/4$. 96
6.18 Time averaged Nusselt number for the circular configuration 97
6.19 Time evolution of the temperature at the SJA outlet for both configurations 98
6.20 Time averaged Nusselt number for both configurations 98

List of Tables

2.1 Summary of the dimensions 23
2.2 Values of the scaling parameter δ_C 28

Abbreviations

AFC	**A**ctive **F**low **C**ontrol
ALE	**A**rbitrary **L**agrangian **E**ulerian
CFD	**C**omputational **F**uid **D**ynamics
CPU	**C**entral **P**rocessing **U**nit
CV	**C**ontrol **V**olume
DES	**D**etached **E**ddy **S**imulations
DMD	**D**ynamic **M**ode **D**ecomposition
DNS	**D**irect **N**umerical **S**imulations
JFC	**J**et **F**ormation **C**riteria
LES	**L**arge **E**ddy **S**imulations
LaRC	**La**ngley **R**esearch **C**enter
MEMS	**M**icro **E**lectro **M**echanical **S**ystems
NASA	**N**ational **A**eronautics and **S**pace **A**dministration
PIV	**P**article **I**mage **V**elocimetry
POD	**P**roper **O**rder **D**ecomposition
RANS	**R**eynolds **A**veraged **N**avier **S**tokes
SGS	**S**ub **G**rid **S**cale
SJA	**S**ynthetic **J**et **A**ctuator
SST	**S**hear **S**tress **T**ransport
UHBR	**U**ltra **H**igh **B**ypass **R**atio
URANS	**U**nsteady **R**eynolds **A**veraged **N**avier **S**tokes
WALE	**W**all **A**dapting **L**ocal **E**ddy
ZNMF	**Z**ero **N**et **M**ass **F**ux

Symbols

A	amplitude	m
$\overline{A}$	amplitude, mean	m
d	dimension, orifice	m
H	dimension, height	m
f	frequency	Hz
f_0	frequency, actuator	Hz
f_h	frequency, Helmholtz	Hz
c_p	heat capacity	J/kgK
x_i	position	m
r	position, radial	m
p	pressure	Pa
U_0	reference velocity	m/s
$\overline{U}$	reference velocity, averaged	m/s
S_d	surface, orifice	m^2
S_W	surface, membrane	m^2
L_0	stroke length	m
T	temperature	K
k	thermal conductivity	W/mK
t	time	s
u_i	velocity	m/s
ρ	density	kg/m^3
μ	dynamic viscosity	$Pa\ s$
ν	kinematic viscosity	m^3/s
η	Kolmogorov length scale	m

τ	period	s
k	turbulent kinetic energy	m^2/s^2
ε	turbulent dissipation	m^2/s^3
ϑ	vortex (time-averaged)	
Θ	vortex (phase-averaged)	

Nu	Nusselt number
Pr	Prandlt number
Re	Reynolds number
Ri	Richardson number
Sr	Strouhal number
Sk	Stokes number

To my family and friends.

1

Introduction

The ability to manipulate a flow field in order to improve efficiency or performance or the need for compact cooling solutions that meet good performance requirements at compact volumes are topics of utmost technological importance nowadays [1--4] . Since the late 90s and the early 2000s many studies have been performed regarding a device that had the potential to address this technological need: the Synthetic Jet Actuator (SJA) or Zero Net Mass Flux (ZNMF) actuators [5--10]. The origins of these devices can be traced back to the decades of the '50s up to the '80s, where experiments with acoustic resonators yielded net jets without the addition of mass flux [11--13].

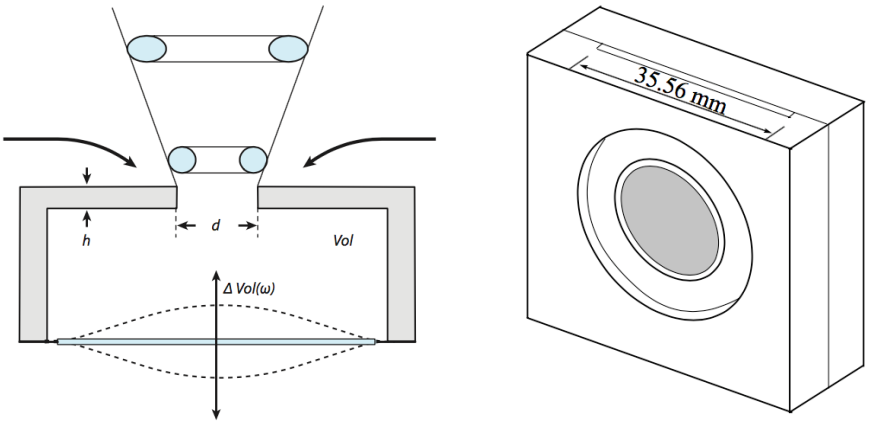

(a) Schematic view (from Cattafesta, 2011 [14]).

(b) Engineering view (from Kotapati, 2007 [15]).

Figure 1.1: Depiction of a synthetic jet (ZNMF) actuator.

Nowadays, synthetic jet actuators consist of a cavity encapsulating a piezoelectric diaphragm (or membrane), as shown in Fig. 1.1. Another possible configuration found in the literature is the use of a piston instead of a mechanically moving diaphragm. The bottom line is that the actuation of this device changes the cavity volume periodically, causing external fluid to enter and leave through a small slot (or orifice). The cavity and the slot can have different geometries. This has an impact on the resulting flow, as discussed in Section 5.3. Under certain conditions, the advected vortices are too far to be ingested back. In this case, a train of vortices, and eventually a jet, are created without the addition of mass flow, allowing the transfer of kinetic energy and momentum to a fluid medium without the need of piping systems. This is measured by the jet formation criteria, which is a parameter that depends on two of the major governing parameters of the SJA flow: the Reynolds number and the Stokes number. The former can be related to the velocity of the advected vortices as well as the fluid properties, while the latter is related to the oscillating frequency of the membrane. This aspect will be further discussed in Section 2.4. Qualitatively, Fig. 1.2 shows a representation of the flow of a SJA at the expulsion and ingestion instants at $Re = 1,000$. In this case, the jet formation criteria is high enough and a pair of vortices can be seen advected from the actuator orifice. During the ingestion, they are far enough from the orifice and are not ingested back. A brief discussion on the flow of a SJA with low jet formation criteria is performed at the end of Section 2.4.

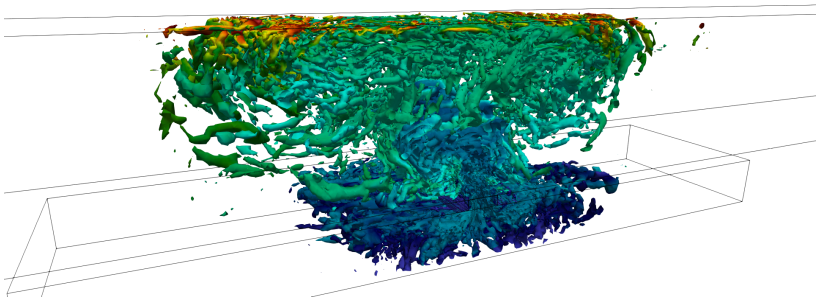

(a) Expulsion instant.

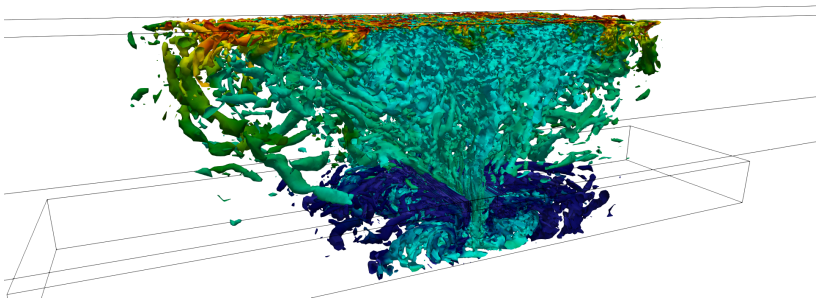

(b) Ingestion instant.

Figure 1.2: Example of the flow of a SJA at $Re = 1,000$. The vortices are visualized using the Q-criterion, as further explained in Chapter 5.

Indeed, synthetic jets are interesting devices from a phenomenological point of view. The flow

patterns that result from the interaction of the currents enter and leaving the cavity with the external flow are very complex (as seen in Fig. 1.2) and have been the subject of many numerical and experimental studies [10, 15--17], which will be discussed in Section 1.1. These patterns are dependent on the geometry of the actuator and orifice [18]. Two major configurations are studied in the literature and are depicted in Fig. 1.3:

- The slotted configuration (Fig. 1.3a), which refers to those actuator geometries that are two-dimensional and that have a clear symmetry plane that passes through the jet centerline. The geometry of the actuators are typically rectangular. The advected vortices receive the name of vortex dipoles.
- The axisymmetric or round/circular configuration (Fig. 1.3b), which refers to those actuator geometries that are inherently three dimensional and present axial symmetries, such as a circular actuator. The advected vortices receive the name of vortex rings.

In this line, a comparison of the flow patterns that a slotted and a circular orifices produce has been performed by the author and is presented in [19]. Computational Fluid Dynamics can, at this point, provide a good insight on the flow configurations of SJA. Nevertheless, further work is still required in some opened topics.

Detailed numerical simulations of SJA are generally expensive. A detailed DNS of the discharge of a SJA at $Re_j = 1150$ (where Re_j is a Reynolds number based on the average exit velocity and $Re = 2Re_j$ according to the notation in this work, as explained in Chapter 2) was performed on a simplified actuator [15]. For more complex geometries, models or applications DNS becomes prohibitive and turbulence models such as LES (e.g., in [17, 22, 23]) or RANS/URANS (e.g., [16, 24, 25]) are needed. Moreover, exceeding a jet Reynolds number of $Re = 1,000$ is generally expensive even under the most simple models. On the other hand, experimental results on SJA tend to focus on Reynolds numbers greater than $1,000$, typically in the range of $1,000 < Re < 5,000$ [26--28]. Nevertheless, there is potential in numerical simulations to bridge the gap between experimental and numerical results along with the development of models (such as LES or DES) that can provide more accurate representations of fairly complex geometries and flows using a relatively small amount of numerical resources. As a brief example, in free shear flows the computational cost of LES is independent of the Reynolds number and becomes practicable. In DNS the computational cost high as it increases of approximately Re^3. As an example, in [29] DNS of a NACA0012 in stall conditions were performed on meshes of around 49 million control volumes that required around 600 CPUs.

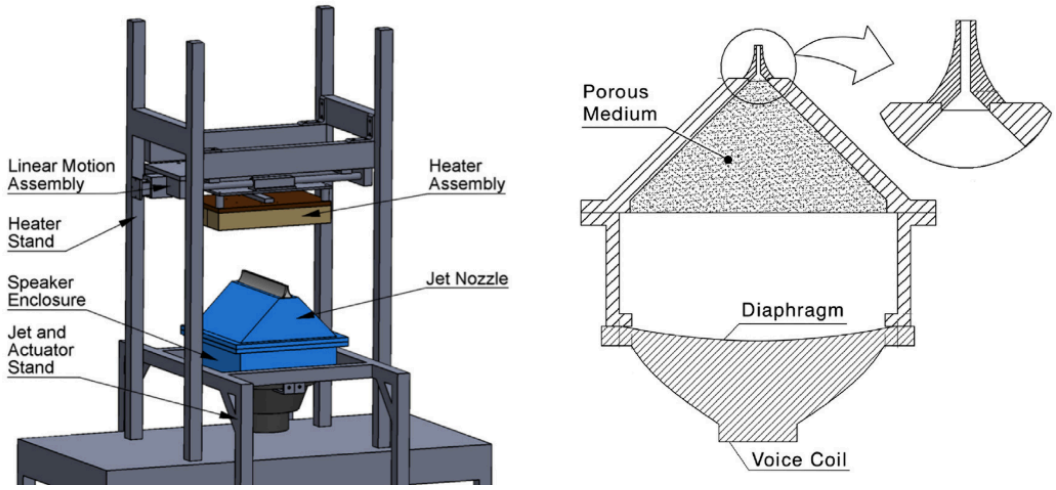

(a) Example of a slotted configuration from an experimental rig from (from Silva-Llanca, 2015 [20]).

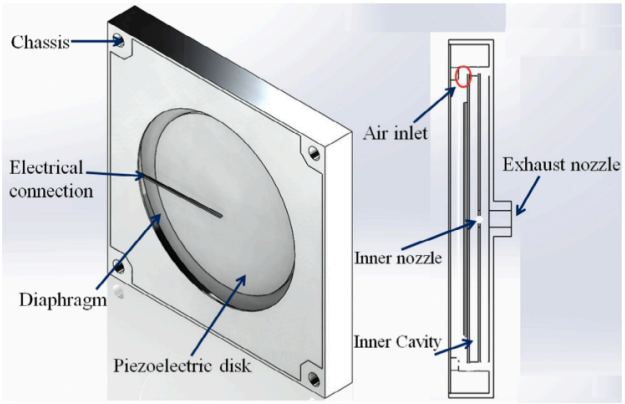

(b) Example of a circular configuration from a piezoelectric ultra sonic micro-blower presented in Ghaffari, 2016 [21].

Figure 1.3: Examples of SJA configurations.

Regarding the actuator frequency, while experimental setups work with moderate to high actuator frequencies (lower frequencies are challenging due to acoustic issues [21]) and are able to provide time-accurate representations of the flow, time integration in numerical simulations must be a tradeoff between accuracy and computational cost. The need of integrating for about 100 actuator cycles or more in order to obtain statistically stationary conditions in the vicinity of the flow is discussed in [15, 17]. Moreover, in [17] it is argued that a broadband low frequency appears when moving away from the jet centerline, thus highlighting the challenge of obtaining statistically stationary conditions in zones far from the jet.

Synthetic jets nowadays find applications in many relevant engineering fields. Active flow control, or the ability to manipulate the flow field in order to improve the aerodynamic performance, is of uttermost technological importance. In the past decades, a considerable amount of research was done in passive flow control and in the last twenty decades, a considerable effort was put on active flow control. In particular SJA are interesting for their ability to generate a jet that can interact with the external flow without the need of pumping systems. Another interesting field for SJA is thermal regulation. Electronic systems nowadays are becoming smaller and smaller. There is a need of a compact cooling system that uses the working fluid of the system and can be embedded within the package. SJAs are seen as a potential solution as they can be miniaturized using Micro Electro Mechanical Systems (MEMS) and do not need an external fluid to create a jet. In fact, this work is devoted to the analysis of a particular cooling solution for SJA: the impingement into a hot wall. More details about the findings in thermal performance of SJA can be found in Chapter 6.

1.1 Literature Review

This section presents an overview of the relevant research concerning synthetic jet actuators found in the literature. First, the necessary conditions for a synthetic jet to form are reviewed, as well as the necessary parameters involved in the characterization of the SJA. Then, the flow dynamics of the jet are reviewed, for the two configurations considered in this work: the slotted and the round (axisymmetric or circular) configurations. The literature reveals that the flow configurations for either cases are significantly different. Afterwards, the particular case where a synthetic jet impinges into a hot wall is examined. Finally, the most relevant engineering applications of synthetic jets are presented.

1.1.1 Synthetic jet formation and characterization

The formation and evolution of SJAs was investigated by Smith and Glezer [10]. The concept of stroke length L_0 was defined as the integral of the stream-wise velocity at the orifice exit u_0 over the ejection part of the cycle, which corresponds to the half of the actuation period τ

$$L_0 = \int_0^{\tau/2} u_0(t)\, dt \tag{1.1}$$

from which a reference velocity $U_0 = L_0/\tau$ can be defined. It was found out that the evolution of the SJA flow near the orifice is dominated by its time-periodic formation and advection of vortices that roll-up and become part of the jet. It was also observed that their mean trajectory scales with the stroke length. A dimensionless stroke length L_0/d, where d is the orifice diameter, was proposed to be one of the parameters that define the SJA flow [30] and corresponds to the inverse of the Strouhal number (Sr)

$$\frac{L_0}{d} = \frac{1}{Sr}. \tag{1.2}$$

The jet formation criteria (JFC)

$$\text{JFC} = \frac{1}{\overline{Sr}} = \frac{\overline{Re}}{\overline{Sk}^2}, \tag{1.3}$$

was introduced by Utturkar and Holman [31, 32], where $\overline{Sr}$, $\overline{Re}$ and $\overline{Sk}$ are the Strouhal, Reynolds and Stokes numbers based on a time and space averaged velocity $\overline{U}$ at the SJA exit during the expulsion stroke ($\overline{U} = 2U_0$). The difference between this jet formation criteria and the dimensionless stroke length is a constant, as is further discussed in this work. The formation of synthetic jets was analyzed for axisymmetric and two-dimensional configurations and notorious differences were found between them, even though the orifice geometry was similar. The axisymmetric and the two-dimensional configuration have different threshold values of the JFC to obtain the jet formation. In the case of the circular configuration this threshold is $K = 0.16$ and for the slotted case $K = 2$. Moreover, as predicted by Utturkar and Holman, experimental investigations of SJA cavity [18] and orifice shape [33, 34] have been found to be influential on the synthetic jet performance.

Silva-Llanca [35] recently proposed a definition of the Reynolds number using the stroke length, as

$$Re_{L_0} = \frac{U_0 L_0}{\nu} = 2\pi \frac{Re^2}{Sk^2}. \tag{1.4}$$

It was found out that this definition describes better the flow regime and was used to measure when the flow goes into a transitional state. Indeed, this parameter is interesting as it combines the Reynolds number and the dimensionless stroke length (or jet formation criteria)

$$Re_{L_0} = Re \frac{L_0}{d}. \tag{1.5}$$

Another important characteristic of SJA is its natural resonating frequency, also known as Helmholtz frequency f_h. Such phenomenon can be described by imagining what would happen if extra air is forced inside the actuator cavity. A common example of this is when blowing air inside an empty bottle in order to produce a sound. In this case, the air blown inside the bottle compresses the air inside. The pressure will drive it out, however, when it returns to its original position a slight vacuum is produced inside the bottle that will suck the air back in. This causes the air inside the bottle to vibrate (thus producing a sound), much like a mass on a spring. In synthetic jets, when this phenomenon occurs, incompressible treatment fails to describe accurately the behavior of the fluid, and a compressible treatment is needed. It has been shown both experimentally and numerically that, when the drive frequency divided by the resonance frequency is more than 0.5, compressible effects take over, thus forgoing an incompressible treatment [36]; i.e., for $f/f_h < 0.5$ incompressible treatment is possible.

1.1.2 Flow dynamics of a SJA

As aforementioned, the flow patters of SJA are highly dependent on the actuator geometry. Vortex rings for circular configurations and vortex dipoles for two-dimensional configurations are the result from the interaction of the currents entering and leaving the cavity are substantially different and complex. Many studies have been devoted to analyze the flow morphology of these two configurations, the most relevant are reviewed here.

Due to the differences in the geometry of these two configurations, the flow dynamics are essentially different. However, some similarities exist in how the jet is created. Jet creation occurs when a stream of fluid is injected into the surrounding medium due to the action of an actuator [37].

Such actuator can be a piston or a membrane. Afterwards, the actuator retracts and the external fluid is ingested inside the actuator. This yields to four relevant phases on the dynamics of SJA flow:

- Maximum expulsion instant, when the velocity at the orifice is maximum (towards the external medium) and the actuator is moving towards the orifice.
- Maximum positive deployment of the actuator, when the position of the actuator is nearest to the orifice and its displacement velocity is zero.
- Maximum ingestion instant, when the velocity at the orifice is maximum (towards the inside of the actuator) and the actuator is moving further from the orifice.
- Maximum negative deployment of the actuator, when the position of the actuator is farthest from the orifice and its velocity is zero.

The near external field is dominated by vortices caused by the separation of the shear layer and its instability growth. The motion induced in the fluid by each vortex affects other vortices so that adjacent vortices pair off, as shown in Fig. 1.4. Note that, under the right circumstances, the flow is ingested back without affecting the newly formed vortex pair, hence allowing the jet formation. Moreover, as it can be seen in Fig. 1.4, the ingested flow comes from the sides of the orifice.

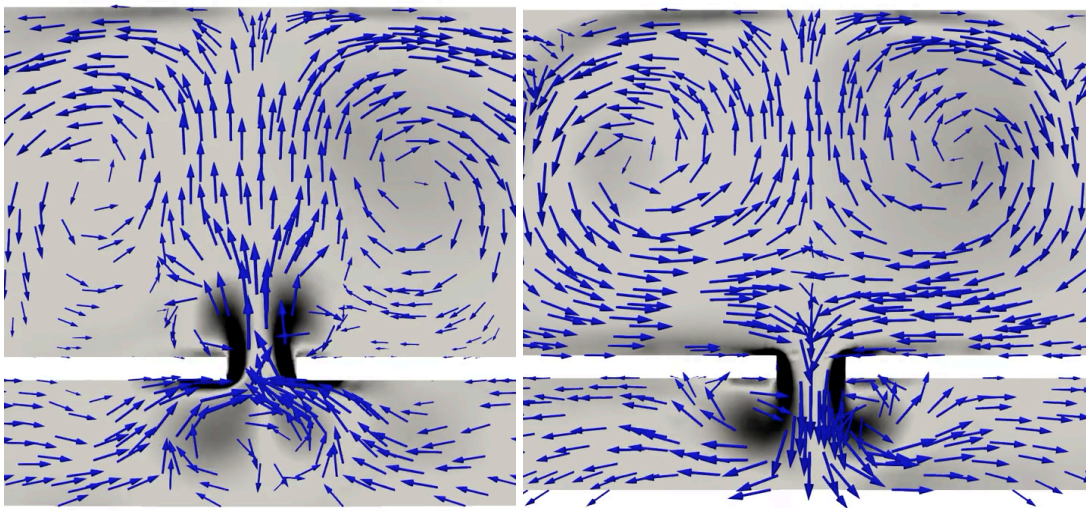

(a) Expulsion instant. (b) Ingestion instant.

Figure 1.4: Two dimensional synthetic jet flow at $Re = 50$. The vorticity is shaded in black and white and the velocity is plotted using vectors.

Other flow dynamics are particular of the configuration studied. The following sections are devoted to the understanding of the flow dynamics of slotted and circular SJA.

The slotted configuration

Slotted SJA configurations form vortex dipoles. They are formed in a viscous fluid when a force is applied locally to a volume of fluid and a roll up is produced [38]. A clear example of this is when a piston moving forward pushes out a volume of fluid in a two-dimensional frame. Then, two vortex form in front of the developing flow, while a trailing jet is established behind, as shown in Fig. 1.5.

Vortex dipoles are a well-known feature of (quasi) two-dimensional flows and are found in many different contexts (i.e., oceanography [39]). One particularity of vortex dipoles is that vortex separation (or pinch-off) from the trailing jet occurs at a higher stroke ratio than on vortex rings [38]. The dipole is fed by the fluid from the trailing jet and its vorticity grows linearly with time; thus accumulating most of the vorticity of the flow, while the rest is stored in the trailing jet. Then, if vortex pinch-off does not occur, the vortex dipole entrains all of the circulation produced by the generator.

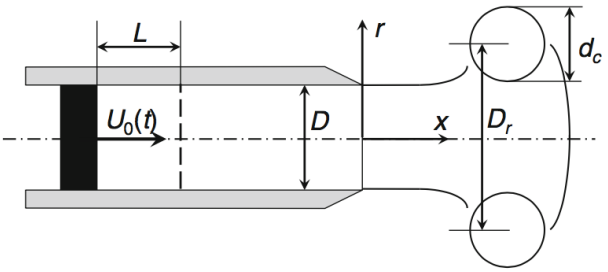

Figure 1.5: Vortex dipole formation by the action of a piston (from New, 2015 [37]).

Kral and Donovan (1997) [6] performed early studies on an incompressible laminar and turbulent two-dimensional synthetic jet using the unsteady RANS Spalart-Allmaras one-equation model. The SJA was successfully implemented as a suction/blowing boundary condition (thus avoiding any representation of the SJA cavity) and the results obtained presented a good correlation with the later experiments of Smith and Glezer (1998) [10]. Early direct numerical simulations (DNS) of an array of two SJA were performed by Lee and Goldstein (2002) [40] under the hypothesis of two-dimensional incompressible flow. The actuators were modeled as a moving piston using virtual surfaces. Despite the simulations being two dimensional, a fair agreement was shown with experimental data near the jet orifice. In addition, it was observed that the shape of the lips and the cavity depth were important parameters of the resulting flow. Three dimensional span-wise periodic DNS of a synthetic jet previously analyzed with particle image velocimetry (PIV) [41] (in the framework of the NASA LaRC Workshop, 2004) were performed by Kotapati et al. (2007) [15]. Despite simplifying the actuator geometry, it was found out that the results closely agree with the experimental results. The main vortex pairs that convect downstream by self-induction were successfully identified along with secondary stream-wise oriented rib-like structures surrounding the main vortex cores. It was found that these structures undergo amplification in the span-wise direction due to vortex stretching and cause the transition to turbulence of the main vortices in the vicinity of the orifice and a well-developed turbulent jet is eventually formed. Moreover, large convective time scales in the outer flow of at least an order of magnitude higher than the actuator period were foreseen to appear, thus having strong implications in computational time. In fact, the presence of these large scales was found to indicate that large sampling times are required in order to obtain accurate statistics of the outer region of the flow. Miro et al. (2018) [17] further investigated into this issue and found that these large time scales roughly corresponded to 7 periods and the time required to obtain accurate statistics was of about 200 cycles.

Due to the vortical nature of the SJA flow, the analysis of the vortices becomes a key parameter for the understanding of the flow dynamics. Experimental and numerical investigations of the vortex dynamics and merging of two-dimensional synthetic jets have been performed by Silva-Llanca et. al. (2015, 2017) [16, 20, 35]. Different techniques for identifying coherent structures in synthetic

jets were compared and the Q-criterion [42] was selected as a vortex presence indicator. Three stages of vortex merging were identified in two-dimensional impinging synthetic jets, in which the expelled vortex slowly merges with the remaining vortex of the previous actuator cycle. This phenomenon was found to be directly proportional to the Reynolds number and inversely proportional to the frequency.

The axisymmetric (round, circular) configuration

Axisymmetric SJA configurations form the three dimensional counterpart of vortex dipoles: vortex rings. In a vortex ring, the vortex shedded from the actuator lips rolls over itself forming a torus (or a ring). Their generation is natural in numerous practical application in nature and industry, e.g., the propulsion of some aquatic animals is based on this mechanism [43] (see Fig. 1.6).

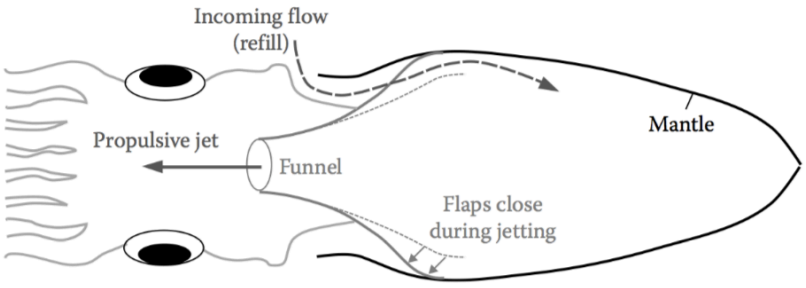

Figure 1.6: Squid jet propulsion (from Mohseni, 2014 [44]).

The flow behavior of axisymmetric impinging synthetic jets has been experimentally analyzed by Greco et. al. [28, 45]. Two different jet morphologies, as depicted in Fig. 1.7, were observed in terms of the dimensionless stroke length. For low dimensionless stroke length or jet formation criteria ($4 \leq L_0/d < 8$ or $1.27 \leq$ JFC < 2.55) the Strouhal number is high and the jet morphology consists of a succession of primary vortex rings as shown in Fig. 1.7b, where the impingement is dominated by the vortex ring and results in a larger jet width and lower centerline velocity. On the other hand, at high dimensionless stroke lengths or jet formation criteria ($8 \leq L_0/d < 16$ or $2.55 \leq$ JFC < 5.09) the Strouhal number is low and the flow is formed by a disconnected primary vortex ring followed by a trailing jet and a region of low turbulence, called potential core as shown in Fig. 1.7a. In these flows, the trailing jet, which is formed of multiple vortex rings generated by the Kelvin-Helmholtz instability, becomes the most influential feature of the flow. This behavior and time scales are consistent with those observed in vortex ring formation for steady jets [46]. In this context, it was observed that, in the case of a vortex ring followed by a trailing jet, the vortex ring reduced its circulation by shedding the excess vorticity into its wake.

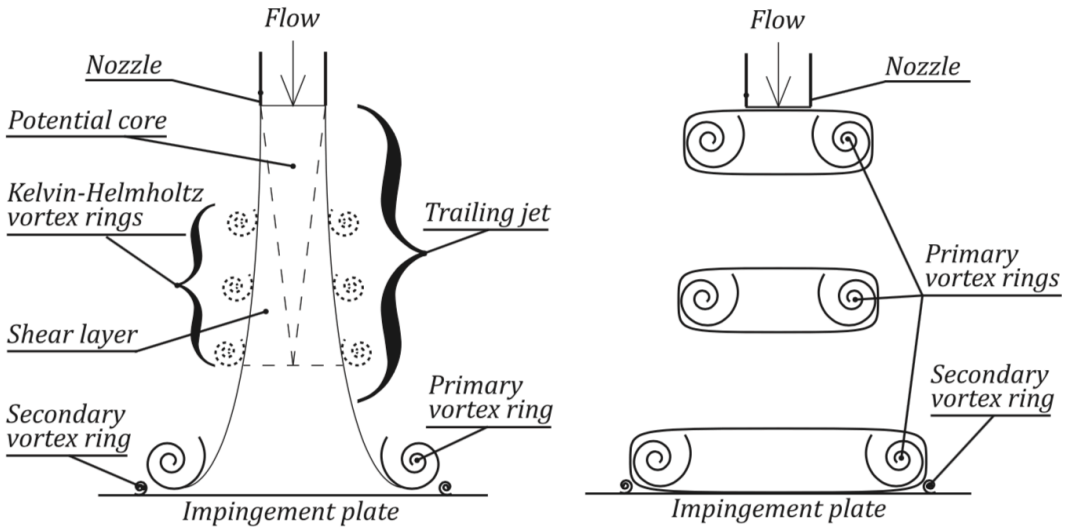

(a) High dimensionless stroke length. (b) Low dimensionless stroke length.

Figure 1.7: Schematic representation of the flow morphology of a round synthetic jet (from Greco, 2018 [28]).

1.1.3 Synthetic jet impingement

Synthetic jet impingement refers to the the geometrical configuration where a synthetic jet collides with an object, typically a plate, as depicted in Fig. 1.8.

In the heat transfer context, heat exchange occurs between the jet and the object and has been the subject of many studies [33, 48--51]. In particular, the aforementioned experimental and numerical two-dimensional investigations of Silva-Llanca et al. [16, 20] are of interest concerning synthetic jet impingement. In their work, a formulation is presented that allows to vary independently the Reynolds and Stokes numbers, thus opening the possibility to vary independently the jet velocity and the jet driving frequency. This was done aiming to achieve a better understanding of the jet dynamics. The impingement phenomena was investigated for different jet-to-width ratios and found out that for a jet-to-surface spacing of 5 could be optimal for their SJA configuration. Such optimum is defined so that the vortices arrive at the heated wall at their peak of intensity [35]. As for jet-to-surface spacings greater than 5, the merging of consecutive vortex pairs occurs prior to the impingement and diminishes the overall heat transfer. This was in good agreement with the experimental investigations of Ghaffari et al. [26]. Therefore selecting the adequate jet-to-width ratio is one heat transfer enhancing method for impinging synthetic jets. Several different jet-to-surface spacings were investigated using the PIV technique and it was found that the optimal ratio of jet-to-surface spacing that maximizes heat transfer is between 5 and 10. Silva-Llanca's canonical geometry [16] was also used to investigate the flow of a purely oscillatory jet, and a new formulation for the jet characteristic velocity was introduced. It was observed that vortex

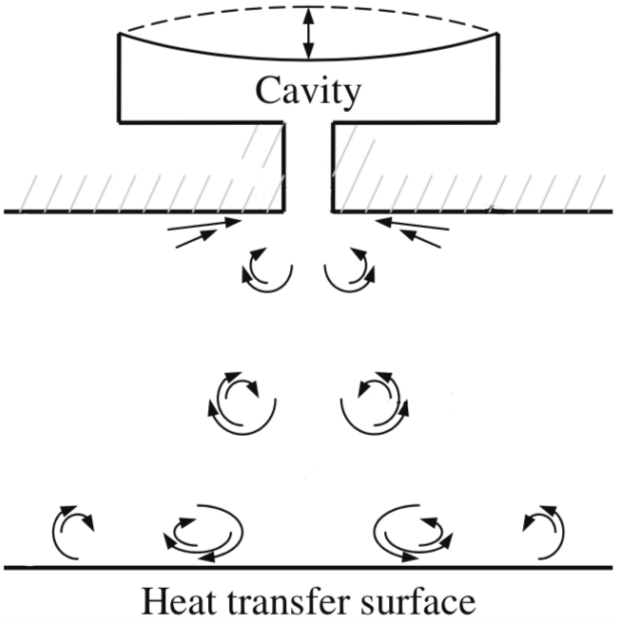

Figure 1.8: Schematic of a synthetic jet impinging into a heated wall (adapted from Valiorgue et. al., 2009 [47]).

coalescence reduces the heat transfer capacity of the jet. Therefore, another method to improve heat transfer is to generate stronger vortices at a higher frequency [35]. Moreover, secondary vortices with opposite circulation that the main vortex are found to be generated when the vortex pair arrives near the heated wall as shown in Fig. 1.9. These secondary vortices sweep the heated surface thus effectively enhancing the heat transfer of the synthetic jet.

Several applications for synthetic jet impingement are possible, for example, they have been proposed for cooling of circuit boards and miniature electronics. Such applications are reviewed in Section 1.1.5. A common point of these studies is that an open configuration is considered for the discharge domain. In these cases, a simplified actuator model is used, as the heated flow is not ingested back inside the actuator and the temperature at the SJA outlet can be assumed to be constant [52--54].

Other works have been carried out in confined configurations, i.e., the jet is enclosed between two parallel plates. Experimental investigations of this configuration were performed by Vukasinovic and Glezer [55] on an axisymmetric synthetic jet. It was found that the temperature of the jet at the expulsion is significantly above the ambient temperature due to a countercurrent in the flow formed by the confining plate. Moreover, the cooling efficiency of the jet was observed to decrease with the spacing between the parallel plates. Very recent numerical studies of opened and enclosed configurations of an axisymmetric synthetic jet, using moving mesh techniques for the membrane description, have been performed by Hatami et al. [25]. Noticeable differences were found in the

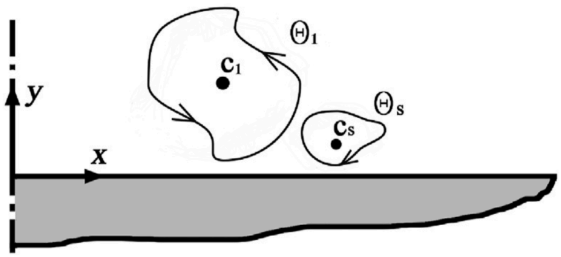

(a) Schematic view (from Silva-Llanca, 2017 [16]).

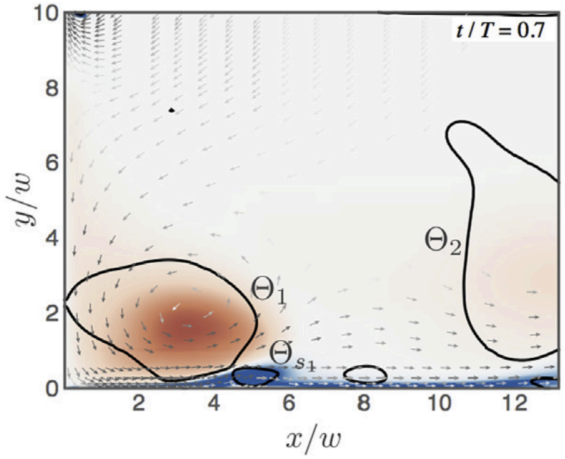

(b) Vorticity map (from Silva-Llanca, 2017 [35]).

Figure 1.9: Vortex dynamics at the impinging wall showing the creation of a counter-rotating secondary vortex Θ_s.

flow and heat transfer capabilities between the enclosed and opened configurations. In particular, the advected vortices were found to stretch axially on the enclosed configuration whereas in the opened configuration they stretch radially. This has been found to produce more coherent vortices in the opened configuration compared with the enclosed configuration.

1.1.4 Numerical methodologies for representing SJA

Several methodologies for representing the SJA and the interaction of the flow inside the actuator cavity have been used in previous studies. They are, in decreasing order of computational time:

- Model M1: the actuator membrane movement is described using a somewhat realistic way and the flow inside the cavity is simulated. Mesh moving techniques, such as Arbitrary Lagrangian Eulerian (ALE) formulation has been successfully used to model the time-dependent movement of the SJA membrane [56]. Other implementations in the literature for realistic models of the SJA membrane are Chimera grids [57], virtual forces to emulate the effect of a moving boundary [40], the mass-spring analogy method [58], and dynamic mesh methods [25].
- Model M2: the internal flow is simulated but the time derivative of the membrane position respect to the bottom of the cavity is used as a velocity boundary condition. This approach was used by Kotapati et al. [15] in their DNS.

- Model M3: The cavity flow is not simulated, instead, a velocity profile at the actuator lips is imposed. This is probably the most used model in the literature due to its simplicity of implementation and low computational time [6, 20, 53] . It is also used for industrial applications with complex geometries [59].

Clearly, M1 models allow imposing physically realistic boundary conditions for the momentum and energy equations at the actuator membrane. This is beneficial when trying to understand the interaction between the external flow (at the discharge cavity) and the internal flow (inside the SJA), as otherwise parameters such as temperature or vorticity and turbulent kinetic energy would remain unknown and would be hard to estimate. M2 models also allow a good representation of the actuator cavity, however, the aforementioned parameters would also remain unknown at the membrane. As a drawback, simulating the turbulence inside the cavity in M1 and M2 and simulating the membrane movement in M1 add considerable complication and computational cost to the simulation of SJAs. M3 models are clearly the simplest, however, they have proved (as well as M2) to be able to represent the jet in the far field and obtain relevant data [6, 16], in good agreement with the results obtained with M1 [17]. An analysis of the performance of the different numerical methodologies was done in [60] using a synthetic jet in a crossflow as a test case and [61] using an impinging synthetic jet as a test case. In both cases, the slot was included in the model due to its importance in the physics of the flow. It was also found that M2 represents a good compromise between accuracy and cost; and for large-scale flows M3 provides the most cost-effective approximation.

1.1.5 Applications of SJA

SJA are not only interesting from a phenomenological point of view but also find applications in many fields. The most relevant fields, Active Flow Control (AFC), thermal control and cooling and mixing enhancement, are reviewed here.

Active flow control (AFC)

The ability to manipulate a flow field in order to improve efficiency or performance of the aerodynamic components is of technological importance. During the 1970's and 1980's a considerable amount of research was performed aiming towards turbulent drag reduction, emphasizing on passive flow control methods. Since 1990, great research effort is being devoted to Active Flow Control (AFC) [62], based on the introduction of kinetic energy in the boundary layer, a concept first proposed by Prandtl more than a century ago [63].

In the 1960s, it was shown that the use of steady blowing or suction could produce significant increases in lift and reductions in drag. However, the large momentum coefficients needed to do so imply excessive compressor bleeding and high technical complexity of the plumbing system. On the other hand, as first shown by Schubauer and Skramstad [64] in 1948, periodic perturbations create vortex structures which increase the momentum transfer between the free stream and the boundary layer and increase resistivity against flow separation [65]. This mechanism allows an effective control of the flow with momentum coefficients up to two orders of magnitude lower than static blowing/suction [66], and opens the possibility of achieving AFC with small, autonomous and energy efficient actuators.

On this line, Spalart et al. [67] performed preliminary simulations of a blowing/suction AFC device to unload the wind of the V-22 tilt-rotor aircraft using a Detached-Eddy Simulation approach at $Re = 3 \times 10^5$. The geometry was a modified NACA 0012 at an angle of attack of -85 degrees and a flap deflection of 85 degrees. Later, both You and Moin [68] and Uribe et al. [23] simulated the flow over a NACA 0015 airfoil by means of LES simulations and used SJA as AFC devices. They both implemented the SJA as a blowing/suction orifice and clustered the mesh around the nozzle to ensure appropriate resolution of the flow.

More recently, Fricke [65] simulated an Ultra High Bypass Ratio (UHBR) engine-wing junction in the frame of the Vision2020 and Flightpath 2050 projects. Due to the large diameter of UHBR engines, they interfere with the leading edge devices and lead to flow separation that may compromise the total aircraft efficiency [69]. The simulations were carried out using URANS Spalart-Almaras turbulence closure. Velasco et al. [24] performed two-dimensional simulations of a Darrieus turbine using synthetic jets for AFC. The simulations were carried out using time-accurate RANS $k-\omega$ turbulence model. It was found out that AFC incremented the net power generated by the turbine and this power was higher than the one consumed by the SJA; thus the total efficiency was increased. Experimental wind tunnel investigations of a simplified generic truck cabin with AFC were performed by Minelli et al. [2]. Synthetic jets implemented by means of loudspeakers were selected as AFC actuator due to their low power consumption. PIV was performed to analyze the flow patterns and Proper Order Decomposition (POD) was used to analyze the main coherent structures of both the actuated and unactuated flow. The application of AFC resulted in a substantial drag reduction.

The momentum coefficient C_μ is defined as the ratio between the momentum of the jet and the momentum of the external flow

$$C_\mu = \frac{nU_0^2 S_d}{U_\infty^2 S_\infty}, \tag{1.6}$$

where U_∞ is the velocity of the external flow S_d the orifice area and S_∞ the characteristic external

area (e.g., the wing surface). The parameter n refers to the number of synthetic jets. This coefficient is used to represent the capability of the jet to influence the external flow. Typical values of the momentum coefficient are in the order of 10^{-4} to 10^{-2}, which combined with a typical chord-based Reynolds number of 6×10^6 and a chord-jet outlet ratio in the order of 10^2 to 5×10^3, yields jet Reynolds numbers in the order of 5×10^3 to 2×10^4. The simulation of the jet internal flow has a significant cost, and thus, the selection of the actuator modeling approach is an important issue. While appropriate values for the main control parameters (momentum coefficient, frequency and location of the actuators) can be determined without modeling the actuator internal flow, a more detailed actuator model might be needed to ensure a successful design of the whole AFC system.

Thermal control of electronic devices

One of the most active research areas of heat transfer technologies is the thermal control of electronic devices. The main objective is to increase the performance and reliability of components by decreasing their temperature. Systems that use the fluid enclosed within the electronic device as cooling agent have been proposed as an effective thermal control mechanism [26, 48, 70]. Moreover, electronics tend to become smaller and smaller. Due to such miniaturization, there is a need for compact cooling solutions that meet good performance requirements at compact volumes. One of the main advantages of SJAs in this area is that the need of additional hardware such as fluid ducting is eliminated, thus becoming perfect candidates for MEMS integration [71].

As an example, consider the three lines of CPU cooling that have been proposed in the literature:

- A device that would improve the thermal cooling of fins and fans [72] as shown in Fig. 1.10a. Such device would make use of the heat transfer enhancement of synthetic jets impinging into hot surfaces, as described in Section 1.1.3.
- A device that would enhance the primary cooling methodology [73]. This method would use SJA and agitators to be integrated into air cooling heat sinks. Although the agitator outperforms the synthetic jet in regards to cooling enhancement, when they are both combined they are able to increase a 82.1% the heat transfer.
- A miniature device of a size comparable to that of an electronic microchip [74] as shown in Fig. 1.10b. This device would use the chip's self cooling fluid to enhance convection and increase thermal dissipation.

Although the former has been proven to improve the heat removal by 1.5 times compared with fans and 4.5 times compared to natural convection, the latter represents a challenge to chip developers due to the increased miniaturization in the sector. As an example, the Intel Xeon E5-2670 (Sandy

Bridge EP) of MareNostrum III [75] packs 8 cores in an area of $52.5 \times 45.0\ mm^2$, whereas the Intel Xeon Platinum 8160 (skylake) of MareNostrum IV [76] packs three times more cores (24 cores) in a package just about 1.4 times bigger ($76.0 \times 56.5\ mm^2$). Other representative cases are the new Core i9-7900X packing 10 cores in the same package of $52.5 \times 45.0\ mm^2$ or the new mobile Core i9-8950HK packing 6 cores in $42 \times 28\ mm^2$ [77].

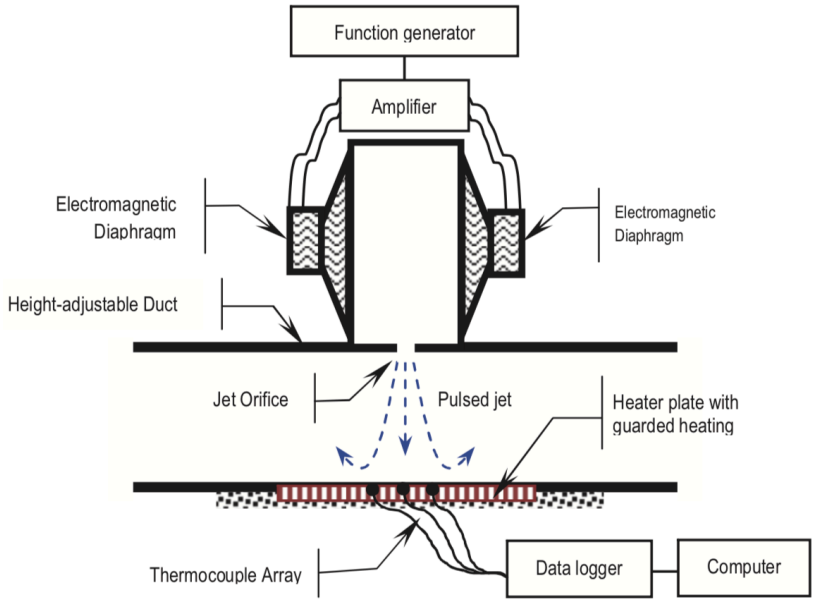

(a) Twin loudspeaker SJA (from Chandratilleke, 2013 [72]).

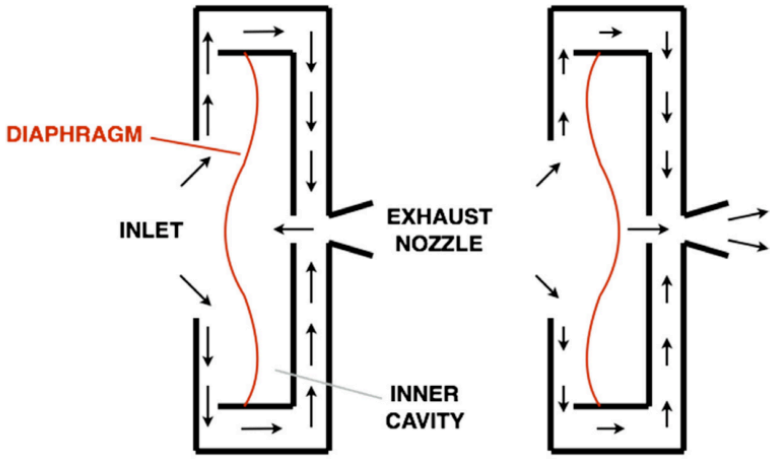

(b) Micro-blower SJA (from Ghaffari, 2016 [26]).

Figure 1.10: Synthetic Jet Actuator implementations for thermal control.

One of the most challenging fields in SJA is the design and construction of the resonator cavity. Many studies have been performed to analyze the influence of cavity geometry. It has generally been found that very shallow cavities have a detrimental effect on the jet velocity while orifices with a larger hydraulic diameter in conjunction with a smaller aspect ratio proved to give the best results in heat transfer [78]. Another major limitation of SJA is their high noise output as they often require

operation at the actuator resonant frequency to maximize jet exit velocity [26]. Most experimental investigations construct SJA using loudspeakers, however, this might not be the best solution for compactness. Piezoelectric membrane SJA can be compacted but present the drawback of the oscillating membrane. To overcome this handicap, double cavity SJAs or multiple orifice SJAs have been proposed, such as Fig. 1.10b, in order to overcome this problem.

Mixing enhancement

Nowadays, a main concern for combustors is the reduction of pollutant emissions, such as CO, NO_x and unburned fuel (e.g., in aeronautics is a main concern during takeoff and landing), while maintaining combustion efficiency. A viable method is to enhance the fuel-air mixing process so that the initial dense spray regime is minimized and the vaporized fuel-air regime is maximized.

Attempts are focused on changing the pattern of the fuel injected into the combustor in order to modify the fuel-air mixing. Design include the use of multiple injection using microlaminated screens and advanced swirler cups. The concept of active fuel control was developed by Chen [79] when he used the synthetic jet actuators developed by Glezer and co-workers as a kind of active fuel mixing enhancers. This concept was later improved by Wang [80] by introducing synthetic jet as MEMS actuators. This turned out to be a necessity, as for example, a typical gas turbine combustor was around 15 cm long and a typical fuel injector had around 3 mm diameter. Then, a SJA used for fuel mixing enhancement that must fit inside the fuel injector has to be even smaller; with 0.1 mm of orifice diameter.

1.2 Objectives and scope

The majority of the studies reviewed consider an open configuration in which the synthetic jet impinges to a hot wall and use simplified actuator models and often disregard the cavity fluid interaction and the moving membrane in favor of a model that provides the velocity at the actuator lips. In these cases, the heated flow is not ingested back inside the actuator and the temperature at the SJA outlet can be assumed constant. What would happen if the heated flow is ingested back? This happens when the jet is enclosed between two parallel plates. Then, how are the boundary conditions selected? What are the effects of overestimating or underestimating the conditions at the actuator orifice?

This dissertation main objective is to provide insight on the implications of simulating an enclosed SJA and its the actuator cavity in order to analyze its heat transfer performance and to obtain data at the actuator orifice that can be used as a boundary condition for simplified models. This data will

be compared to that of open configuration synthetic jets found in the literature. Moreover, literature has revealed fundamental differences in the flow field for different actuator geometries. Another objective of this work is to help understand the differences between the flows at different actuator geometries and to assess the implication of the actuator geometry to the conditions at the actuator orifice in enclosed configurations.

An accurate model of a synthetic jet actuator, based in its governing parameters, that accurately describes the cavity and the membrane and, therefore, enables a realistic simulation of the turbulence will be developed as a second objective of this dissertation. Then, simpler actuator models can be analyzed and compared with the aforementioned model. This will allow to validate less expensive simulations of synthetic jet actuators performed with simpler models. These validations are expected to be useful for coupled simulations between the synthetic jet and the external flows.

The scope of this dissertation is the study of turbulent flows generated by a synthetic jet actuator as well as the external flows that interact with the synthetic jet flow. It is also part of the scope of this doctoral thesis the modeling of the actuator membrane using mesh moving techniques. The modeling of the electromechanical parts of the membrane is out of the scope of this thesis. The proposed studies shall be performed by means of numerical analysis; experimental data shall be obtained from the literature. This work shall use parallel Computational Fluid Dynamics codes to perform the numerical analyses. It is not part of the scope of this dissertation their development, neither the implementation of new turbulence models. It is part of the scope of this work the implementation of sequential and parallel post-processing and visualizing tools and their subsequent validation.

1.3 Approach and Outline

The following technical approach has been employed in this work to reach the aforementioned objectives. First, a literature review is performed in this chapter in order to gain insight on the state-of-the-art of SJA and to obtain a formulation of the problem that is in line with the other authors. In addition, different numerical methodologies employed in the literature are examined as well as the application of SJA to real engineering problems, which can benefit of the present work. Next, Chapter 2 presents a detailed mathematical model that is used in this dissertation. As aforementioned, this model takes into account the movement of the actuator membrane and is formulated with the non-dimensional parameters derived from the Navier-Stokes equations that have been identified to govern the SJA flow. This model is based on the jet formation criteria, which is a key parameter of the flow and has strong implications in the flow morphology. This is followed by a thorough description of the turbulence models employed in this work, i.e., Reynolds averaged

methods, large-eddy simulations and direct numerical simulations, as well as the implications of using energy preserving schemes to model the flow. This is the subject of Chapter 3.

The results discussion part presents and extends the findings in [17, 19]. Chapter 4 describes the computational grids used in this work as well as the extensive validation performed on such grids in order to assure convergence to the solution, in both space and time. This is followed by an extensive description of the dynamics of synthetic jet flow. Two configurations are studied: a slotted and a circular geometry, with $Re = 50$ and $Re = 500$ taken as representatives of the flow. This is the subject of Chapter 5. Then, Chapter 6 analyzes the heat transfer performance of enclosed synthetic jets at the two mentioned configurations, closely relating the results with the flow description of the previous chapter. Finally, the findings of this dissertation are summarized in Chapter 7 and some further research points are outlined.

I

Mathematical and Numerical Description

2

Mathematical Model for Synthetic Jet Actuators

This chapter presents a detailed mathematical model used in this work for synthetic jet actuators that takes into account the cavity membrane movement. It corresponds to a variation of the M1 model presented in Section 1.1.4 and takes into account the non-dimensional parameters that govern the SJA flow (i.e., Re and Sk), derived from a dimensional analysis of the Navier-Stokes equations. Two SJA configurations are presented: the slotted and the circular. The mathematical model developed is generic so is used for both configurations. The definition of the jet formation criteria in Eq. 1.3 is expanded in order to find a relationship with the driving and geometric parameters of a SJA. The JFC is found to be a key parameter in the SJA flow that has strong implications in the resulting flow, which is further illustrated with precursory simulations. In addition, several actuator membrane models found in the literature are presented and analyzed. This model is developed under the hypothesis of incompressibility, therefore, the Helmholtz frequency condition is presented and verified.

2.1 Geometry and Configurations Studied

The configurations studied, shown in Fig. 2.1, represent two different simplified actuator configurations: Fig. 2.1a corresponds to a rectangular actuator in an homogeneous domain in the x_3 direction (henceforth slotted configuration) while Fig. 2.1b corresponds to a circular actuator (or axisymmetric configuration). The fluid enters and leaves the actuators through a channel of length b due to the oscillation of their membranes, thus creating a jet. These jets impinge on a uniformly

heated wall located at an orifice-to-surface distance of $H/d = 5$, which has been imposed based on the optimal distances for cooling applications [20, 26, 48], causing convective heat transfer from the wall to the jet. The discharge cavity of length L is large enough so as to not interfere with the developing and propagation of the jet. Moreover, depth of $D/d = 6$ is considered for the slotted configuration to allow the full development of the three-dimensional flow. Finally, the dimensionless actuator cavity width W/d is set accordingly so as to impose a jet formation criteria of 3 (see Section 2.4). The other dimensions of the SJA are selected as in Liu [81], with $b/d = 0.3$ and $B/d = 1.67$. All these dimensions are summarized in Table 2.1.

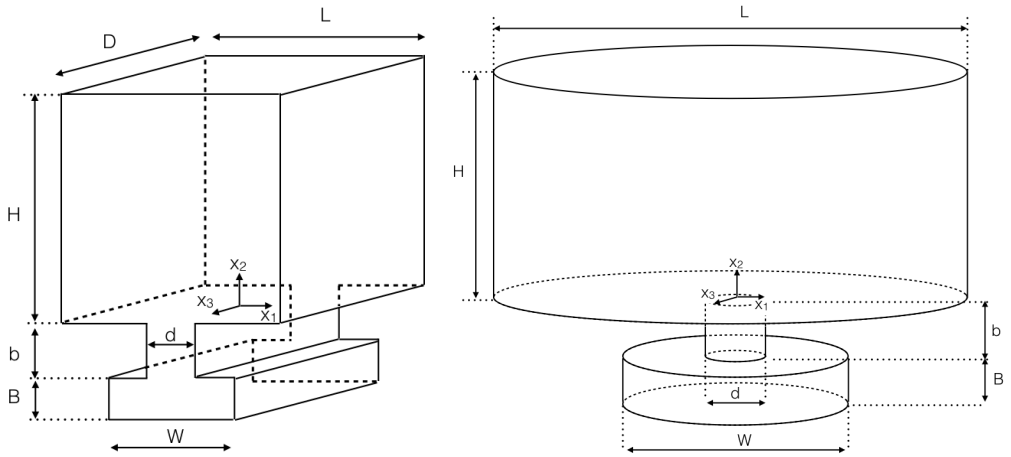

(a) Slotted. (b) Axisymmetric.

Figure 2.1: Geometry of the analyzed configurations (not to scale).

Table 2.1: Summary of the dimensions presented in the configuration on Fig. 2.1

	Slotted	Circular
W/d	23.5619	4.8541
H/d	5	5
L/d	60	60
A/d	0.2	0.2
B/d	5/3	5/3
b/d	1/3	1/3
D/d	6	-

Regarding the actuator's natural resonating frequency, i.e., the Helmholtz frequency, it is proportional to the area of the opening port of the cavity and inversely proportional to the cavity volume and neck length [18], with the constant of proportionality being the speed of sound. Hence, for a slotted or rectangular cavity and orifice

$$f_h = \frac{v_{sound}}{2\pi}\sqrt{\frac{d\,w}{W w\,Bb}}, \tag{2.1}$$

where v_{sound} is the speed of sound of the considered fluid. For round or axisymmetric configurations, the term $3/4$ [18] appears inside the square root as a consequence of the area ratio, as

$$f_h = \frac{v_{sound}}{2\pi}\sqrt{\frac{3}{4}\frac{d\ w}{W w\ Bb}}. \tag{2.2}$$

Note that the dimensions correspond to those shown in Fig. 2.1. Assuming a reasonable actuator exit orifice of $d = 1$ mm, the ratios presented on Table 2.1 and standard air properties, the actuator driving frequency divided by the Helmholtz frequency f_0/f_h is plotted for different Reynolds numbers in Fig. 2.2 for both the slotted and round configurations. Under these circumstances and for the slotted configuration, incompressible treatment is possible for $Re < 5000$; while for the round configuration it is a good approximation for $Re < 10000$.

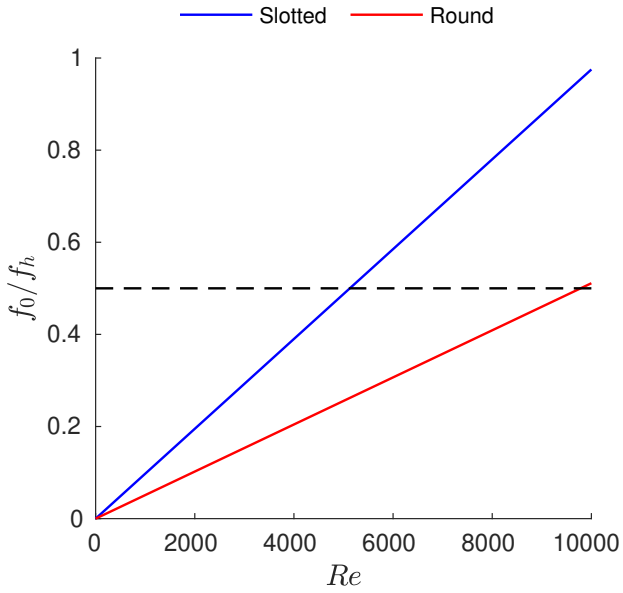

Figure 2.2: Ratio of the actuator driving frequency f_0 and the natural resonance frequency f_h for various Reynolds numbers and an orifice exit diameter of $d = 1$ mm.

2.2 Dimensional Analysis of the Governing Equations

The Navier-Stokes and energy equations are used to model the flow. Incompressible regime is assumed since the ratio between the Helmholtz frequency of the actuator and the driving frequency is assumed to be less than 0.5, as previously explained. This study focuses on situations where the jet velocity is high enough to disregard natural convection, i.e., the Richardson (Ri) number, defined as the ratio of the buoyancy term to the flow shear term, is low enough. Experimental and numerical studies [54] show that buoyancy effects become relevant for $Ri > 0.01$. Moreover,

thermal radiation has also been neglected. Under these assumptions, the incompressible Navier-Stokes equations are

$$\frac{\partial u_j}{\partial x_j} = 0, \tag{2.3}$$

$$\frac{\partial u_i}{\partial t} + \frac{\partial \left(u_i u_j\right)}{\partial x_j} = -\frac{1}{\rho}\frac{\partial p}{\partial x_i} + \frac{\partial}{\partial x_j}\left[\nu\left(\frac{\partial u_i}{\partial x_j} + \frac{\partial u_j}{\partial x_i}\right)\right], \tag{2.4}$$

$$\frac{\partial T}{\partial t} + \frac{\partial \left(u_j T\right)}{\partial x_j} = \frac{\partial}{\partial x_j}\left(\frac{k}{\rho c_p}\frac{\partial T}{\partial x_j}\right), \tag{2.5}$$

where x_i are the spatial coordinates (or x, y and z), u_i are the cross-stream, stream-wise and span-wise velocity components (or u, v, w), p is the pressure and T is the temperature. ρ is the density, ν is the kinematic viscosity, c_p is the specific heat coefficient at constant pressure and k is the thermal conductivity of the fluid.

The following non-dimensional magnitudes are defined in order to perform a dimensional analysis of Eqs. 2.3 to 2.5

$$\widehat{x}_i = \tfrac{x_i}{d}, \quad \widehat{u}_i = \tfrac{u_i}{U_0}, \quad \widehat{t} = 2\pi f_0 t, \quad \widehat{p} = \tfrac{p}{\rho U_0^2},$$

where $\widehat{\cdot}$ denotes a non-dimensional field and d is the SJA outlet orifice diameter, f_0 is the membrane oscillating frequency and U_0 a characteristic velocity. They are rewritten as

$$x_i = d\widehat{x}_i, \quad u_i = U_0\widehat{u}_i, \quad t = \tfrac{t}{2\pi f_0}, \quad p = \rho U_0^2 \widehat{p},$$

so that they can be plugged into Eqs. 2.3 and 2.4 to obtain a non-dimensional form. Eq. 2.4 becomes as follows after including the aforementioned non-dimensional variables

$$\frac{2\pi f d}{U_0}\frac{\partial \widehat{u}_i}{\partial \widehat{t}} + \widehat{u}_j\frac{\partial \widehat{u}_i}{\partial \widehat{x}_j} = -\frac{\partial \widehat{p}}{\partial \widehat{x}_i} + \frac{\partial}{\partial \widehat{x}_j}\left[\frac{\nu}{U_0 d}\left(\frac{\partial \widehat{u}_i}{\partial \widehat{x}_j} + \frac{\partial \widehat{u}_j}{\partial \widehat{x}_i}\right)\right]. \tag{2.6}$$

The non-dimensional form of the continuity equation (Eq. 2.3) is simple to obtain, thus it is not treated in depth.

Two non-dimensional numbers are obtained from the analysis of Eq. 2.6, the Reynolds (Re) number and Strouhal (Sr) number, which are defined along the standard set by Smith and Glezer [10] as

$$Re = \frac{U_0 d}{\nu}, \tag{2.7}$$

$$Sr = \frac{2\pi f_0 d}{U_0}. \tag{2.8}$$

Then, Eq. 2.6 can be rewritten as

$$Sr\frac{\partial \widehat{u}_i}{\partial \widehat{t}} + \widehat{u}_j\frac{\partial \widehat{u}_i}{\partial \widehat{x}_j} = -\frac{\partial \widehat{p}}{\partial \widehat{x}_i} + \frac{\partial}{\partial \widehat{x}_j}\left[\frac{1}{Re}\left(\frac{\partial \widehat{u}_i}{\partial \widehat{x}_j} + \frac{\partial \widehat{u}_j}{\partial \widehat{x}_i}\right)\right] \tag{2.9}$$

and thus the non-dimensional form of the momentum equation is obtained.

Concerning the energy equation, the non-dimensional temperature field is defined as

$$\widehat{T} = \frac{T - T_\infty}{T_{wall} - T_\infty}, \tag{2.10}$$

where T_{wall} denotes the temperature at the heated wall and T_∞ the bulk temperature. Then, the dimensional temperature is $T = (T_{wall} - T_\infty)\widehat{T} + T_\infty$ and when plugged into Eq. 2.5, it becomes

$$\frac{2\pi f d}{U_0}\frac{\partial \widehat{T}}{\partial \widehat{t}} + \widehat{u}_j \frac{\partial \widehat{T}}{\partial \widehat{x}_j} = \frac{\partial}{\partial \widehat{x}_j}\left(\frac{k}{\rho \nu c_P}\frac{\nu}{U_0 d}\frac{\partial \widehat{T}}{\partial \widehat{x}_j}\right) \tag{2.11}$$

Another non-dimensional number, the Prandtl (Pr) number

$$Pr = \frac{\rho \nu c_P}{k}, \tag{2.12}$$

is obtained from Eq. 2.11 and allows to rewrite it as

$$Sr\frac{\partial \widehat{T}}{\partial \widehat{t}} + \widehat{u}_j \frac{\partial \widehat{T}}{\partial \widehat{x}_j} = \frac{\partial}{\partial \widehat{x}_j}\left(\frac{1}{PrRe}\frac{\partial \widehat{T}}{\partial \widehat{x}_j}\right). \tag{2.13}$$

Therefore, the non-dimensional incompressible Navier-Stokes equations that govern the flow field for synthetic jets have been obtained. Putting them together they are

$$\frac{\partial \widehat{u}_j}{\partial \widehat{x}_j} = 0, \tag{2.14}$$

$$Sr\frac{\partial \widehat{u}_i}{\partial \widehat{t}} + \widehat{u}_j \frac{\partial \widehat{u}_i}{\partial \widehat{x}_j} = -\frac{\partial \widehat{p}}{\partial \widehat{x}_i} + \frac{\partial}{\partial \widehat{x}_j}\left[\frac{1}{Re}\left(\frac{\partial \widehat{u}_i}{\partial \widehat{x}_j} + \frac{\partial \widehat{u}_j}{\partial \widehat{x}_i}\right)\right], \tag{2.15}$$

$$Sr\frac{\partial \widehat{T}}{\partial \widehat{t}} + \widehat{u}_j \frac{\partial \widehat{T}}{\partial \widehat{x}_j} = \frac{\partial}{\partial \widehat{x}_j}\left(\frac{1}{PrRe}\frac{\partial \widehat{T}}{\partial \widehat{x}_j}\right). \tag{2.16}$$

2.3 Actuator Membrane Model

The position of the SJA membrane is a combination of the forces that drive the membrane and the forces produced by the fluid. Detailed models have been elaborated in the literature, e.g., using lumped element modeling to investigate the behavior of the piezoelectric components [36, 82]. Generally speaking, the membrane movement can be modeled using a time-dependent sinusoidal function and a space-dependent profile function $\delta(r)$ as

$$x_2 = -\delta(r)\cos(2\pi f_0 t), \tag{2.17}$$

where r is the local radius as $r = x_1$ or $r = \sqrt{x_1 + x_3}$ for the slotted and axisymmetric configurations respectively. The parameter $\delta(r)$ is what defines the shape of the membrane. Several models are present in the literature:

- Blevins [83] derived an expression to approximate the shape and mode of vibrating structures as

$$\delta(r) = \delta_C \left[J_0\left(\frac{\lambda r}{W/2}\right) - \frac{J_0(\lambda)}{I_0(\lambda)} I_0\left(\frac{\lambda r}{W/2}\right) \right], \tag{2.18}$$

  where δ_C is a scaling parameter, J_0 the modified Bessel function of the first kind, I_0 the Bessel function of the first kind and λ a dimensionless parameter taken as $\lambda = 10.22^{1/2}$.

- A profile derived from theory of plates and shells is proposed to model the membrane shape by Mane et al. [84]

$$\delta(r) = \frac{\delta_C}{2} \left[1 - \frac{4r^2}{W^2} + \frac{8r^2}{W^2} \ln\left(\frac{2r}{W}\right) \right]. \tag{2.19}$$

  The profile presented in Eq. 2.19 is used in the recent works of Hatami et al. [25, 85] to model the actuator membrane.

- After conducting Detailed experimental and numerical analysis of the actuator membrane displacement, Mane et al. also proposed an expression measured from experimental data, obtained by regressing a 2nd grade polynomial

$$\delta(r) = \delta_C \left(1 - \left(\frac{r}{W/2}\right)^2 \right). \tag{2.20}$$

  It is claimed that it achieves better results when the function in Eq. 2.19 does not give a good enough approximation.

- A rather simple yet efficient profile function is proposed by Xia and Qin [56] where the membrane shape is modeled as a cosine function of the membrane radius

$$\delta(r) = \delta_C \cos\left(\pi \frac{r}{W}\right). \tag{2.21}$$

  This approach is successfully used in the works of Miro et. al. [17, 19, 61] and this work to model the SJA membrane.

Then, a mean actuator amplitude can be defined as

$$\overline{A} = \frac{1}{S_W} \int_{S_W} \delta(r)\, dS \tag{2.22}$$

where S_W is the surface of the actuator membrane (see Fig. 2.1). This allows to set a certain value of δ_C so that the profile functions presented in Eqs. 2.18 to 2.21 have the same integrated

$\overline{A}$. Expressions for δ_C are obtained by integrating analytically Eq. 2.22 and are shown in Table 2.2 for both slotted and circular shaped actuators.

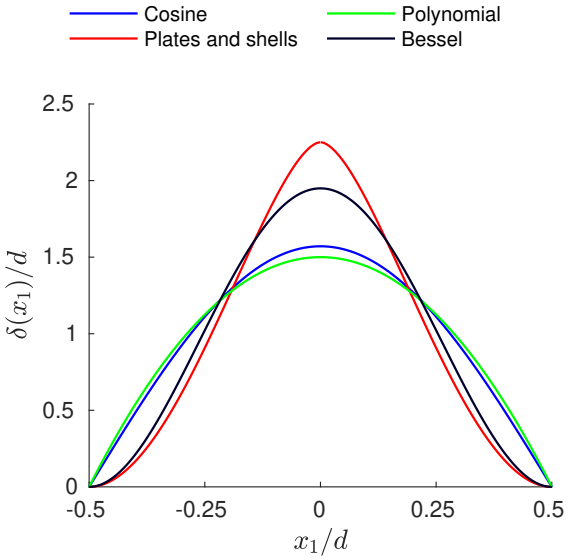

Figure 2.3: Membrane profile functions for a slotted actuator.

Table 2.2: Values of the scaling parameter δ_C after integrating the profile functions using Eq. 2.22.

$\delta_C =$	Slotted	Axisym.
Bessel, Eq. 2.18	$1.846\ \overline{A}$	$3.041\ \overline{A}$
Plates and shells, Eq. 2.19	$9/2\ \overline{A}$	$8\ \overline{A}$
Polynomial, Eq. 2.20	$3/2\ \overline{A}$	$2\ \overline{A}$
Cosine, Eq. 2.21	$\pi/2\ \overline{A}$	$\pi^2/(4\pi-8)\ \overline{A}$

A comparative of the different profile functions for a slotted actuator is given in Fig. 2.3, whereas for a circular actuator is given in Fig. 2.4. Clearly, the models described by Eqs. 2.18 and 2.19 present a similar shape whereas the models in Eqs. 2.20 and 2.21 are also similar. Blevins model is cumbersome to implement and does not present an easy analytical integral on Eq. 2.22 (although it can be done numerically). On the other hand, the cosine model presents a good approximation to the membrane shape and is simple enough to be implemented as a boundary condition. For this reasons, the cosine model is preferred in this work. Moreover, the polynomial profile function (derived from experimental data) that has been proven to give good results does not differ much from the cosine profile function.

As already mentioned in Section 1.1.4, imposing the movement of the actuator membrane using a M1 model allows imposing physically realistic boundary conditions for the momentum (no-slip) and energy equations (either a Dirichlet $T = T^*$ or a Neumann $\partial T/\partial n = q^*$ condition). Eqs. 2.18 to 2.21 are examples of some expressions for modeling such movement. A condition for u_i at the membrane position, i.e., model M2 can be obtained from the derivative of Eq. 2.17 with respect to time and the profile functions of Eqs. 2.18 to 2.21. Regarding M3 models, a constant (top hat) profile for u_i is usually preferred in the literature, thus favoring simplicity. For a parabolic velocity profile at the orifice and under incompressible flow, a condition can be derived assuming continuity between the membrane and the orifice as

$$\int_{S_d} u_2\left(x_1, x_3, t\right)\ dS = \int_{S_W} \frac{\partial x_2}{\partial t}\ dS, \tag{2.23}$$

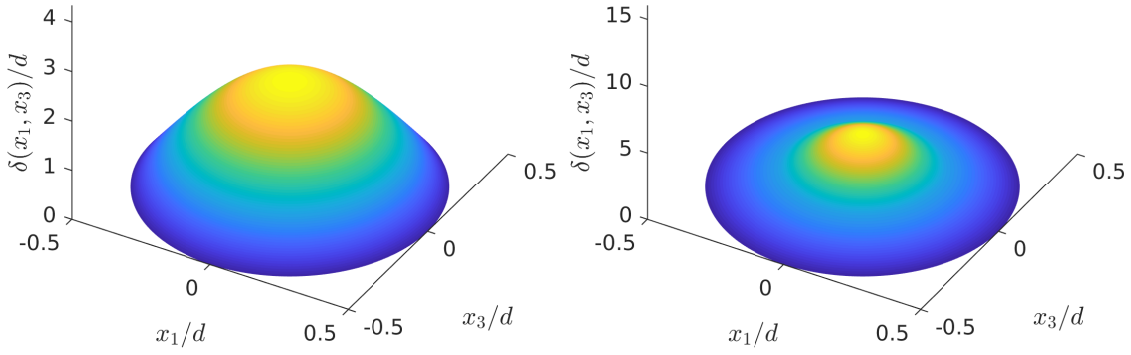

(a) Cosine model.

(b) Plates and shells model.

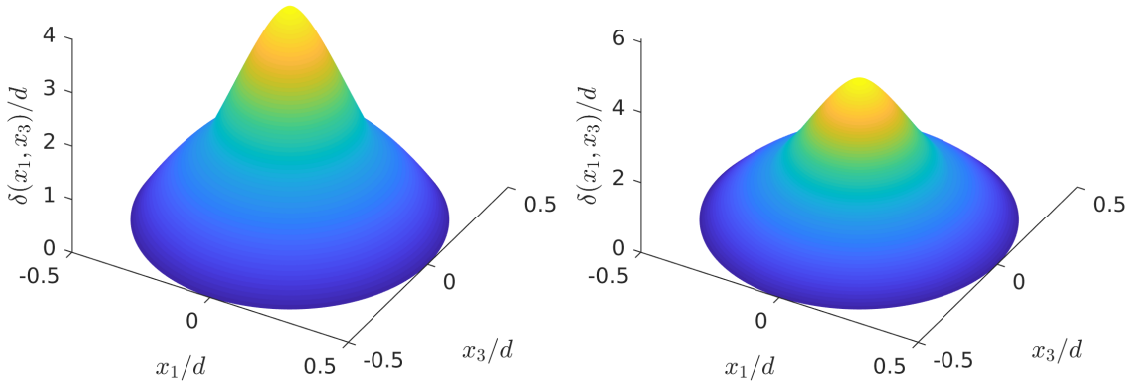

(c) Polynomial model.

(d) Bessel model.

Figure 2.4: Membrane profile functions for a circular membrane.

where $u_2\left(x_1, x_3, t\right)$ is the velocity profile at the orifice lips. Taking into account that only the term that describes the shape is affected by the integral and using Eq. 2.22, it can be written that

$$\int_{S_d} \delta_2(r)\ dS = S_W \overline{A}, \tag{2.24}$$

where $\delta_2(r)$ is the parabola profile function using a description similar to that of Eq. 2.17 for $u_2\left(x_1, x_3, t\right)$. Then, using a similar approach to the one used in Eq. 2.22,

$$\overline{A}_2 = \frac{S_W}{S_d}\overline{A}, \tag{2.25}$$

where $\overline{A}_2$ is the mean amplitude of the parabolic profile. Eq. 2.25 basically states in which fraction the amplitude at the orifice needs to be increased due to the difference of geometry between the actuator cavity and the actuator neck. Note that, for a constant (top-hat) profile,

$$u_2\left(t\right) = 2\pi f_0 \frac{S_W}{S_d}\overline{A}\sin\left(2\pi f_0 t\right), \tag{2.26}$$

is exactly the velocity at the orifice that is consistent with the formulation presented in this section.

2.4 Analysis of the Governing Parameters

It is now of interest to analyze how the actuator model can be included into the dimensional analysis presented in Section 2.2, and its effect to the governing parameters of the synthetic jet flow. As aforementioned, a characteristic velocity (U_0) is defined in terms of the stroke length L_0 as $U_0 = L_0 f_0$. The stroke length is defined according to Eq. 1.1 as

$$L_0 = \int_0^{\tau/2} u_0(t)\ dt$$

where $u_0(t)$ is the orifice exit velocity over the ejection part of the cycle, which corresponds to the half of the actuation period τ. Therefore, U_0 is expressed as

$$U_0 = \frac{1}{\tau}\int_0^{\tau/2} u_0(t)\ dt, \tag{2.27}$$

where the relationship $f_0 = 1/\tau$ has been used. It was firstly assumed that $u_0(t)$ had a slug shape [10]. Later, in [86] it was argued that, because of the shape difference of the spatial velocity profile with the assumed slug shape, it is more accurate to define $u_0(t)$ using the spatial-averaged velocity at the exit, so that

$$u_0(t) = \frac{1}{S_d}\int_{S_d} u_2(x_1, x_3, t)\ dS, \tag{2.28}$$

where S_d is the surface of the exit orifice (see Fig. 2.1) and $u_2(x_1, x_3, t)$ the velocity at the orifice exit, as defined in Section 2.3. Hence,

$$U_0 = \frac{1}{\tau}\frac{1}{S_d}\int_0^{\tau/2}\int_{S_d} u_2(x_1, x_3, t)\; dS\; dt, \tag{2.29}$$

Other authors [15, 32] prefer to use a time and space averaged velocity ($\overline{U}$) at the SJA exit during the expulsion stroke that corresponds to

$$\overline{U} = \frac{2}{\tau}\frac{1}{S_d}\int_0^{\tau/2}\int_{S_d} u_2(x_1, x_3, t)\; dS\; dt, \tag{2.30}$$

where S_d is the surface of the exit orifice (see Fig. 2.1). It is easy to show from Eqs. 2.29 and 2.30 that the relationship between both characteristic velocities is $\overline{U} = 2U_0$. Moreover, these authors prefer to use the Stokes (Sk) number, defined as

$$Sk = \sqrt{\frac{2\pi f d^2}{\nu}}, \tag{2.31}$$

and is used to characterize the flow as an alternative to the Strouhal number presented in Section 2.2. Let us recall that the jet formation criteria (JFC) in Eq. 1.3 is defined using $\overline{U}$ for the Reynolds and Strouhal numbers as

$$\text{JFC} = \frac{1}{Sr_{\overline{U}}} = \frac{Re_{\overline{U}}}{Sk^2} = \frac{2Re}{Sk^2}.$$

The relationship between the JFC and the dimensionless stroke length L_0/d can be proven to be

$$\text{JFC} = \frac{1}{\pi}\frac{L_0}{d}. \tag{2.32}$$

Therefore, the JFC and the dimensionless stroke length differ from a constant and are equivalent parameters for characterizing the SJA flow. Regarding the definition of the Reynolds number based on the stroke length Re_{L_0} of Eq. 1.4, it can be shown that

$$Re_{L_0} = Re\frac{L_0}{d} = \pi \text{JFC} Re. \tag{2.33}$$

Hence, this parameter combines the effects of the jet formation and the Reynolds number in one single parameter.

The membrane vertical position can be modeled as presented in Section 2.3, using Eq. 2.17 to compute its position with any of the proposed profile functions. Then, the instantaneous velocity

at the actuator membrane is found by performing the time derivative of Eq. 2.17 and obtain

$$\frac{dx_2}{dt} = 2\pi f_0 \delta(r) \sin(2\pi f_0 t). \tag{2.34}$$

Then, under incompressible regime, the velocity at the actuator membrane is related to the velocity at the orifice exit by applying continuity, hence,

$$\int_{S_d} u_2(x_1, x_3, t)\ dS = \int_{S_W} 2\pi f_0 \delta(r) \sin(2\pi f_0 t)\ dS. \tag{2.35}$$

The integral on the right-hand side is only applied over $\delta(r)$ and using the definition of the mean actuator amplitude of Eq. 2.22 the following expression is obtained

$$\int_{S_d} u_2(x_1, x_3, t)\ dS = 2\pi f_0 \overline{A} S_W \sin(2\pi f_0 t), \tag{2.36}$$

which is directly plugged into Eq. 2.29

$$U_0 = \frac{1}{\tau}\frac{S_W}{S_d}\int_0^{\tau/2} 2\pi f_0 \overline{A} \sin(2\pi f_0 t)\ dt. \tag{2.37}$$

This expression can now be integrated in time, resulting

$$U_0 = 2\overline{A} f_0 \frac{S_W}{S_d}. \tag{2.38}$$

Therefore, the characteristic velocity is related to the mean amplitude and the driving frequency, coupling f_0 and U_0.

Let us then plug Eq. 2.38 into Eqs. 2.7 and 2.8 to find new expressions for the Reynolds and Strouhal numbers

$$Re = \frac{2\overline{A} f_0 d}{\nu}\frac{S_W}{S_d}, \tag{2.39}$$

$$Sr = \pi \left(\frac{\overline{A}}{d}\right)^{-1} \left(\frac{S_W}{S_d}\right)^{-1}. \tag{2.40}$$

The Reynolds number based on the stroke length Re_{L_0} becomes

$$Re_{L_0} = \frac{4\overline{A} f_0}{\nu}\left(\frac{S_W}{S_d}\right)^2, \tag{2.41}$$

and has clear dependences on the driving parameters ($\overline{A}$ and f_0), the fluid parameters (ν) and the cavity geometric parameters (S_W and S_d). Also, under this definition, the jet formation criteria

becomes a purely geometrical parameter.

$$\text{JFC} = \frac{2}{\pi}\left(\frac{\overline{A}}{d}\right)\left(\frac{S_W}{S_d}\right). \tag{2.42}$$

Therefore, as observed by Smith and Glezer [10], when the motion of the actuator membrane is time-harmonic the formation parameters of the jet depend only on the amplitude of the actuator, and cannot be varied independently.

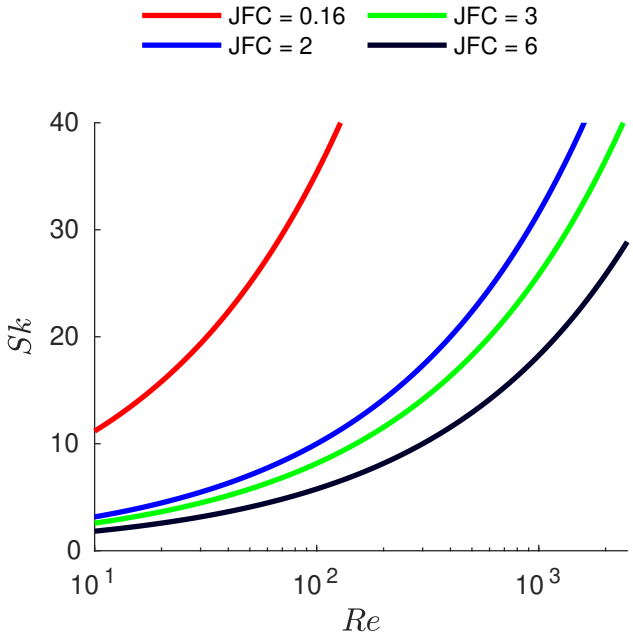

Figure 2.5: Evolution of the jet formation criteria with the Stokes and Reynolds numbers.

The variation of the jet formation criteria in Eq. 2.42 is plotted in function of the Stokes and Reynolds numbers in Fig. 2.5. Slotted jets with a combination of Re and Sk over the blue line do not form whereas circular jets with Re and Sk over the red line do not form. High amplitudes and large jet cavity aspect ratios favor the formation of jets, independently of the frequency, while changing the drive frequency has no effect on the JFC. Changing the drive frequency can be interpreted in Fig. 2.5 as moving along a certain line without the possibility to jump to others.

Figs. 2.6 and 2.7 show precursory simulations using the aforementioned mathematical model of the slotted and circular configurations at different Re and using the JFC represented in Fig. 2.5. The effect of the JFC can be clearly seen: at the same Re, if the JFC is low enough, the jet is indeed not formed. On the other hand, increasing the JFC has implications in the impinging area and the two recirculation vortices that are created. Moreover, the cavity flow also changes with the JFC. Another difference between Figs. 2.6 and 2.7 is the difference on the jet morphology between the slotted and circular configuration. This topic is further discussed in Chapter 5.

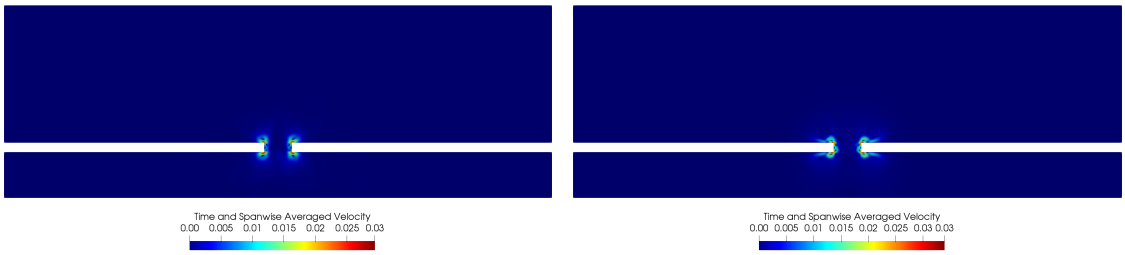

(a) JFC $= 0.1$

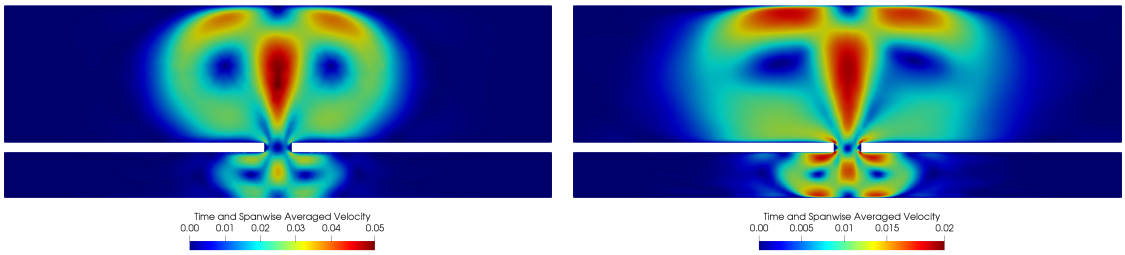

(b) JFC $= 2$

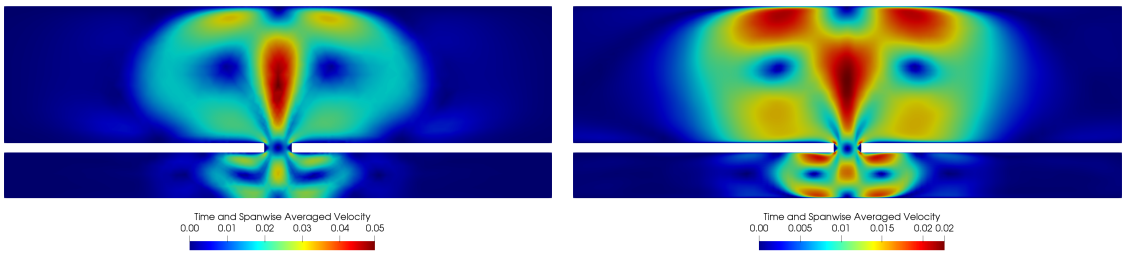

(c) JFC $= 6$

Figure 2.6: Effect of the jet formation criteria in the slotted geometry for $Re = 50$ (top) and $Re = 500$ (bottom).

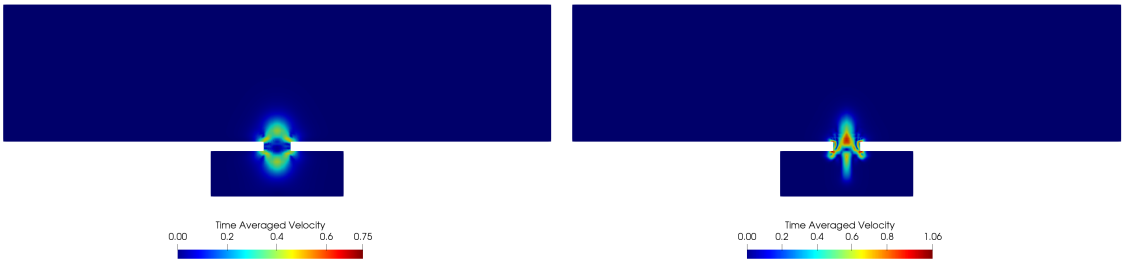

(a) JFC $= 0.1$

(b) JFC $= 2$

(c) JFC $= 6$

Figure 2.7: Effect of the jet formation criteria in the circular geometry for $Re = 50$ (top) and $Re = 500$ (bottom).

3

Turbulence Modeling

In the study of turbulent flows, the main goal is to obtain a tractable quantitative model that can be used to calculate quantities of interest and practical relevance, e.g., the heat transfer produced by an impinging synthetic jet. The problem is not easy and numerical models calculated by computers (or supercomputers) are needed to perform a calculation on relevant properties of turbulent flows. The largest turbulent motions are almost as large as the characteristic width of the flow, thus directly affected by the geometry. The smaller scales decrease as $Re^{-1/2}$ for the time-scales and $Re^{-3/4}$ for the length-scales. Moreover, difficulties arise from the nonlinear convective term of the Navier-Stokes equations and much more from the pressure-gradient term.

Therefore, this chapter is dedicated to synthesize some of the most relevant methods available in the literature for the study of turbulent flows. These methods have been applied to analyze the impingement of turbulent synthetic jets by means of parallel codes such as Alya or *Code_Saturne*. Alya [87] is based on the Finite Element method, and uses a fractional step approach to solve the pressure-velocity coupling and an explicit fourth-order Runge-Kutta time integration scheme; while *Code_Saturne* [88] is based on the Finite Volume method, and also uses a fractional step to solve the pressure-velocity with a second-order centered scheme as spatial discretization and an implicit second-order Crank-Nicholson time integration scheme. Both codes are designed for large-scale parallel applications [89, 90].

This chapter includes a review on Reynolds-Averaged methods and Large-Eddy Simulations, and the models used in this work are clearly detailed. Then Direct Numerical Simulation of the Navier-Stokes equations are addressed, discussing why it is prohibitive to be used. Finally, a review of

energy preserving schemes and its importance in turbulence modeling is outlined.

3.1 Modeling of the Navier-Stokes equations using RANS/URANS

The Reynolds-Averaged Navier-Stokes (RANS) equations were derived by Reynolds in 1894 and allow to obtain a representation of the mean flow. Their unsteady counterparts, the Unsteady Reynolds-Averaged Navier-Stokes (URANS) equations enable to obtain a temporal variation for the mean flow. Among the advantages of using this model is the decrease on computational time and mesh size with respect to others such as DNS or LES. On the other hand, the obtained solution is dependent on the RANS closure used; and also the solutions obtained using RANS/URANS do not provide information about the small scales in the fluid.

Nevertheless, they are used in this work to obtain initial maps for more refined flow models. Hence, this section contains a brief explanation on the derivation of the equations and the model used in this work.

3.1.1 The mean flow equations

The RANS equations are based on the mean flow equations. Reynolds assumed that the velocity field u_i can be decomposed into a mean velocity $\overline{u}_i$ and a fluctuation u' as

$$u_i = \overline{u}_i + u'. \tag{3.1}$$

Eq. 3.1 is often known as Reynolds decomposition. From the definition of fluctuation, it must hold that $\overline{u'} = 0$. The mean flow equations are obtained by taking the average and plugging Eq. 3.1 into the Navier-Stokes equations (Eqs. 2.3 to 2.5).

Let us start with the continuity equation. After applying Eq. 3.1 it becomes

$$\frac{\partial \left(\overline{u}_j + u'_j \right)}{\partial x_j} = 0. \tag{3.2}$$

Hence, both fields are solenoidal and

$$\frac{\partial \overline{u}_j}{\partial x_j} = 0, \tag{3.3}$$

$$\frac{\partial u'_j}{\partial x_j} = 0. \tag{3.4}$$

Let us now take the average of the momentum equation

$$\frac{\partial \overline{u}_i}{\partial t} + \frac{\partial \left(\overline{u_i u_j}\right)}{\partial x_j} = -\frac{1}{\rho}\frac{\partial \overline{p}}{\partial x_i} + \frac{\partial}{\partial x_j}\left[\nu\left(\frac{\partial \overline{u}_i}{\partial x_j} + \frac{\partial \overline{u}_j}{\partial x_i}\right)\right]. \tag{3.5}$$

It can be proved that the product $\overline{u_i u_j}$ can be expanded to

$$\overline{u_i u_j} = \overline{u}_i\,\overline{u}_j + \overline{u_i' u_j'} \tag{3.6}$$

by plugging Eq. 3.1 into the aforementioned product and operating. Then, the mean flow Navier-Stokes equations become, after using Eq. 3.6,

$$\frac{\partial \overline{u}_i}{\partial t} + \overline{u}_j\frac{\partial \overline{u}_i}{\partial x_j} + \frac{\partial \overline{u_i' u_j'}}{\partial x_j} = -\frac{1}{\rho}\frac{\partial \overline{p}}{\partial x_i} + \frac{\partial}{\partial x_j}\left[\nu\left(\frac{\partial \overline{u}_i}{\partial x_j} + \frac{\partial \overline{u}_j}{\partial x_i}\right)\right]. \tag{3.7}$$

These set of equations can be rewritten as

$$\frac{\partial \overline{u}_i}{\partial t} + \overline{u}_j\frac{\partial \overline{u}_i}{\partial x_j} = \frac{\partial}{\partial x_j}\left[\nu\left(\frac{\partial \overline{u}_i}{\partial x_j} + \frac{\partial \overline{u}_j}{\partial x_i}\right) - \frac{1}{\rho}\overline{p}\delta_{ij} - \overline{u_i' u_j'}\right]. \tag{3.8}$$

3.1.2 Additional unknowns in RANS

A closer examination on Eq. 3.8 reveals that a new unknown, namely $\overline{u_i' u_j'}$, has appeared. This magnitude is known as the Reynolds stress tensor and, generally speaking, RANS models provide closures for $\overline{u_i' u_j'}$ so that the equations can be computed. This is generally done in the form of additional transport equations, as it will be further seen.

The Reynolds stresses form a second-order symmetric tensor, whose diagonal components are the normal stresses and the off-diagonal components are the shear stresses. The turbulent kinetic energy k is defined as half of the sum of the normal stresses, i.e.,

$$\mathrm{k} = \frac{1}{2}\left(\overline{u_i' u_i'}\right). \tag{3.9}$$

Moreover, the Reynolds stress tensor can be decomposed into an isotropic stress $2/3\mathrm{k}\delta_{ij}$ and a deviatoric anisotropic stress $\overline{u_i' u_i'} - 2/3\mathrm{k}\delta_{ij}$ [91]. According to the turbulent-viscosity hypothesis formulated by Boussinesq, the deviatoric anisotropic part of the Reynolds stress tensor is proportional to the rate of strain by a positive scalar ν_t as

$$-\overline{u_i' u_i'} + \frac{2}{3}\mathrm{k}\delta_{ij} = \nu_t\left(\frac{\partial \overline{u}_i}{\partial x_j} + \frac{\partial \overline{u}_j}{\partial x_i}\right), \tag{3.10}$$

where the scalar ν_t is the turbulent viscosity. Then, Eq. 3.8 can be rewritten in terms of an effective viscosity $\nu_{eff} = \nu + \nu_t$ by means of Eq. 3.10

$$\frac{\partial \overline{u}_i}{\partial t} + \overline{u}_j \frac{\partial \overline{u}_i}{\partial x_j} = \frac{\partial}{\partial x_j}\left[\nu_{eff}\left(\frac{\partial \overline{u}_i}{\partial x_j} + \frac{\partial \overline{u}_j}{\partial x_i}\right)\right] - \frac{1}{\rho}\frac{\partial}{\partial x_j}\left(\overline{p} + \frac{2}{3}\rho \mathrm{k}\right), \tag{3.11}$$

where $\overline{p} + 2/3\rho\mathrm{k}$ can be interpreted as a modified mean pressure. The problem becomes now to find an appropriate definition for ν_t. This can be done by defining a certain characteristic velocity u^* and a certain characteristic length l^* so that

$$\nu_t = u^* l^*. \tag{3.12}$$

Indeed, the turbulent viscosity can be modeled by selecting appropriate characteristic velocity and length (e.g., mixing-length model). However, both Kolmogorov and Prandtl independently suggested that it is advisable to base the characteristic velocity on the turbulent kinetic energy, i.e.,

$$u^* = c_k^{1/2}, \tag{3.13}$$

where c_k is a constant. Therefore, the turbulent kinetic energy must be known or estimated beforehand. In addition, it can be further proved that, at high Reynolds numbers the dissipation rate ε scales as u_0^3/l_0, where u_0 and l_0 are the velocity and length scales of the energy-containing motions. Hence, it is fair to model ε as

$$\varepsilon = c_\varepsilon \mathrm{k}^{3/2}/l^*, \tag{3.14}$$

where c_ε is a constant.

3.1.3 A transport equation for k

A transport equation for the kinetic energy can be obtained by multiplying the Navier-Stokes equations by u_i. Analogously, when the Reynolds equations are multiplied by $\overline{u}_i$, a transport equation for the average kinetic energy is obtained. Therefore, a transport equation for k can be derived by obtaining an equation for the fluctuating velocity, multiplying by u_i' and taking the average [91]. The equation for u_i' is obtained by subtracting the Reyolds equations from the Navier-Stokes equation

$$\frac{\partial\left(u_i - \overline{u}_i\right)}{\partial t} + \frac{\partial\left(u_i u_j - \overline{u_i u_j}\right)}{\partial x_j} = -\frac{1}{\rho}\frac{\partial\left(p - \overline{p}\right)}{\partial x_i} + \frac{\partial}{\partial x_j}\left[\nu\left(\frac{\partial\left(u_i - \overline{u}_i\right)}{\partial x_j} + \frac{\partial\left(u_j - \overline{u}_j\right)}{\partial x_i}\right)\right]. \tag{3.15}$$

Eq. 3.15 can be further simplified by defining a fluctuating pressure field $p' = p - \overline{p}$ and by expanding $u_i u_j - \overline{u_i}\,\overline{u_j} = u_i' u_j' + u_i' \overline{u}_j + u_j' \overline{u}_i - \overline{u_i' u_j'}$ as

$$\frac{\partial u_i'}{\partial t} + \overline{u}_j \frac{\partial u_i'}{\partial x_j} = -\frac{\partial u_i' u_j'}{\partial x_j} - u_j' \frac{\partial \overline{u}_i}{\partial x_j} + \frac{\partial \overline{u_i' u_j'}}{\partial x_j} + \frac{\partial}{\partial x_j}\left(-\frac{p'}{\rho} + 2\nu S_{ij}'\right), \tag{3.16}$$

where the fluctuating rate of strain S_{ij}' is

$$S_{ij}' = S_{ij} - \overline{S}_{ij} = \frac{1}{2}\left(\frac{\partial u_i'}{\partial x_j} + \frac{\partial u_j'}{\partial x_i}\right). \tag{3.17}$$

Then, Eq. 3.16 is multiplied by u_i' to obtain an equation for the fluctuating kinetic energy

$$u_i' \frac{\partial u_i'}{\partial t} + u_i' \overline{u}_j \frac{\partial u_i'}{\partial x_j} = -u_i' \frac{\partial u_i' u_j'}{\partial x_j} - u_i' u_j' \frac{\partial \overline{u}_i}{\partial x_j} + u_i' \frac{\partial \overline{u_i' u_j'}}{\partial x_j} + u_i' \frac{\partial}{\partial x_j}\left(-\frac{p'}{\rho} + 2\nu S_{ij}'\right), \tag{3.18}$$

and taking into account that the fluctuating kinetic energy is $e' = 1/2\ u_i' u_i'$, the following expression is obtained

$$\frac{\partial e'}{\partial t} + \overline{u}_j \frac{\partial e'}{\partial x_j} = -\frac{\partial}{\partial x_j}\left(\frac{1}{2} u_i' u_i' u_j'\right) - u_i' u_j' \frac{\partial \overline{u}_i}{\partial x_j} + u_i' \frac{\partial \overline{u_i' u_j'}}{\partial x_j} + \frac{\partial}{\partial x_j}\left(-\frac{u_i' p'}{\rho} + 2\nu u_i' S_{ij}'\right) - 2\nu S_{ij}' S_{ij}'. \tag{3.19}$$

The average of Eq. 3.19 yields an equation for the turbulent kinetic energy

$$\frac{\partial \mathrm{k}}{\partial t} + \overline{u}_j \frac{\partial \mathrm{k}}{\partial x_j} + \frac{\partial T_j'}{\partial x_j} = -\overline{u_i' u_j'} \frac{\partial \overline{u}_i}{\partial x_j} - 2\nu \overline{S_{ij}' S_{ij}'}, \tag{3.20}$$

where

$$T_j' = \frac{1}{2}\overline{u_i' u_i' u_j'} + \frac{\overline{u_i' p'}}{\rho} - 2\nu \overline{u_i' S_{ij}'}. \tag{3.21}$$

The term $-\overline{u_i' u_j'} \frac{\partial \overline{u}_i}{\partial x_j}$ in is generally positive and thus acts as a source in the transport equation. Therefore, it is called production P and has the following properties:

- Only the symmetric component of the velocity-gradient tensor affects the production, i.e.,

$$\mathrm{P} = -\overline{u_i' u_j'}\,\overline{S_{ij}}. \tag{3.22}$$

- Only the anisotropic a_{ij} part of the Reynolds stress tensor affects the production, i.e.,

$$\mathrm{P} = -a_{ij}\overline{S_{ij}}. \tag{3.23}$$

- The turbulent-viscosity hypothesis is applicable $a_{ij} = -2\nu_t \overline{S_{ij}}$, i.e.,

$$\mathrm{P} = 2\nu_t \overline{S_{ij} S_{ij}}. \tag{3.24}$$

Analogously, the term $2\nu\overline{S'_{ij}S'_{ij}}$ is non-negative and acts as a sink, therefore, it is called dissipation ε. Using these two quantities, Eq. 3.25 can be rewritten as

$$\frac{\partial \mathrm{k}}{\partial t} + \overline{u}_j \frac{\partial \mathrm{k}}{\partial x_j} + \frac{\partial T'_j}{\partial x_j} = \mathrm{P} - \varepsilon. \tag{3.25}$$

3.1.4 Scalar transport equation

The mean scalar transport equation is obtained in a similar manner than the mean flow equations, i.e., the scalar quantity ϕ is decomposed into a mean $\overline{\phi}$ and a fluctuating ϕ' quantity

$$\phi = \overline{\phi} + \phi'. \tag{3.26}$$

Let us take the average of the energy equation

$$\frac{\partial \overline{T}}{\partial t} + \frac{\partial \left(\overline{u_j T}\right)}{\partial x_j} = \frac{\partial}{\partial x_j}\left(\frac{k}{\rho c_p}\frac{\partial \overline{T}}{\partial x_j}\right), \tag{3.27}$$

It can be easily seen that the product $\overline{u_j T}$ is expanded analogously to Eq. 3.6 to obtain

$$\overline{u_j T} = \overline{u}_j\, \overline{T} + \overline{u'_j T'}. \tag{3.28}$$

Then, plugging this relation into Eq. 3.27, it is obtained that

$$\frac{\partial \overline{T}}{\partial t} + \frac{\partial \left(\overline{u}_j\, \overline{T}\right)}{\partial x_j} = \frac{\partial}{\partial x_j}\left(\frac{k}{\rho c_p}\frac{\partial \overline{T}}{\partial x_j} - \overline{u'_j T'}\right), \tag{3.29}$$

where the term $\overline{u'_j T'}$ is unknown and needs to be modeled. This can be done by means of the gradient-diffusion hypothesis [91]. The scalar flux $\overline{u'_j T'}$ vector gives both the direction and the magnitude of the turbulent transport of the temperature field. The gradient-diffusion hypothesis states that this transport is down the mean scalar gradient and there is a positive scalar (Γ_t or turbulent diffusivity) such that

$$\overline{u'_j T'} = \Gamma_t \frac{\partial \overline{T}}{\partial x_j}. \tag{3.30}$$

Therefore, Eq. 3.29 can be rewritten using the gradient-diffusion approach to obtain

$$\frac{\partial \overline{T}}{\partial t} + \frac{\partial \left(\overline{u}_j\, \overline{T}\right)}{\partial x_j} = \frac{\partial}{\partial x_j}\left(\Gamma_{eff}\frac{\partial \overline{T}}{\partial x_j}\right), \tag{3.31}$$

with

$$\Gamma_{eff} = \frac{k}{\rho c_p} + \Gamma_t. \tag{3.32}$$

3.1.5 RANS models

Up to this point, the equations for the mean flow and the scalar transport have been derived. Moreover, a transport equation has been obtained for the turbulent kinetic energy. Thus, the closure problem consists in finding an appropriate relation so that $\nu_t = f(\mathrm{k}, \varepsilon)$ in a similar fashion as in Section 3.1.2. Different closures yield different models, some of which are shown in this work.

The $\mathrm{k} - \varepsilon$ model

The $\mathrm{k} - \varepsilon$ model is a two-equation RANS model in which the turbulent kinetic energy and the dissipation are modeled by transport equations. The model is credited to Jones and Launder[92], with Launder and Sharma[93] providing improved values of the model constants. It consists of (in addition to the turbulent viscosity hypothesis):

- one model transport equation for k.
- one model transport equation for ε.
- specification of the turbulent viscosity as

$$\nu_t = C_\mu \frac{\mathrm{k}^2}{\varepsilon}. \tag{3.33}$$

- modeling T' using the gradient-diffusion hypothesis

$$T' = -\frac{\mu_t}{\sigma_\mathrm{k}} \frac{\partial \mathrm{k}}{\partial x_j}, \tag{3.34}$$

  where σ_k is a constant and is generally taken as $\sigma_\mathrm{k} = 1.0$.

Under these conditions, the standard $k - \varepsilon$ model transport equation for k is

$$\frac{\partial \mathrm{k}}{\partial t} + \overline{u}_j \frac{\partial \mathrm{k}}{\partial x_j} = \frac{\partial}{\partial x_j} \left[\left(\nu + \frac{\nu_t}{\sigma_\mathrm{k}} \right) \frac{\partial \mathrm{k}}{\partial x_j} \right] + 2\nu_t \overline{S_{ij} S_{ij}} - \varepsilon. \tag{3.35}$$

As for the dissipation, an empirical approach is used rather than deriving an exact transport equation. For the standard $k - \varepsilon$ model, the transport equation is

$$\frac{\partial \varepsilon}{\partial t} + \overline{u}_j \frac{\partial \varepsilon}{\partial x_j} = \frac{\partial}{\partial x_j} \left[\left(\nu + \frac{\nu_t}{\sigma_\varepsilon} \right) \frac{\partial \varepsilon}{\partial x_j} \right] + C_{1\varepsilon} \frac{\varepsilon}{\mathrm{k}} \overline{S_{ij} S_{ij}} - 2C_{2\varepsilon} \frac{\varepsilon^2}{\mathrm{k}}, \tag{3.36}$$

where σ_ε, $C_{1\varepsilon}$ and $C_{2\varepsilon}$ are model constants [93]:

$$C_{1\varepsilon} = 1.44, \quad C_{2\varepsilon} = 1.92, \quad C_\mu = 0.09, \quad \sigma_k = 1.0, \quad \sigma_\varepsilon = 1.3,$$

The $\mathrm{k}-\omega$ model

The use of the turbulence frequency $\omega = \varepsilon/\mathrm{k}$ as a second variable was first proposed by Kolmogorov (1942) and developed by Wilcox[94]. The main advantage described by Wilcox over the $\mathrm{k}-\varepsilon$ model is that, for boundary layer flows, the $\mathrm{k}-\omega$ model is both superior in the treatment of the viscous near-wall region and in its treatment of the stream-wise pressure gradients. However, free-stream boundaries are problematic as a non-zero boundary condition for ω is required and the model is sensitive to the value specified.

The transport equation to model k is

$$\frac{\partial \mathrm{k}}{\partial t} + \overline{u}_j \frac{\partial \mathrm{k}}{\partial x_j} = \frac{\partial}{\partial x_j}\left[\left(\nu + \sigma^* \nu_t\right)\frac{\partial \mathrm{k}}{\partial x_j}\right] + 2\nu_t \overline{S_{ij} S_{ij}} - \beta^* k\omega. \tag{3.37}$$

where σ^* and β^* are model constants. Analogously, the model equation for ω reads

$$\frac{\partial \omega}{\partial t} + \overline{u}_j \frac{\partial \omega}{\partial x_j} = \frac{\partial}{\partial x_j}\left[\left(\nu + \sigma \nu_t\right)\frac{\partial \omega}{\partial x_j}\right] + \alpha \frac{\omega}{\mathrm{k}} 2\nu_t \overline{S_{ij} S_{ij}} - \beta\omega^2, \tag{3.38}$$

where σ, α and β are model constants:

$$\alpha = \tfrac{5}{9}, \quad \beta = \tfrac{3}{40}, \quad \beta^* = \tfrac{9}{100}, \quad \sigma = \tfrac{1}{2}, \quad \sigma^* = \tfrac{1}{2}.$$

The model closes by computing the turbulent viscosity as

$$\nu_t = \frac{\nu}{\omega}, \tag{3.39}$$

and the dissipation

$$\varepsilon = \beta^* \omega \mathrm{k}. \tag{3.40}$$

3.1.6 The $\mathrm{k}-\omega$ SST model

Menter proposed and later refined[95] a two-equation model that combines the best behavior of the $\mathrm{k}-\varepsilon$ and the $\mathrm{k}-\omega$ models. It is written as a non-standard $\mathrm{k}-\omega$ model where the final terms are multiplied by a blending function. Close to the walls the blending function is zero (thus becoming the $\mathrm{k}-\omega$ model) and far from the walls the blending function is one (thus becoming the $\mathrm{k}-\varepsilon$ model).

The model equations for the $k-\omega$ SST model are

$$\frac{\partial \mathrm{k}}{\partial t} + \overline{u}_j \frac{\partial \mathrm{k}}{\partial x_j} = \frac{\partial}{\partial x_j}\left[\left(\nu + \sigma_{\mathrm{k}} \nu_t\right)\frac{\partial \mathrm{k}}{\partial x_j}\right] + \mathrm{P}_{\mathrm{k}} - \beta^* k\omega, \tag{3.41}$$

$$\frac{\partial \omega}{\partial t} + \overline{u}_j \frac{\partial \omega}{\partial x_j} = \frac{\partial}{\partial x_j}\left[\left(\nu + \sigma_{\omega} \nu_t\right)\frac{\partial \omega}{\partial x_j}\right] + \frac{\gamma}{\nu_t}\mathrm{P}_{\mathrm{k}} - \beta\omega^2 + 2\left(1 - F_1\right)\frac{\sigma_{\omega 2}}{\omega}\frac{\partial \mathrm{k}}{\partial x_j}\frac{\partial \omega}{\partial x_j}, \tag{3.42}$$

where the production term is

$$\mathrm{P_k} = \mathsf{min}\left(\overline{\tau}_{ij}\frac{\partial \overline{u}_i}{\partial x_j}, 10\beta^*\mathrm{k}\omega\right), \tag{3.43}$$

$$\overline{\tau}_{ij} = 2\nu_t\overline{S}_{ij} - \frac{2}{3}\nu_t\frac{\partial \overline{u}_k}{\partial x_k}\delta_{ij} - \frac{2}{3}\mathrm{k}\delta_{ij}. \tag{3.44}$$

The model is closed by computing the turbulent viscosity as

$$\nu_t = \frac{a_1\mathrm{k}}{\mathsf{max}\left(a_1\omega, SF_2\right)}, \tag{3.45}$$

where $S = \sqrt{2\overline{S_{ij}S_{ij}}}$. Each constant is a blend as $\phi = \phi_1 F_1 + (1 - F_1)\,\phi_2$ and the blending functions are

$$F_1 = \mathsf{tanh}\left(arg_1^4\right), \tag{3.46}$$

$$arg_1 = \mathsf{min}\left[\mathsf{max}\left(\frac{\sqrt{\mathrm{k}}}{\beta^*\omega d}, \frac{500\nu}{d^2\omega}\right), \frac{4\sigma_{\omega 2}\mathrm{k}}{CD_{\mathrm{k}\omega}d^2}\right], \tag{3.47}$$

$$F_2 = \mathsf{tanh}\left(arg_2^2\right), \tag{3.48}$$

$$arg_2 = \mathsf{max}\left(2\frac{\sqrt{\mathrm{k}}}{\beta^*\omega d}, \frac{500\nu}{d^2\omega}\right), \tag{3.49}$$

$$CD_{\mathrm{k}\omega} = \mathsf{max}\left(2\sigma_{\omega 2}\frac{1}{\omega}\frac{\partial \mathrm{k}}{\partial x_j}\frac{\partial \omega}{\partial x_j}, 10^{-10}\right). \tag{3.50}$$

The model constants are

$$\gamma_1 = \tfrac{5}{9}, \quad \gamma_2 = 0.44,$$

$$\begin{aligned} \sigma_{k1} &= 0.85, \quad & \sigma_{\omega 1} &= 0.5, \quad & \beta_1 &= 0.075, \\ \sigma_{k2} &= 1.0, \quad & \sigma_{\omega 2} &= 0.856, \quad & \beta_2 &= 0.0828, \\ \sigma^* &= 0.09, \quad & a_1 &= 0.31. \end{aligned}$$

3.2 Modeling of the Navier-Stokes equations using LES

Large-eddy simulations (LES) were proposed as early as 1963 by Joseph Smagorinsky and consist on applying a spatial average (a low pass filtering) to model the effects if the smaller-scale motions (which have, to some extent, a similar behavior) while the larger turbulent scales (which are affected by the flow configuration) are directly represented [91]. It is motivated by the the limitations of both DNS and RANS. LES can be expected to be more accurate and reliable than RANS for flows in which the large scales of turbulent motion are significant, e.g., the vortex shedding of synthetic jet

actuators. In terms of computational cost, although being quite expensive, it lies in between DNS and RANS.

There are four key concepts in LES:

- A filtering operation is defined to decompose the velocity field as $u_j = \widetilde{u}_j + u'_j$, where $\widetilde{u}_j$ is the filtered velocity and u'_j the sub-grid scale (SGS) velocity. The filtered velocity represents the motion of the larger eddies.
- The equations are derived from the Navier-Stokes equations, with the momentum equation containing the SGS stress tensor and the energy equation the SGS scalar flux.
- Closure is obtained by modeling the SGS stress tensor using an eddy-viscosity model.
- By selecting a small enough filter, the standard Navier-Stokes equations are recovered.

3.2.1 The filtered equations

The filtered continuity equation is

$$\frac{\partial\left(\widetilde{u}_j + u'_j\right)}{\partial x_j} = 0, \tag{3.51}$$

hence, both the filtered velocity and the SGS velocity are solenoidal

$$\frac{\partial \widetilde{u}_j}{\partial x_j} = 0, \tag{3.52}$$

$$\frac{\partial u'_j}{\partial x_j} = 0. \tag{3.53}$$

Then, the filter is applied to the momentum equation in a similar way the average is applied to the mean flow equations

$$\frac{\partial \widetilde{u}_i}{\partial t} + \frac{\partial\left(\widetilde{u_i u_j}\right)}{\partial x_j} = -\frac{1}{\rho}\frac{\partial \widetilde{p}}{\partial x_i} + \frac{\partial}{\partial x_j}\left[\nu\left(\frac{\partial \widetilde{u}_i}{\partial x_j} + \frac{\partial \widetilde{u}_j}{\partial x_i}\right)\right], \tag{3.54}$$

where the nonlinear term can be decomposed as $\widetilde{u_i u_j} = \widetilde{u}_i\widetilde{u}_j + \widetilde{u'_i u'_j}$. The latter term, $\widetilde{u'_i u'_j}$ is called the SGS stress tensor and is usually denoted as $\mathcal{T}_{ij}^{SGS}$. Analogously, a SGS kinetic energy k_{SGS} can be defined as

$$\mathrm{k}_{SGS} = \frac{1}{2}\widetilde{u'_i u'_i}, \tag{3.55}$$

allowing to decompose the SGS stress tensor between an isotropic and anisotropic component. The anisotropic component of the SGS stress tensor is

$$\mathcal{T}_{ij} = \mathcal{T}_{ij}^{SGS} - \frac{2}{3}\mathrm{k}_{SGS}\delta_{ij} = -2\nu_t \widetilde{S}_{ij}, \tag{3.56}$$

with $\widetilde{S}_{ij}$ being the filtered rate of strain

$$\widetilde{S}_{ij} = \frac{1}{2}\left(\frac{\partial \widetilde{u}_i}{\partial x_j} + \frac{\partial \widetilde{u}_j}{\partial x_i}\right). \tag{3.57}$$

The isotropic SGS stress is included in the modified pressure

$$\widetilde{p} = \widetilde{p} + \frac{2}{3}\rho \mathrm{k}_{SGS}. \tag{3.58}$$

Under all these circumstances, Eq. 3.54 becomes

$$\frac{\partial \widetilde{u}_i}{\partial t} + \frac{\partial\left(\widetilde{u}_i \widetilde{u}_j\right)}{\partial x_j} = -\frac{1}{\rho}\frac{\partial \widetilde{p}}{\partial x_i} + \frac{\partial}{\partial x_j}\left[\nu_{eff}\left(\frac{\partial \widetilde{u}_i}{\partial x_j} + \frac{\partial \widetilde{u}_j}{\partial x_i}\right)\right], \tag{3.59}$$

with

$$\nu_{eff} = \nu + \nu_t. \tag{3.60}$$

The same approach is taken for the energy equation. The filter operation is performed, obtaining

$$\frac{\partial \widetilde{T}}{\partial t} + \frac{\partial\left(\widetilde{u_j T}\right)}{\partial x_j} = \frac{\partial}{\partial x_j}\left(\frac{k}{\rho c_p}\frac{\partial \widetilde{T}}{\partial x_j}\right), \tag{3.61}$$

where the quantity $\widetilde{u_j T}$ is decomposed as $\widetilde{u_j T} = \widetilde{u}_j \widetilde{T} + \widetilde{u_j' T'}$. The quantity $\widetilde{u_j' T'}$ is called the SGS scalar flux $\mathcal{Q}_i$ and can be modeled by means of the gradient-diffusion approach [96]

$$\mathcal{Q}_i = \frac{\nu_t}{Pr_t}\frac{\partial \widetilde{T}}{\partial x_j}, \tag{3.62}$$

where Pr_t is the turbulent Prandtl number. Therefore, Eq. 3.61 becomes

$$\frac{\partial \widetilde{T}}{\partial t} + \frac{\partial\left(\widetilde{u}_j \widetilde{T}\right)}{\partial x_j} = \frac{\partial}{\partial x_j}\left(\Gamma_{eff}\frac{\partial \widetilde{T}}{\partial x_j}\right), \tag{3.63}$$

where

$$\Gamma_{eff} = \frac{k}{\rho c_p} + \frac{\nu_t}{Pr_t}. \tag{3.64}$$

3.2.2 The Smagorinsky model

The simplest eddy viscosity model was proposed by Smagorinsky in 1963. The Smagorinsky model states that the eddy viscosity is proportional to the characteristic length scale (the cell volume Δ and the characteristic turbulent velocity taken as the strain rate $\widetilde{S}_{ij}$ as

$$\nu_t = (C_s\Delta)^2\sqrt{2\widetilde{S}_{ij}\widetilde{S}_{ij}}, \tag{3.65}$$

where C_s is a constant of proportionality between the Smagorinsky length scale and the grid scale. According to [97], $C_s \approx 0.18$.

3.2.3 The wall-adapting local eddy viscosity model (WALE)

Of the many eddy viscosity models that exist for LES, it is worth highlighting the wall-adapting local eddy viscosity model (WALE) for its desirable properties and simplicity. This model was proposed by Nicoud and Ducros [98] and attempts to address two major drawbacks present on the Smagorinsky model:

- The classical Smagorinsky formulation does not account for energy dissipation in regions where vorticity dominates over irrotational strain.
- The Smagorinsky model gives a non-zero value of ν_t as soon as there is a velocity gradient. Near a wall, however, v_t should be zero

In LES, it is important that the value of ν_t remains the same when the reference frame is changed. Therefore, the magnitude selected to base the computation of ν_t should be invariant of the reference frame. The problems arisen by the selection of the invariant of the Smagorinsky model can be solved by selecting another invariant, in this case square of the velocity gradient tensor. Then, the following properties are obtained:

- All the turbulent structures relevant for the kinetic energy dissipation are detected by the model.
- The eddy-viscosity goes naturally to zero in the vicinity of the wall.
- Produces zero eddy-viscosity in case of pure shear.

In the WALE model, the eddy-viscosity is computed as

$$\nu_t = (C_w \Delta)^2 \frac{(\mathcal{V}_{ij}\mathcal{V}_{ij})^{3/2}}{\left(\widetilde{S}_{ij}\widetilde{S}_{ij}\right)^{5/2} + (\mathcal{V}_{ij}\mathcal{V}_{ij})^{5/4}}, \tag{3.66}$$

with

$$\mathcal{V}_{ij} = \frac{1}{2}\left(\widetilde{g}_{ij}^2 + \widetilde{g}_{ji}^2\right) - \frac{1}{3}\delta_{ij}\widetilde{g}_{kk}^2 \tag{3.67}$$

where Δ denotes the cell volume, $C_w = 0.5$ the model constant and δ_{ij} the Kronecker delta. The symbol $\widetilde{g}$ corresponds to the velocity gradient tensor

$$\widetilde{g} = \frac{\partial \widetilde{u}_i}{\partial x_j} \tag{3.68}$$

and $\widetilde{g}_{ij}^2 = \widetilde{g}_{ik}\widetilde{g}_{kj}$.

3.3 Modeling of the Navier-Stokes equations using Direct Numerical Simulation (DNS)

It is well known that the Navier-Stokes equations describe the physics of turbulent flows without the need of any of the previously discussed models. Therefore, Eqs. 2.3 to 2.5 could be directly integrated to obtain the relevant scales of the turbulent flow. However, the cost of solving the time-scales is proportional to $Re^{1/2}$ and the cost of solving accurately all the three-dimensional length scales proportional to $Re^{9/4}$. Hence, the computational cost of solving a DNS is, at least, proportional to $Re^{11/4}$, which makes DNS highly unfeasible and practically restricted to low Reynolds numbers.

On the other hand, when DNS is feasible, it allows to resolve all the relevant scales of a turbulent flow, providing spatially resolved turbulence statistics and second order statistics such as Reynolds stress tensor, turbulent kinetic energy, both their generation and dissipation. All these data is valuable not only for its end use (understanding and predicting a given flow configuration) but also to check the validity of the different turbulence models (either LES or RANS).

3.3.1 Flow statistics

As aforementioned, the flow statistics are useful to check the validity of the results obtained and to compare with different turbulence models. They are obtained by applying the Reynolds decomposition (Eq. 3.1) and operating to obtain the Reynolds stress tensor $R_{ij} = \overline{u_i' u_j'}$ using DNS data. Then the turbulent kinetic energy can be recovered as

$$\mathrm{k} = \frac{1}{2}\left(R_{11} + R_{22} + R_{33}\right). \tag{3.69}$$

Regarding the dissipation, it has been found that corresponds exactly to $\varepsilon = 2\nu\overline{S_{ij}' S_{ij}'}$ and can generally be estimated as [99]

$$\varepsilon \approx 2\nu S_{ij}'^{RMS} S_{ij}'^{RMS}, \tag{3.70}$$

where $S_{ij}'^{RMS}$ is computed as

$$S_{ij}'^{RMS} = \frac{1}{2}\left(\frac{\partial u_i'^{RMS}}{\partial x_j} + \frac{\partial u_j'^{RMS}}{\partial x_i}\right), \tag{3.71}$$

and $u_i'^{RMS} = \sqrt{R_{ii}}$ is the RMS value of the diagonal components of the Reynolds stress tensor. Using these quantities, the Kolmogorov length scale can be approximated as

$$\eta = \left(\frac{\nu^3}{\varepsilon}\right)^{\frac{1}{4}}. \tag{3.72}$$

The computations of these magnitudes on LES is similar and uses $\nu_{eff} = \nu + \nu_t$ instead of ν.

3.4 Energy preserving in the Navier-Stokes equations

One of the problems regarding the numerical integration of the Navier-Stokes equations is that the numerical dissipation of kinetic energy interferes with the energy cascade. This effect can be significant and, depending on the numerical schemes used, a coarse mesh can act as an implicit filter. In order to solve this problem, Verstappen and Veldman [100] and later Trias et al. [101] developed a formulation that allows for the conservation of kinetic energy. This formulation is based on preserving the properties of the differential operators through the discretization, in particular the convective and diffusive operator, which have to read as

$$\left(u_j \frac{\partial}{\partial x_j}\right)^* = -\left(u_j \frac{\partial}{\partial x_j}\right), \tag{3.73}$$

$$\left(\frac{\partial}{\partial x_j}\right)^* = -\left(\frac{\partial}{\partial x_j}\right). \tag{3.74}$$

Under these circumstances, the rate of change of total energy strictly becomes

$$u_j \frac{\partial u_i}{\partial x_j} = -2\nu \frac{\partial u_i}{\partial x_j} \frac{\partial u_i}{\partial x_j} \leq 0 \tag{3.75}$$

Therefore, under such a formulation, the Navier-Stokes equations are stable on any grid leaving the grid density a parameter based on the required accuracy.

This formulation has been extended to F.E. by Lehmkuhl et al. [102]. On this topic, another methodology called EMAC, that conserves not only energy but also momentum and angular momentum was proposed by Charnyi et al. [103]. The EMAC formulation along with an explicit fourth-order Runge-Kutta integrator [104] combined with an eigenvalue based time-step estimator [105] have been implemented into Alya. Therefore, the formulation in Alya allows for the resolution of complex geometries obtaining a very accurate description of the turbulent parameters, even under LES [106].

II

Results and Discussion

4

Domain Analysis and Grid Sensitivity Studies

In computational analyses, it is essential to ensure that the computational grids produce the correct results and contain all the needed scales of motion to represent the flow. This is usually done by performing successive simulations while refining the grid and further analyzing the convergence towards the solution. Moreover, when possible, two point correlations enable to verify that the largest scales of the flow are contained within the domain.

For this reason, this chapter is devoted to the explanation of the computational grids used in this work and to show the domain analysis and grid sensitivity studies performed in order to verify the correctness of the solution achieved with the aforementioned grids. The chapter starts by outlining the computational domain (already presented in Section 2.1) as well as highlighting the cases considered to perform the mesh sensitivity analysis as well as the boundary conditions used. Next, some data reduction operators are presented as they are used for the grid sensitivity study (as well as to present the results in the upcoming chapters). Then, the computational grids and their construction methods are presented along with a grid sensitivity study and two-point correlations. Finally, the temporal convergence of the impinging synthetic jet is analyzed and a method of reduction of computational time is presented.

4.1 Computational domain and boundary conditions

The geometry of the computational domain and its dimensions are presented in Section 2.1. A schematic view of the computational domain is reproduced again in this section (see Fig. 4.1), for a better understanding of the reader.

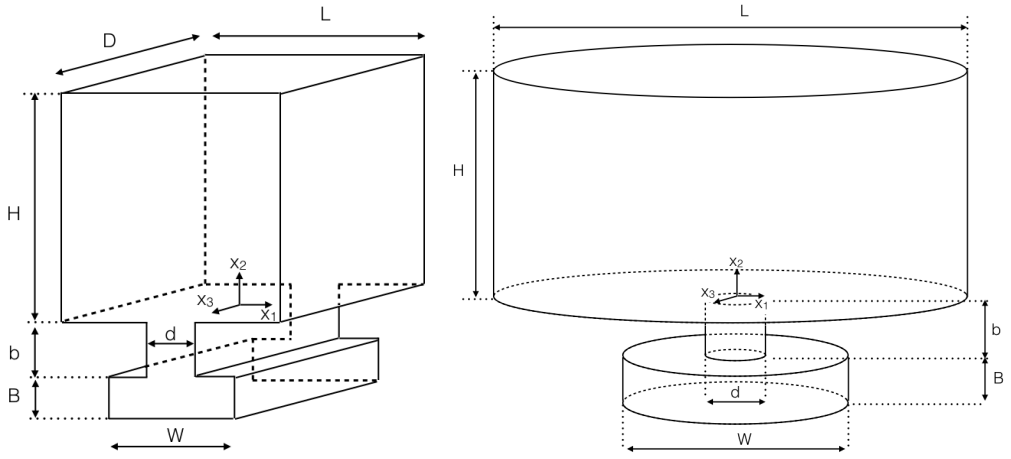

(a) Slotted. (b) Axisymmetric.

Figure 4.1: Geometry of the analyzed configurations (not to scale).

The Reynolds numbers considered on this work are $Re = 50$, 100, 300, 500 and $1,000$ for the slotted configuration and $Re = 50$ and 500 for the circular configuration. DNS are performed for $Re = 50$ and 100, whereas, LES are carried out when $Re > 100$. The WALE SGS model, as described in Section 3.2.3, is used as it is formulated in a way that it is suitable for unstructured grids and has the property of not acting near the walls or in two-dimensional flows. Moreover, its dissipation is relatively small in transitional flows. The SGS scalar flux is modeled using a gradient diffusion approach as described in the last paragraphs of Section 3.2. Two large-scale parallel computational fluid dynamics codes have been used to compute the solution field for the fluid and its thermal interaction with the heated wall. They are described in Chapter 3. Precursory laminar and RANS flow fields are computed using *Code_Saturne*, while DNS and LES are computed using Alya. Moreover, some work with *Code_Saturne* and LES is also performed in [19].

In order to simplify the notation, when discussing the results the symbol $\widetilde{\cdot}$ shall be dropped when $Re > 100$. Moreover, the results are expressed in dimensionless form where $\widehat{x}_i = x_i/d$ is the dimensionless spatial coordinates, $\widehat{u}_i = u_i/U_0$ the dimensionless velocity components and $\widehat{T} = (T - T_\infty)/(T_{wall} - T_\infty)$ the dimensionless temperature and T_{wall} denotes the temperature at the heated wall and T_∞ the bulk temperature.

No-slip boundary conditions are imposed at the top ($\widehat{x}_2 = H/d$) and bottom ($\widehat{x}_2 = 0$) of the discharge cavity as well as at the actuator walls including the SJA membrane ($\widehat{x}_2 < 0$). Free-flow

boundary conditions are prescribed at all the vertical boundaries with $\widehat{x}_2 > 0$. Regarding the energy equation, the cavity top wall is hot ($\widehat{T} = 1$) and the bottom wall is cold ($\widehat{T} = 0$). The lateral boundaries are considered adiabatic ($\partial\widehat{T}/\partial n = 0$). The SJA walls ($\widehat{x}_2 < 0$) are assumed to be cold. Periodic boundary conditions are set between the front ($\widehat{x}_3 = 0$) and back ($\widehat{x}_3 = D/d$) faces. The SJA membrane movement has been modeled using a M1 model, as described in Section 2.3.

4.2 Data reduction

Due to the complexity of the flow, it is necessary to perform various averaging operations in space and time (or both). These operators are often used in this work and are based in the work of Kotapati et al. [15]. Assuming a generic variable ϕ, they are:

- Time average

$$\overline{\phi} = \frac{1}{\Delta t}\int_{t_0}^{t_0+\Delta t} \phi \, dt. \tag{4.1}$$

- Phase average over M cycles

$$\langle\phi\rangle = \frac{1}{MT}\int_{t_0}^{t_0+MT} \phi \, dt. \tag{4.2}$$

- Span-wise average (only defined for the slotted case)

$$\phi = \frac{1}{L_3}\int_{-L_3/2}^{L_3/2} \phi \, dx_3. \tag{4.3}$$

- Symmetry average defined as

$$\phi = \frac{\phi(-x_1, t) + \phi(x_1, t)}{2}, \tag{4.4}$$

  and for the circular case

$$\phi = \frac{\phi(-r, t) + \phi(r, t)}{2}. \tag{4.5}$$

Symmetry averaging is possible for both configurations since, at the stationary flow field, this must be symmetrical (as the whole case is symmetrical, there should not be preference for any direction). Moreover, the meshes used are symmetrical and a correctly performed symmetry average helps reducing the necessary time to reach a converged stationary flow field.

4.3 Computational grid analysis

Two similar strategies have been used to design the computational grids:

- The slotted configuration grid is built by extruding a two-dimensional grid along the x_3 axis for a certain number of planes and a fixed depth of $\widehat{x}_3 = 6$.
- The axisymmetric configuration grid is created by the revolution of a two-dimensional grid along the x_2 axis for a certain number of angular divisions.

A detail of the computational grids for both configurations is presented in Fig. 4.2. Successive grids have been constructed by multiplying the two-dimensional generator grid. The coarsest grid considered (for $Re = 50$) has $350,000$ control volumes (CV); whereas the finer grids considered (for $Re = 500$) have 4.0 and 5.0 million CV.

Extensive grid convergence studies have been carried out for each Reynolds numbers and configurations considered. As an example, Fig. 4.3 shows the grid study for both configurations at $Re = 500$. The span-wise and time averaged stream-wise velocity profiles at different heights are compared in Fig. 4.3a showing good agreement between them with minimal differences at the points of maximum and minimum span-wise velocity. A good agreement is also achieved between the centerline time averaged temperatures presented in Fig. 4.3b. Finally, Fig. 4.3c presents the Nusselt number at the hot wall for the grids considered. Good agreement is observed between the mid-size and fine grids compared with the coarse grid. In this sense, the mid-size grid presents a good compromise between accurate results and computational time.

As discussed in Chapter 3, the present code automatically selects the time-step using an eigenvalue-based time-step estimator. As an example, for $Re = 500$ and $Re = 1000$ in the slotted configuration, the number of time-steps per actuator cycle is about $13,400$ and $25,200$ respectively. Whereas, in the circular configuration for $Re = 500$ the number of time-steps per actuator cycle is about $20,480$.

The computational domain in the span-wise (and radial) direction has been designed to contain the largest scales of the flow. In the slotted configuration, span-wise two point correlations are used to verify whether the assumed size is correct for all Reynolds numbers considered. They are defined as

$$\mathcal{R}_{ii} = \frac{\overline{u_i'(x_i,t)u_i'(x_i+\delta,t)}}{\overline{u_i'u_i'}}, \tag{4.6}$$

where $u_i' = u_i - \overline{u}_i$. The values for the two point correlation must tend to zero for the turbulent cases as they approach the half-size of the domain. Fig. 4.4 presents the span-wise two point correlations

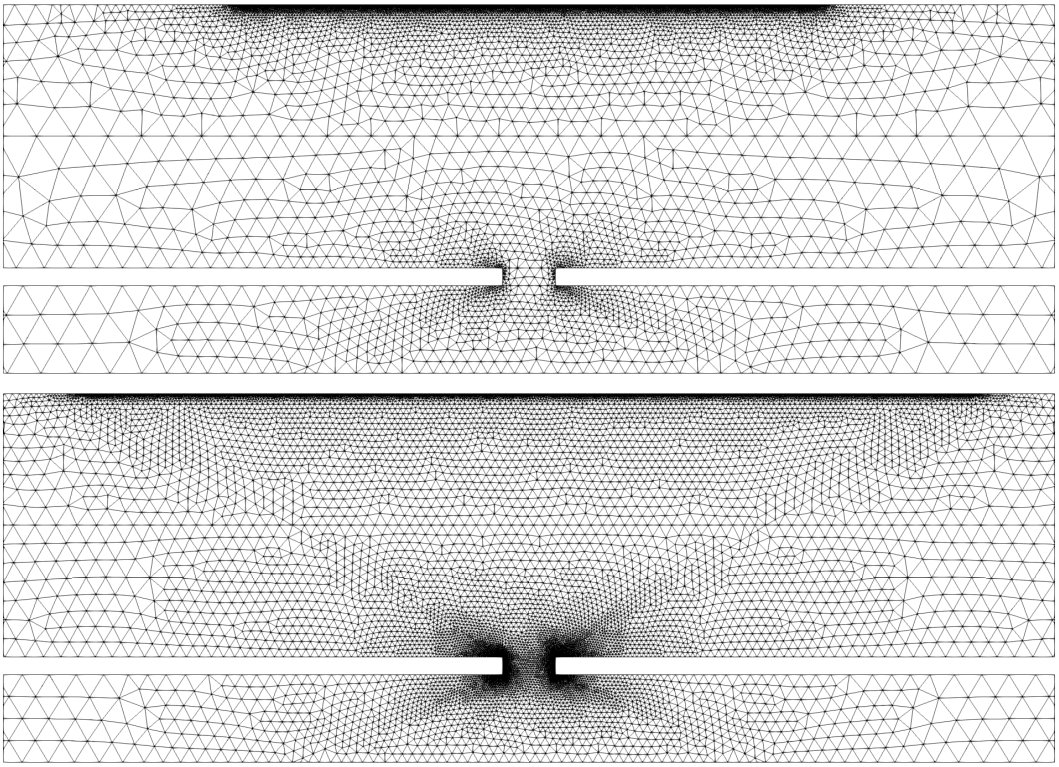

(a) Slotted configuration, only shown from $\widehat{x}_1 = -10$ to $\widehat{x}_1 = 10$ and one plane for clarity. Top: $800,000$ CV. Bottom: 1.44 million CV.

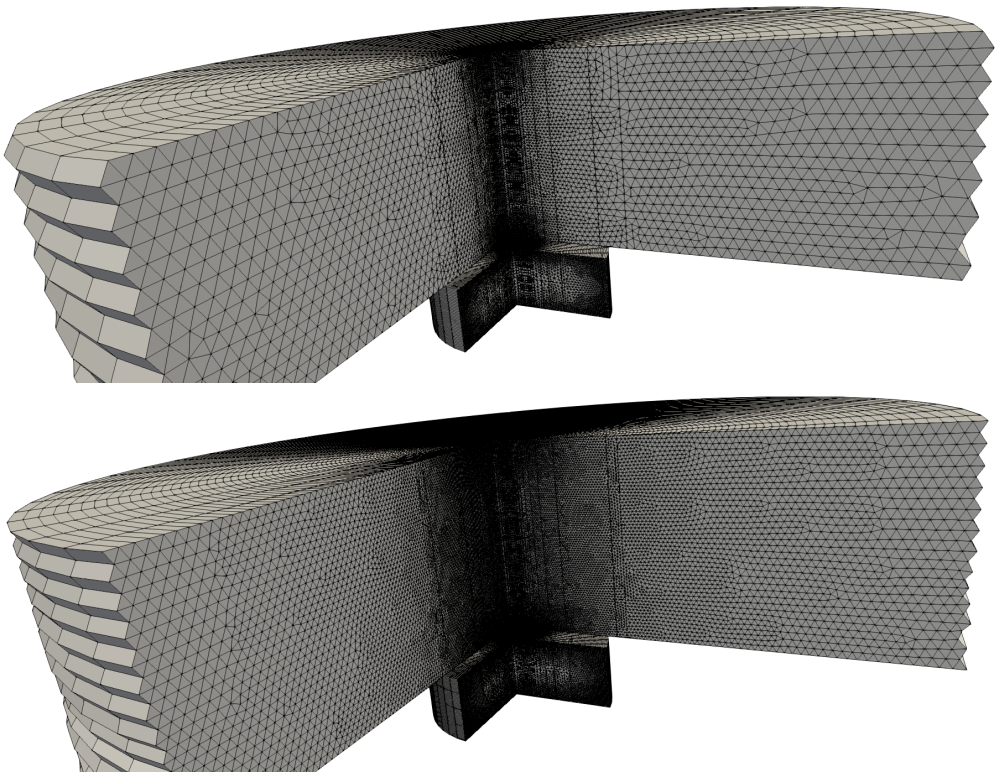

(b) Circular configuration, only shown from $\widehat{r} < 10$. Top: $750,000$ CV. Bottom: 1.8 million CV.

Figure 4.2: Computational grid examples for both configurations.

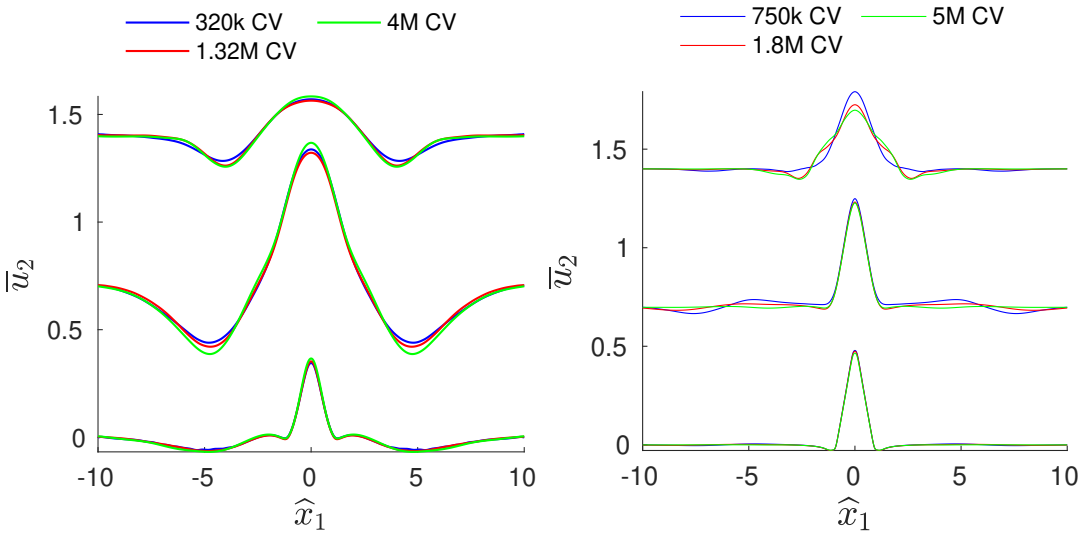

(a) Time (and span-wise, in the slotted configuration) averaged stream-wise velocity at different heights ($\widehat{x}_2 = 0.5$, $\widehat{x}_2 = 2.5$ and $\widehat{x}_2 = 4.5$, each shifted 0.7 units upwards).

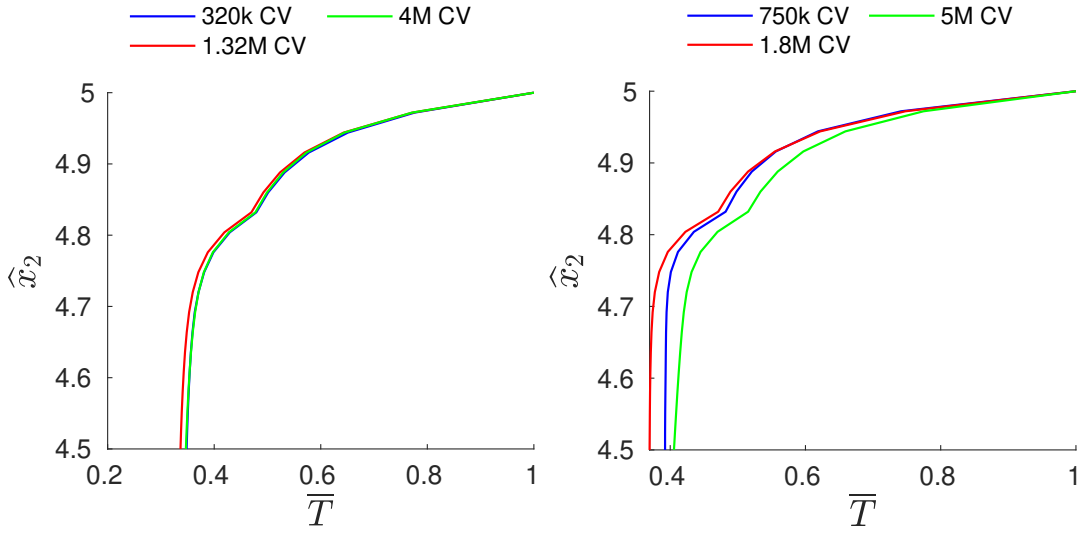

(b) Time (and span-wise, in the slotted configuration) averaged temperature at the jet centerline ($\widehat{x}_1 = 0.0$).

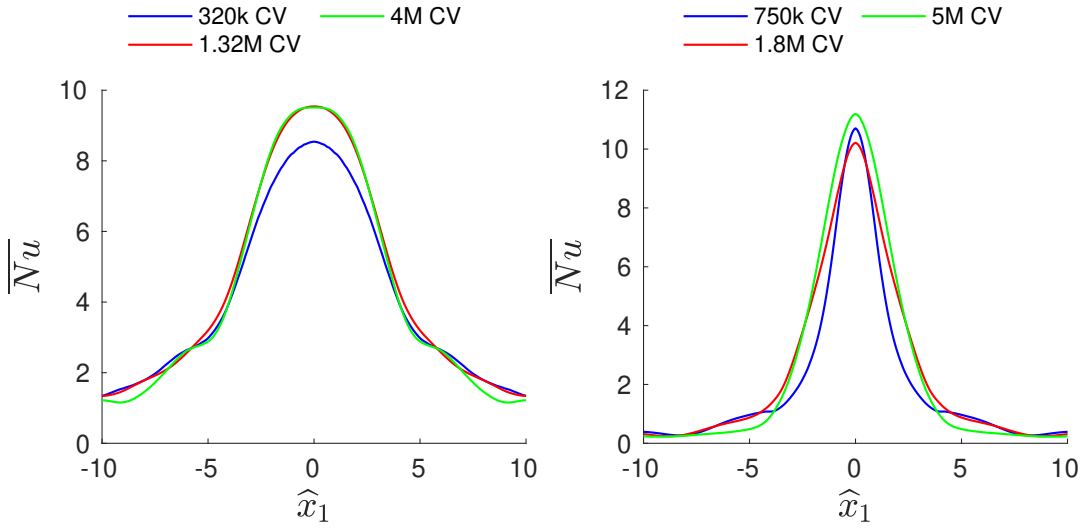

(c) Time (and span-wise, in the slotted configuration) averaged Nusselt number at the hot wall ($\widehat{x}_2 = 5.0$).

Figure 4.3: Grid convergence study at $Re = 500$ for the slotted (left) and circular (right) configurations.

for $u_3'u_3'$ at $\widehat{x}_1 = 0$ and $\widehat{x}_2 = 2.5$ for the slotted configuration and all the Reynolds considered in this study. This position has been selected as a representative point where the jet scales have been fully developed. As seen in the figure, all correlations approach zero at the domain half size, confirming that a domain width of $D/d = 6$ is enough as to contain the largest and more energetic scales, except for $Re = 50$. This could indicate the presence of quasi-laminar structures and a larger domain would be needed. However, $D/d = 6$ has been maintained for $Re = 50$ as a good compromise of computational time.

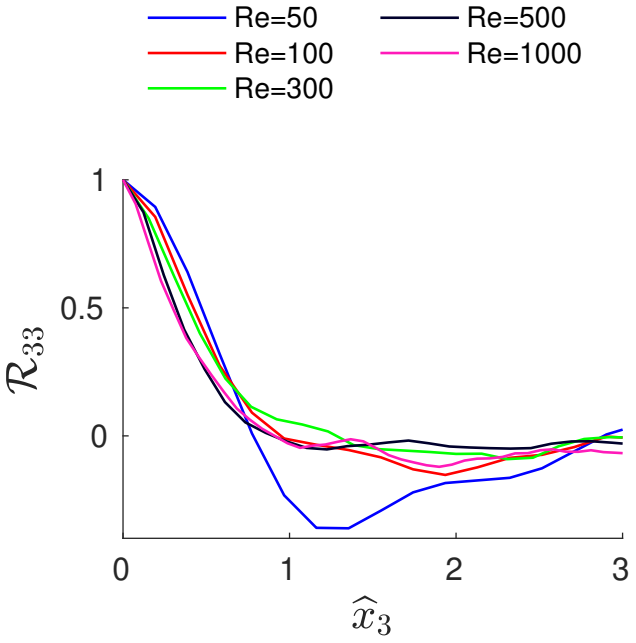

Figure 4.4: Two point correlation for $u_3'u_3'$ and different Reynolds numbers, using the finest grid, at $\widehat{x}_1 = 0$, $\widehat{x}_2 = 2.5$.

4.4 Temporal convergence study

Statistically accurate representations of the flow are needed in order to understand the SJA flow. However, in both configurations, the overall system contains very slow temporal scales related with the low velocity zones, despite the intense mixing in the jet vicinity. This results in a very large computational time for the flow to reach statistical stationary conditions.

For this reason, precursory two-dimensional laminar (for $Re = 50, 100$) and URANS (for $Re > 100$) simulations using the k $- \omega$ SST model [95] with a reasonably large time-step have been analyzed to estimate the time scales associated with the process.

This is illustrated in Fig. 4.5a that shows the temporal evolution of the dimensionless temperature at maximum expulsion ($t = 0$) and maximum ingestion ($t = \tau/2$) for one precursory simulation at

$Re = 500$ and both configurations. It is revealed that about 100 actuator cycles are needed to reach stationary conditions. Therefore, the flow has been initialized using these precursory simulations in order to reduce the computational time. Using this strategy, the computational time required to reach the statistical stationary is drastically reduced. Fig. 4.5b shows 50 cycles of LES starting from URANS solution. As it can be seen in this 50 cycles, if the flow is given enough time to adapt, the statistical stationary is already achieved.

Moreover, the initial conditions for the finer meshes are generated from the solution obtained with coarser grids, which in turn reduced the initial transient by 20 cycles. Once the statistical stationary state is reached, the simulations are run for 30 actuator cycles, using the last 20 to obtain relevant time and phase averages of the flow and the Nusselt number.

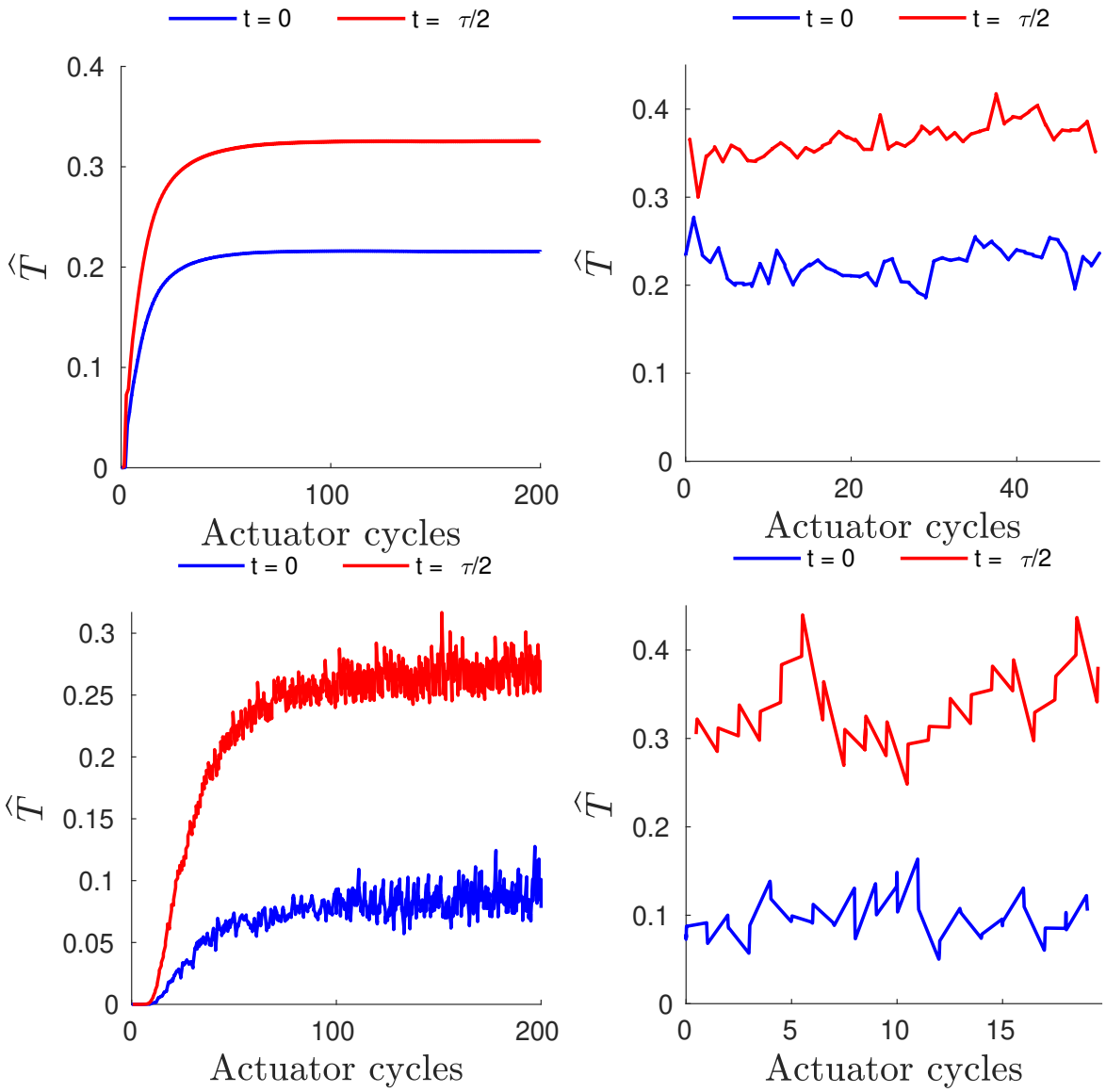

(a) URANS k $-\omega$ SST and a large time-step.

(b) LES starting from URANS solution.

Figure 4.5: Time evolution (in actuator cycles) of the temperature at the SJA orifice at $Re = 500$ for maximum expulsion ($t = 0$) and maximum ingestion ($t = \tau/2$) parts of the cycle. The top figures correspond to the slotted configuration, while the bottom correspond to the circular one.

5

Dynamics of Synthetic Jet Flow

As aforementioned, the phenomenology and flow of a synthetic jet actuator are very complex and interesting. Numerical simulations can provide a good insight on the flow of a SJA, which not only depends on the governing parameters but also the geometric configuration. In this line, the following chapter presents the results of the numerical analysis of the SJA flow at several Reynolds numbers and two configurations: a slotted and a circular configuration. The discussion starts with a description of the instantaneous flow of both configurations in which the vortical structures and the time-dependent signals are analyzed. The cases at $Re = 50$ and $Re = 500$ are taken as representatives of the flow. The time analysis of the signals yields one of the reasons why numerical simulations of SJA are computationally expensive. Next, an accurate description of the vortical structures using time and phase averaged flows follows. The main vortices are then identified and the flow dynamics are explained. Finally, a comparison between the flow from the slotted and circular configuration is made and the fundamental differences between both configurations are stressed.

5.1 Instantaneous flow

The flow on a synthetic jet is very complex and its morphology is highly influenced by the JFC and its geometry. Vortices roll up from the actuator lips and move upwards, until the impingement into the top wall is reached, where there is a heat exchange between the fluid and the hot wall.

Vortical structures have been identified using Q-isocontours [107] where Q is the second invariant of the velocity gradient tensor and is defined as

$$Q = -\frac{1}{2}\frac{\partial u_i}{\partial x_j}\frac{\partial u_j}{\partial x_i} \tag{5.1}$$

The condition $Q > 0$ has been found to be effective in identifying regions of coherent vorticity [16, 42]. As expected, these regions become more apparent and smaller with the Reynolds number.

5.1.1 Slotted configuration

Typical instantaneous vortical structures of the SJA flow for the slotted configuration at all the Reynolds numbers considered are shown in Figs. 5.1, 5.2, 5.3 and 5.4. Four different instants (or phases) can be appreciated:

- Fig. 5.1 is the maximum expulsion phase ($t = 0$).
- Fig. 5.2 is the maximum ingestion phase ($t = \tau/2$).
- Fig. 5.3 is the maximum positive membrane displacement phase ($t = \tau/4$).
- Fig. 5.4 is the maximum negative membrane displacement phase ($t = 3\tau/4$).

The flow for the slotted configuration at $Re = 50$ is laminar and three-dimensional due to the vortex stretching. Larger coherent structures can be seen at both $Re = 50$ and $Re = 100$, although they are smaller and less noticeable at $Re = 500$. The flows at $Re = 300$, $Re = 500$ and $Re = 1,000$ present a large amount of vortical structures, mostly concentrated in the zones near the neck, both outside and inside the synthetic jet actuator cavity. As expected, these structures become smaller and appear in more quantity as Re is increased. The temporal behavior of the flow is the same regardless of the Re considered. During the ejection stroke, the vortex dipoles roll-up from the orifice and almost lose all coherence due to the interaction with the smaller structures and the vortex stretching (see Fig. 5.1). This creates a jet of cold fluid that advects downstream until the impingement is reached at about $t = \tau/4$ (see Fig. 5.2). During the suction part of the cycle, some of these heated structures are ingested back inside the actuator cavity ($t = 3\tau/4$), where they are

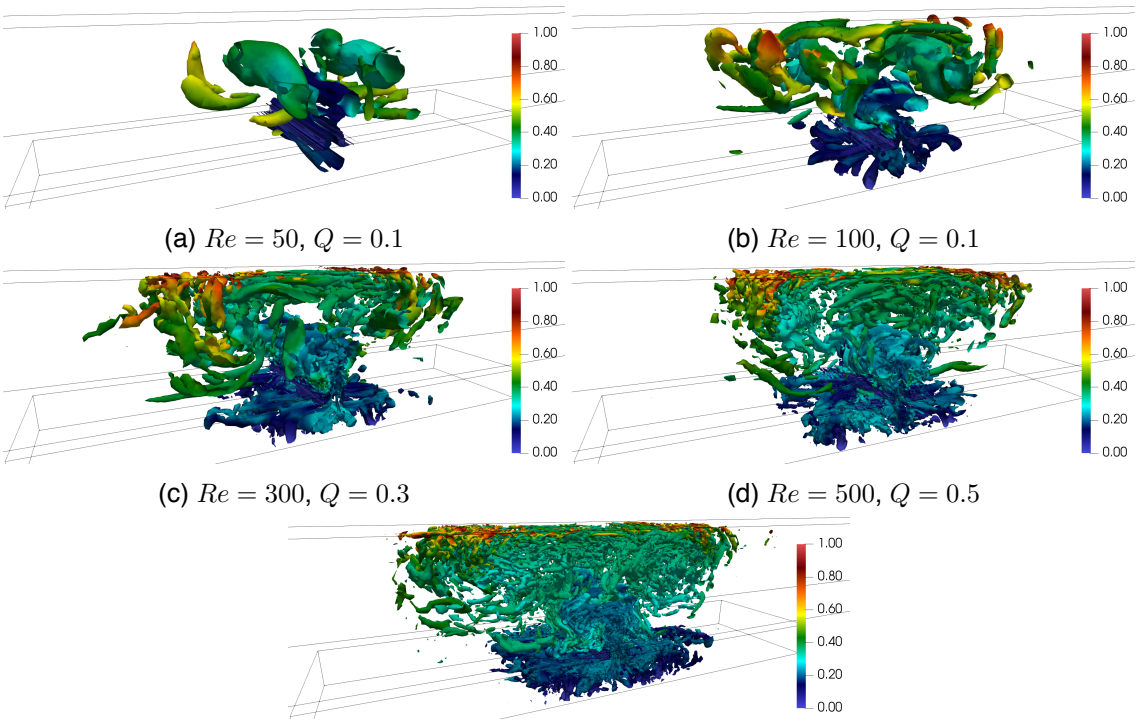

(a) $Re = 50$, $Q = 0.1$ (b) $Re = 100$, $Q = 0.1$

(c) $Re = 300$, $Q = 0.3$ (d) $Re = 500$, $Q = 0.5$

(e) $Re = 1,000$, $Q = 1.0$

Figure 5.1: Q-isocontours colored by the dimensionless temperature at phase $t = 0$ for the slotted configuration at the Reynolds numbers considered.

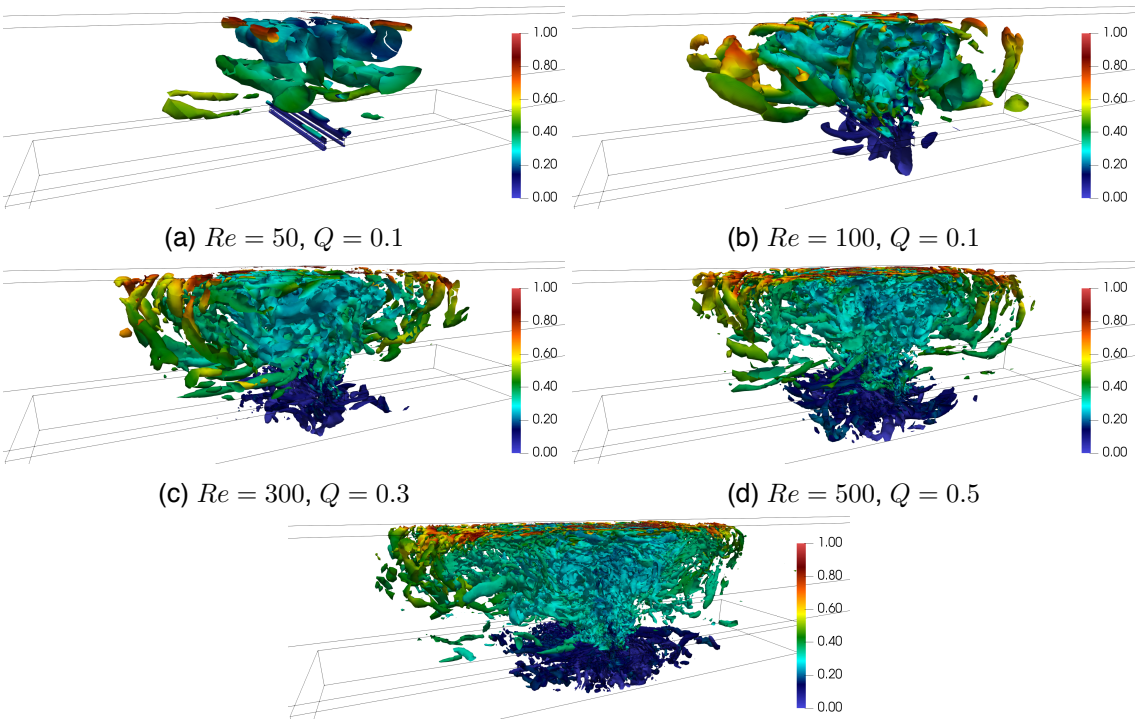

(a) $Re = 50$, $Q = 0.1$ (b) $Re = 100$, $Q = 0.1$

(c) $Re = 300$, $Q = 0.3$ (d) $Re = 500$, $Q = 0.5$

(e) $Re = 1,000$, $Q = 1.0$

Figure 5.2: Q-isocontours colored by the dimensionless temperature at phase $t = \tau/4$ for the slotted configuration at the Reynolds numbers considered.

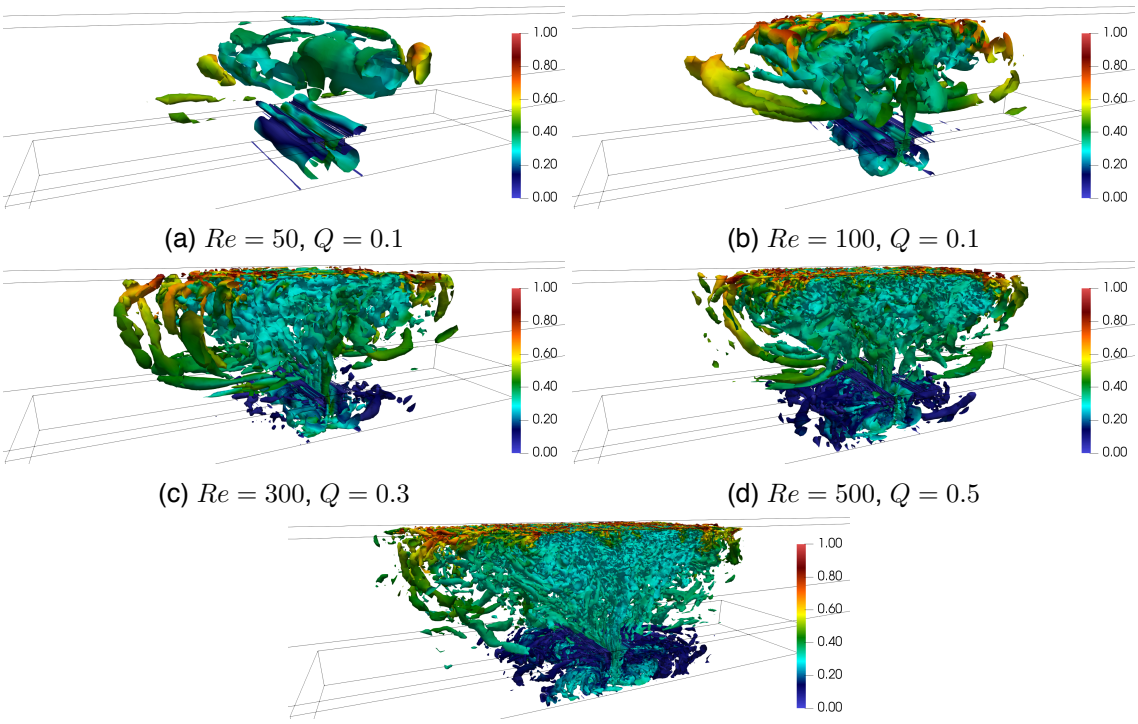

(a) $Re = 50$, $Q = 0.1$ (b) $Re = 100$, $Q = 0.1$

(c) $Re = 300$, $Q = 0.3$ (d) $Re = 500$, $Q = 0.5$

(e) $Re = 1,000$, $Q = 1.0$

Figure 5.3: Q-isocontours colored by the dimensionless temperature at phase $t = \tau/2$ for the slotted configuration at the Reynolds numbers considered.

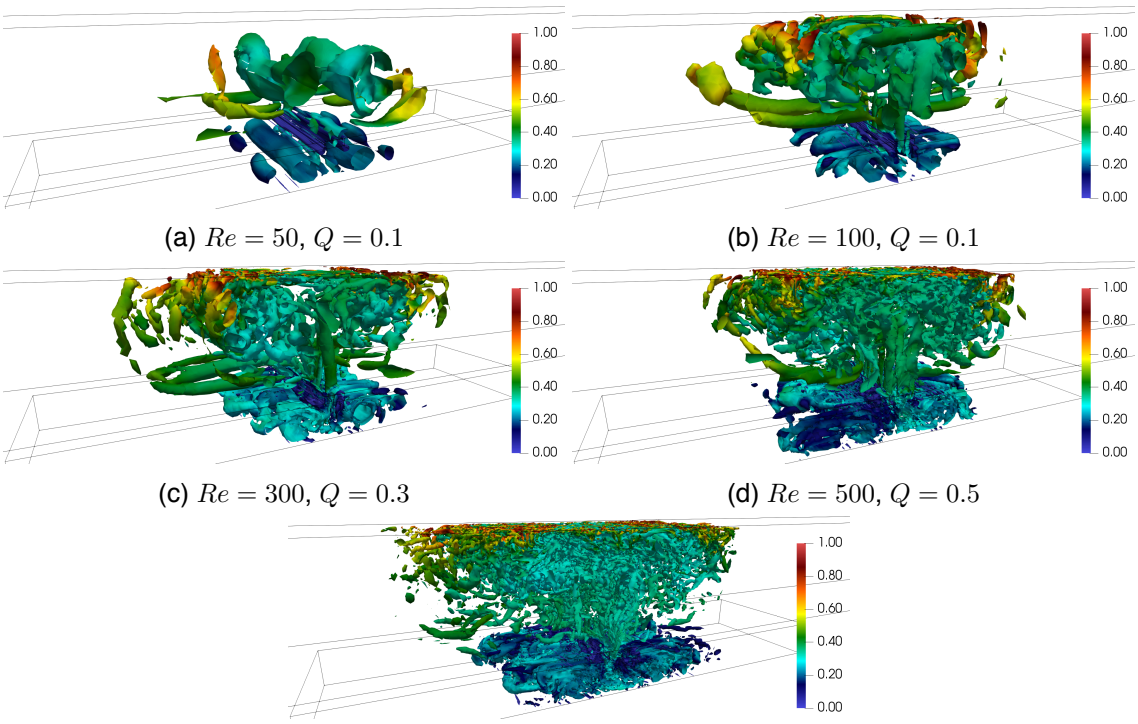

(a) $Re = 50$, $Q = 0.1$ (b) $Re = 100$, $Q = 0.1$

(c) $Re = 300$, $Q = 0.3$ (d) $Re = 500$, $Q = 0.5$

(e) $Re = 1,000$, $Q = 1.0$

Figure 5.4: Q-isocontours colored by the dimensionless temperature at phase $t = 3\tau/4$ for the slotted configuration at the Reynolds numbers considered.

cooled before being ejected again (see Fig. 5.3). Moreover, there is no noticeable potential core as it is seen in the axisymmetric configuration. This jet morphology and behavior are also consistent with what is observed for two- and three-dimensional slotted synthetic jets [15, 16].

5.1.2 Circular configuration

In a similar manner as presented for the slotted configuration, Figs. 5.5, 5.6, 5.7 and 5.8 show typical instantaneous vortical structures of the circular SJA flow at $Re = 50$ and $Re = 500$ along with illustrative flows at $Re = 100$ and $Re = 300$. The same aforementioned instants can be appreciated:

- Fig. 5.5 is the maximum expulsion phase ($t = 0$).
- Fig. 5.6 is the maximum ingestion phase ($t = \tau/2$).
- Fig. 5.7 is the maximum positive membrane displacement phase ($t = \tau/4$).
- Fig. 5.8 is the maximum negative membrane displacement phase ($t = 3\tau/4$).

In this case, the flows at $Re = 50$ and $Re = 100$ are also laminar and almost two-dimensional. The trailing jet observed for high JFC synthetic jets is not visible as Re is too low and the Kelvin-Helmholtz instability is not triggered. The flows at $Re = 300$ and $Re = 500$ have a more interesting behavior. Again, a large amount of vortical structures can be observed in the flow, mostly concentrated in the zones near the orifice, both outside and inside the synthetic jet actuator cavity. The trailing jet at $Re = 500$ presents more vortical structures than the trailing jet at $Re = 300$. In the flow at $Re = 300$, the potential core is more visible. Also, the vortex ring presents more coherence at $Re = 300$. The flow dynamics are the same between both configurations, however, noticeable differences can be observed in the morphology of the flow. The flow of the circular configuration starts with a main vortex ring at about $\widehat{x}_2 = 2.5$ (see Fig. 5.5) being advected downstream from the actuator orifice and reaching the impingement without losing its coherence (see Fig. 5.6). Along with the main ring, there are a number of small structures formed by the Kevin-Helmholtz instability as well as a region of low turbulence in the vicinity of the orifice, the potential core (Fig. 5.6). Vortex separation (pinch-off) [46] is observable between the main vortex ring and the trailing jet, although both have reached the impingement and spread through the heated wall during the suction part of the cycle (see Fig. 5.7). The main vortex ring is persistent enough to be still visible at the start of the next expulsion part of the cycle (see Figs. 5.5 and 5.8). This jet morphology is characteristic of jets with high JFC and is consistent with what has been observed in the literature for continuous and synthetic jets [28, 46, 108].

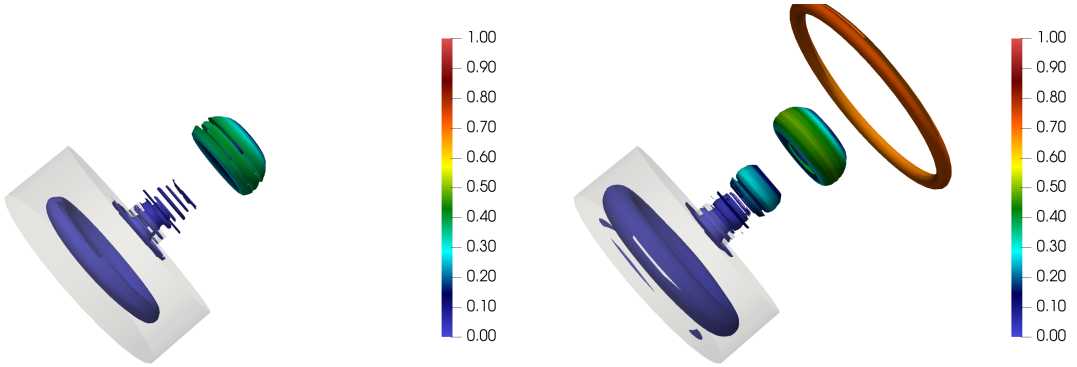

(a) $Re = 50$, $Q = 0.1$

(b) $Re = 100$, $Q = 0.1$

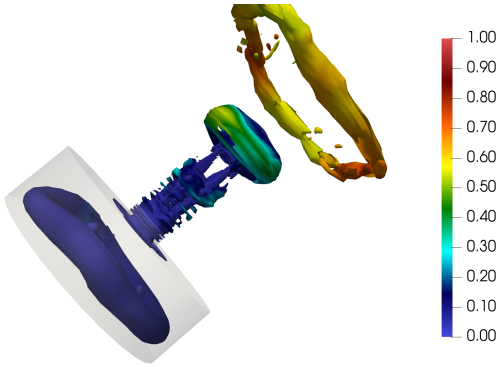

(c) $Re = 300$, $Q = 0.3$

(d) $Re = 500$, $Q = 0.5$

Figure 5.5: Q-isocontours colored by the dimensionless temperature at phase $t = 0$ for the circular configuration at the Reynolds numbers considered.

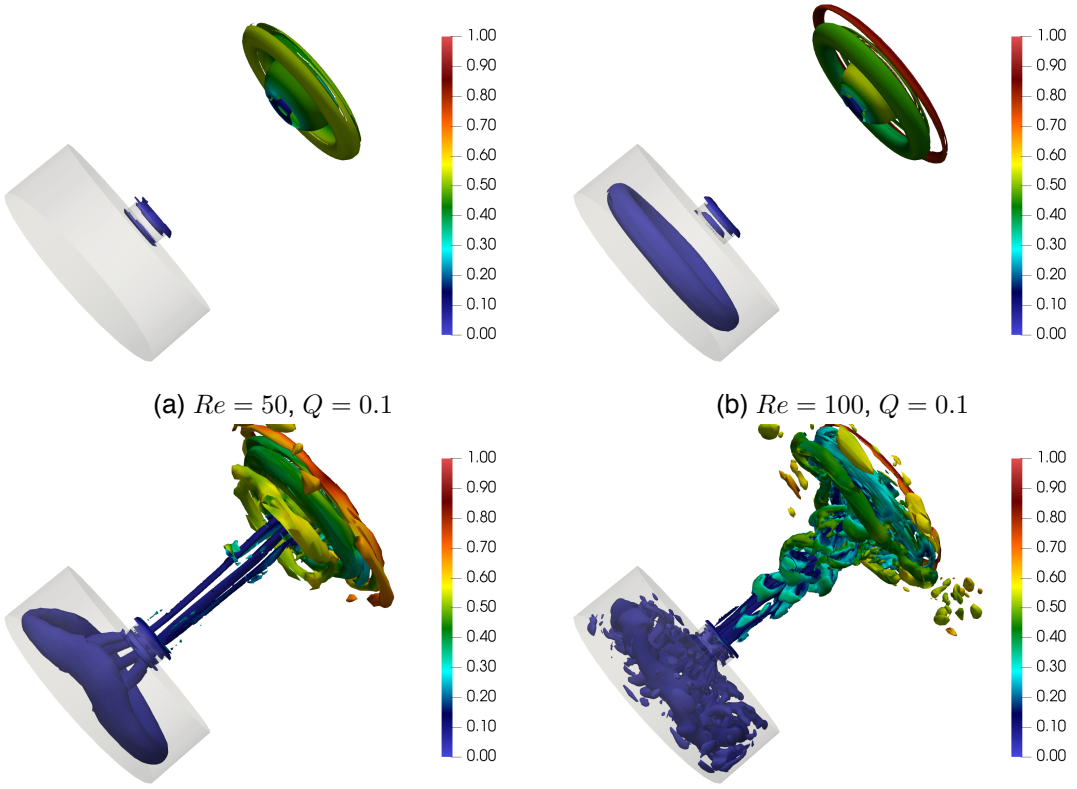

(a) $Re = 50$, $Q = 0.1$

(b) $Re = 100$, $Q = 0.1$

(c) $Re = 300$, $Q = 0.3$

(d) $Re = 500$, $Q = 0.5$

Figure 5.6: Q-isocontours colored by the dimensionless temperature at phase $t = \tau/4$ for the circular configuration at the Reynolds numbers considered.

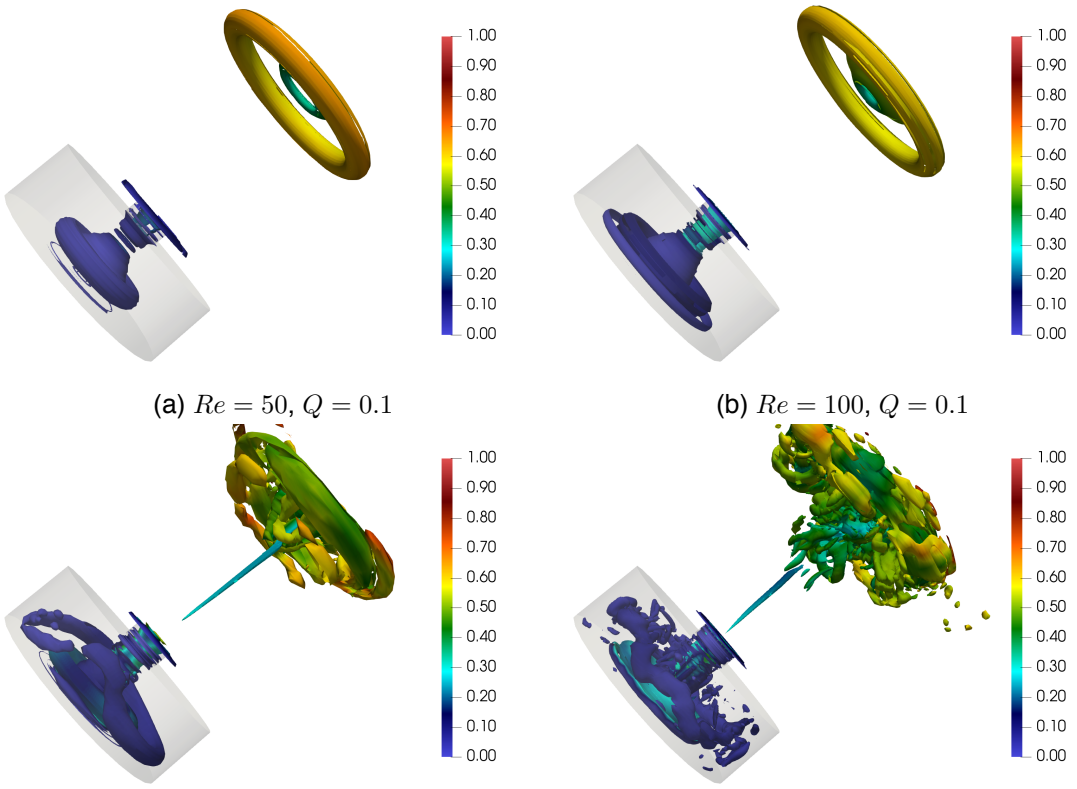

(a) $Re = 50$, $Q = 0.1$

(b) $Re = 100$, $Q = 0.1$

(c) $Re = 300$, $Q = 0.3$

(d) $Re = 500$, $Q = 0.5$

Figure 5.7: Q-isocontours colored by the dimensionless temperature at phase $t = \tau/2$ for the circular configuration at the Reynolds numbers considered.

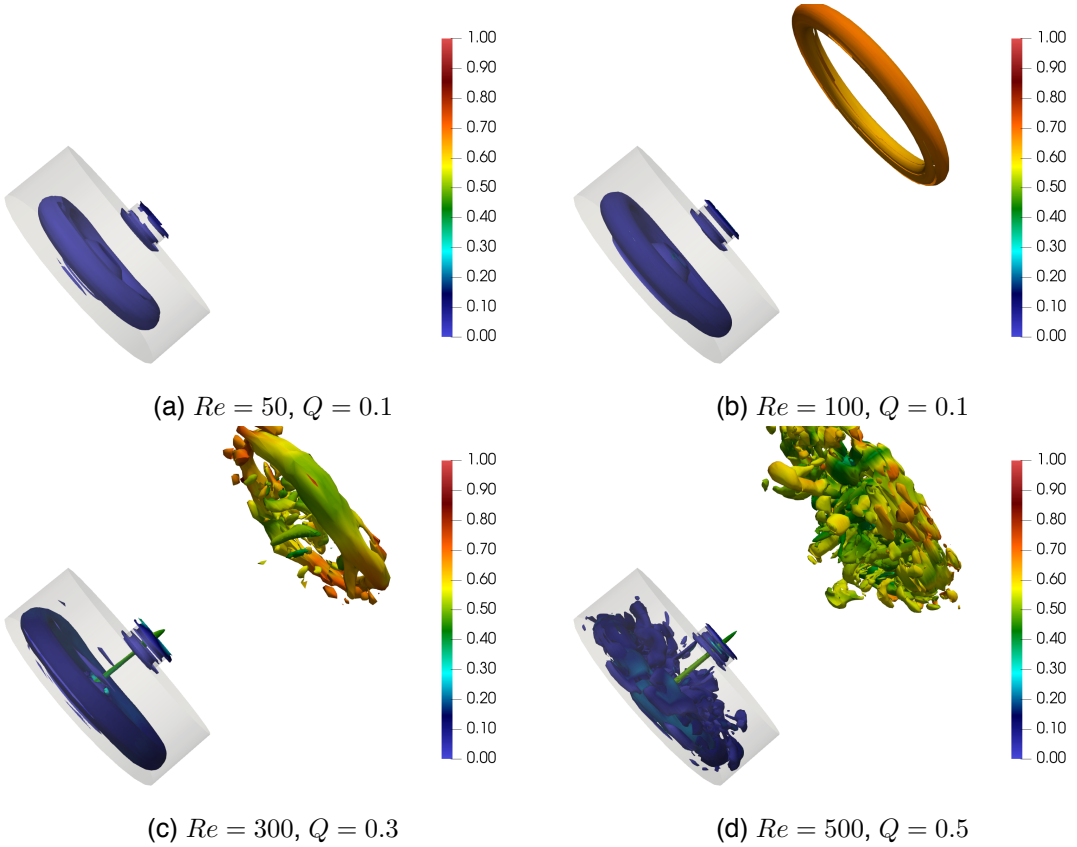

(a) $Re = 50$, $Q = 0.1$

(b) $Re = 100$, $Q = 0.1$

(c) $Re = 300$, $Q = 0.3$

(d) $Re = 500$, $Q = 0.5$

Figure 5.8: Q-isocontours colored by the dimensionless temperature at phase $t = 3\tau/4$ for the circular configuration at the Reynolds numbers considered.

5.1.3 Frequency analysis of the flow

Due to the temporal scales associated with the low velocity zones, it is interesting to identify the frequencies related to these zones as they have an impact on the averaged flow statistics. To do so, a set of numerical probes have been located at different zones of the domain and the signal of the independent variables has been recorded during the whole simulation. These numerical probes are located in the following matrix: $\widehat{x}_1 = 0,\ 5,$ and 10, $\widehat{x}_2 = 0,\ 2.5,$ and 4.5 and for each plane in the $\widehat{x}_3$ or angular direction.

The signal of different probes at $Re = 500$ located at the same vertical distance from the bottom wall $\widehat{x}_2 = 2.5$ but at different $\widehat{x}_1$ distance from the jet centerline are plotted in Fig. 5.9. The energy spectrum of these signals is plotted in Fig. 5.10. As can be seen from the figures, the signal of probe located in the centerline of the jet is dominated by the periodicity of the ejection and suction events. Notice also the amplitude in the fluctuations, which are the largest of three sets of probes. As the flow moves away from the jet centerline, the footprint of the cyclic ejection/suction event can still be observed but also a low frequency modulation in the signal.

This behavior can be better detected in the energy spectrum of these signals (see Fig. 5.10). The SJA main frequency can be seen at all numerical probes, marked in the figures as driving frequency. Yet the energy contained in this peak decreases as the signal of the flow is recorded away from the jet centerline. When comparing the energy contained in this peak for both configurations, it can be seen that it is higher for the circular configuration. Notice that, in both configurations, the spectra also contain harmonics of the main peak, at frequencies $2f/f_0$, $3f/f_0$ and further for the circular configuration, corresponding to the vortices created by the Kelvin-Helmholtz instability. The footprint of the cyclic ejection/suction event can still be observed when the flow away from the jet centerline is inspected, yet the energy contained in the peaks is decreased. The temporal signals of stream-wise velocity for the circular configuration away from the jet (Figs. 5.9a and 5.9b) present a much lower amplitude than their counterparts on the slotted configuration. This results in a lower energy contained in the peaks for the circular configuration away from the centerline (Figs. 5.10a and 5.10b). Moreover, a broadband low-frequency signal, also marked in the figures, can be seen for both configurations corresponding to the slow motion of the largest scales of the flow. This peak is centered around $f = 0.0075$ for $Re = 500$, which roughly corresponds to approximately 7 actuator cycles. These frequencies are also related with the vibration frequencies of the larger structures that have been identified in the flow, as it will be later seen. Moreover, as a result of this low-frequency motion, well-converged statistics of the flow far from the jet centerline require a longer time integration of at least a few slow-motion full cycles. In addition, these frequencies are independent of the geometry studied and are mostly influenced by the Re and Sk numbers (or JFC) selected.

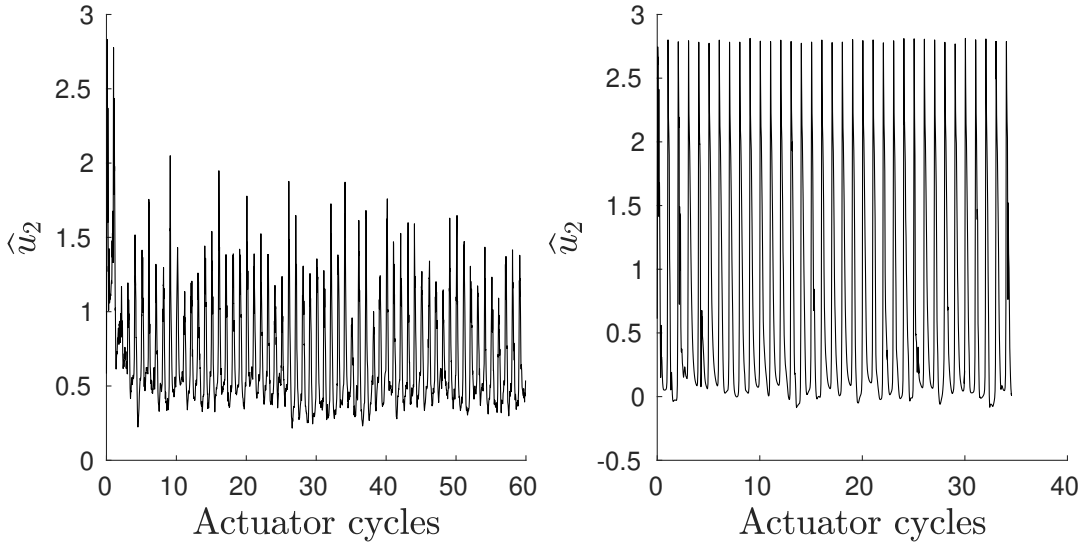

(a) Probe location: $\widehat{x}_1 = 0$, $\widehat{x}_2 = 2.5$.

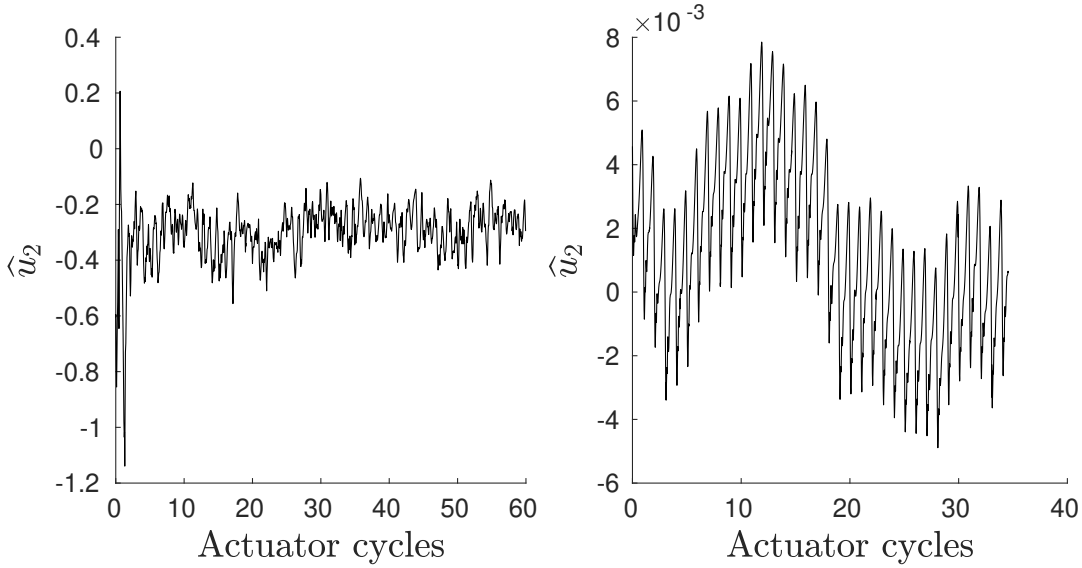

(b) Probe location: $\widehat{x}_1 = 5$, $\widehat{x}_2 = 2.5$.

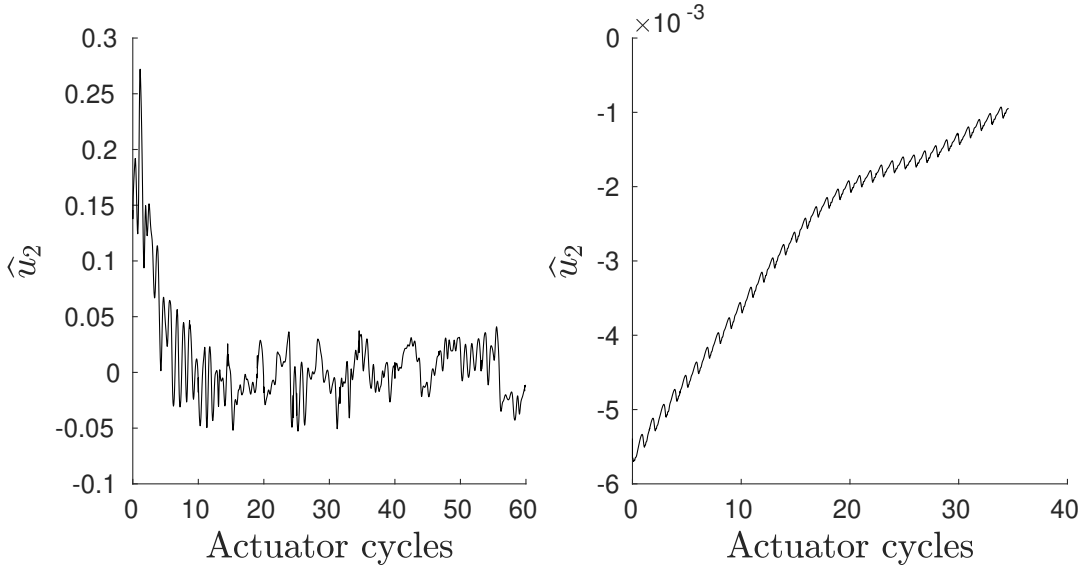

(c) Probe location: $\widehat{x}_1 = 10$, $\widehat{x}_2 = 2.5$.

Figure 5.9: Temporal evolution of the span-wise (axisymmetric) averaged stream-wise velocity for the slotted (left) and circular (right) configurations at $Re = 500$.

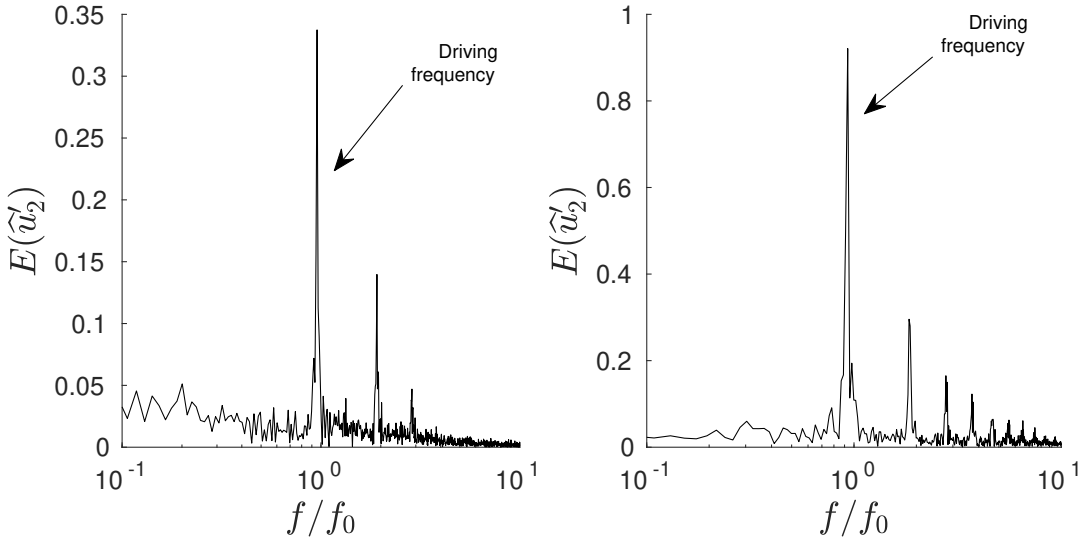

(a) Probe location: $\widehat{x}_1 = 0$, $\widehat{x}_2 = 2.5$.

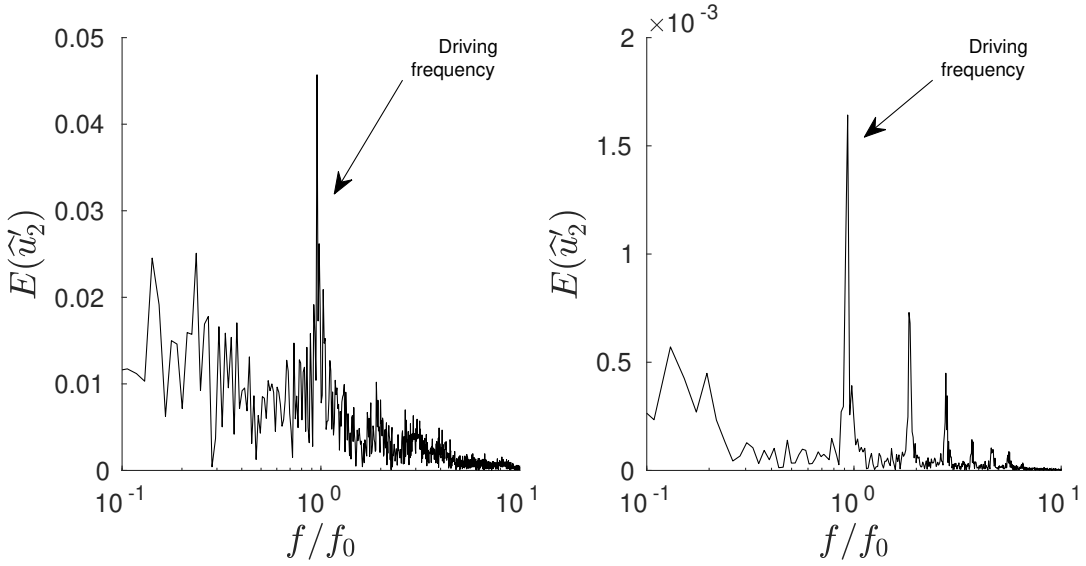

(b) Probe location: $\widehat{x}_1 = 5$, $\widehat{x}_2 = 2.5$.

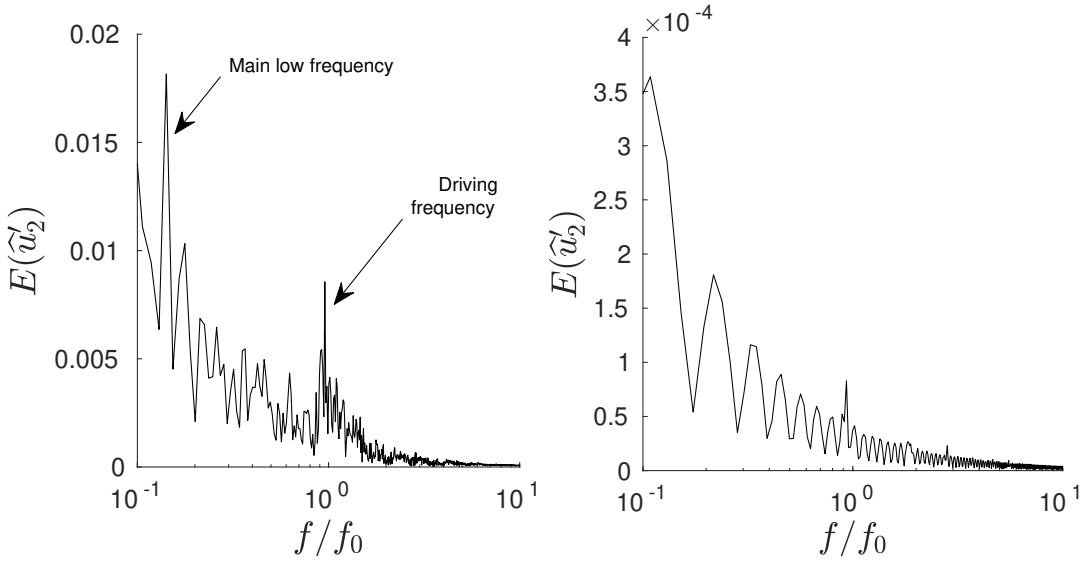

(c) Probe location: $\widehat{x}_1 = 10$, $\widehat{x}_2 = 2.5$.

Figure 5.10: Energy spectrum of the span-wise (axisymmetric) averaged stream-wise velocity for the slotted (left) and circular (right) configurations at $Re = 500$.

5.2 Time and phase averaged flow

Time and phase averaged magnitudes are computed by averaging the last 20 actuator cycles in order to obtain time-accurate statistics (see Section 4.4). In the upcoming analysis, the flow at $Re = 500$ is selected as representative of all the Reynolds numbers studied. Under these circumstances, the major vortices have been identified using velocity streamlines and with regions where $Q > 0$, which correspond to the shadowed grey areas on the next figures.

5.2.1 Slotted configuration

Four major vortices (ϑ_1 to ϑ_4) have been identified in the time averaged flow of the slotted configuration, displayed in Fig. 5.11. They are denoted following the convention set by Silva-Llanca [16].

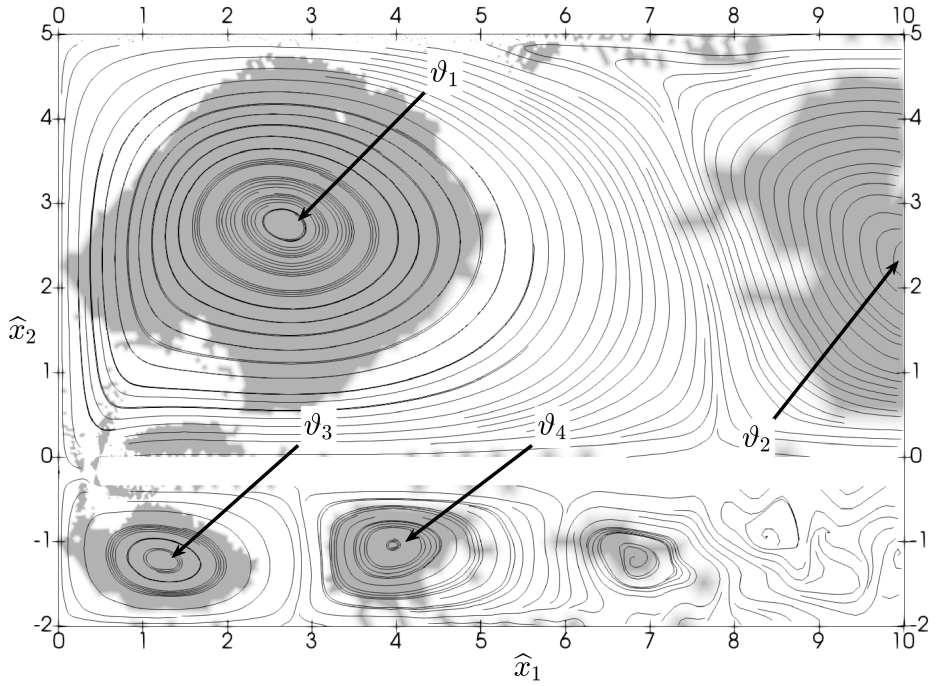

Figure 5.11: Time and span-wise averaged velocity streamlines for the slotted configuration at $Re = 500$ with the regions with $Q > 0$ highlighted in the background (right-hand half of the computational domain).

The result of the coalescence of the vortices ejected from the actuator lips that impinge into the wall is a large clock-wise rotating vortex, ϑ_1. A second vortex, ϑ_2, occurs as a result of the interaction between the downwards flow and the bottom wall. It has already been reported by [55], and is characteristic of the enclosed configuration therefore, is not present in the open configurations, e.g., of Silva-Llanca [16]. These two major vortices, ϑ_1 and ϑ_2, dominate the external flow field

and the positions of their centers, identified by the point where there is a local maximum of Q, have been plotted in Fig. 5.12, where an increase on the x_1 direction with the Reynolds number can be seen. This fact is also seen in the jet half-width or wake, defined as the distance from the centerline where the velocity deficit has decayed to one-half of its maximum value, represented in Fig. 5.13, which widens with the Reynolds number. Regarding the latter, it can be seen that for $Re \geq 300$ the jet width is similar, which could be indicative of the turbulent flow being fully developed.

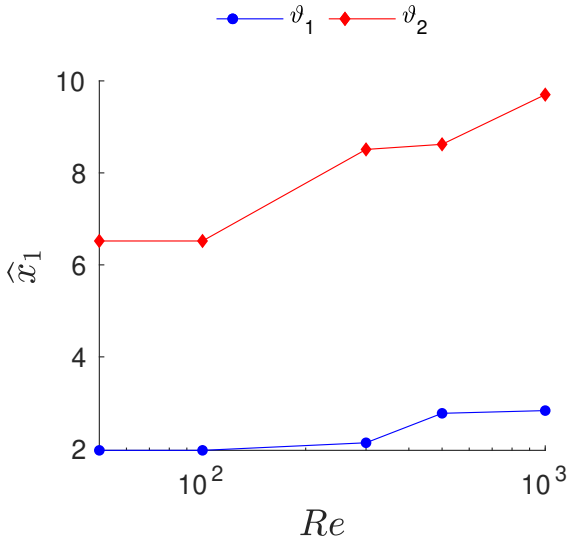

Figure 5.12: Coordinates of the vortex centers for the slotted configuration at different Re.

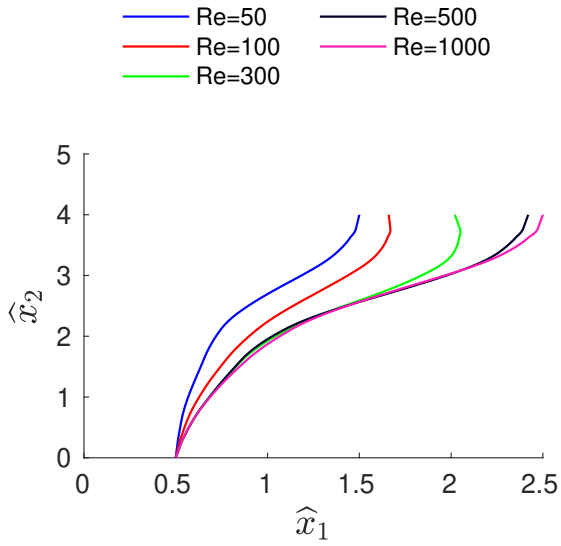

Figure 5.13: Jet half-width with the domain height for the slotted configuration at various Reynolds numbers.

The dynamics of the flow can be appreciated from the phase and span-wise averaged flow in Fig. 5.14. During the ejection (Fig. 5.14a, $t = 0$), a vortex is expelled from the SJA outlet. This vortex is denoted as Θ_1 following the convention set by Silva-Llanca [16]. It eventually merges with the vortex expelled in the previous cycle (Θ_0) at the moment of the impingement (Fig. 5.14b, $t = \tau/4$). At this point and when the suction stroke begins (Fig. 5.14c, $t = \tau/2$), an additional vortical structure (Θ_s) is created near the impingement point. It sweeps the surface from left to right until it is dissipated. Moreover, Θ_s is identified as the main heat transfer enhancement mechanism for jets in the near wall region, which is consistent with the results published in [16, 47, 48, 53]. The counter clock-wise Θ_2 vortex, that is created and destroyed twice per cycle (Figs. 5.14c and 5.14d), is also particular of the enclosed configuration. It merges with Θ_s while the latter is sweeping the heated wall, which has implications in the heat transfer mechanism, as it is further discussed.

The flow inside the SJA cavity is also complex and similar to the external flow. Two major structures (see Fig. 5.11), ϑ_3 and ϑ_4, appear as a result of the flow being ingested back into the cavity. The coherent structure ϑ_4 is the analogous of ϑ_2 but inside the cavity. Regarding the flow dynamics, a vortex, Θ_3, rolls down from the actuator lips and impinges into the actuator membrane (Fig. 5.14c,

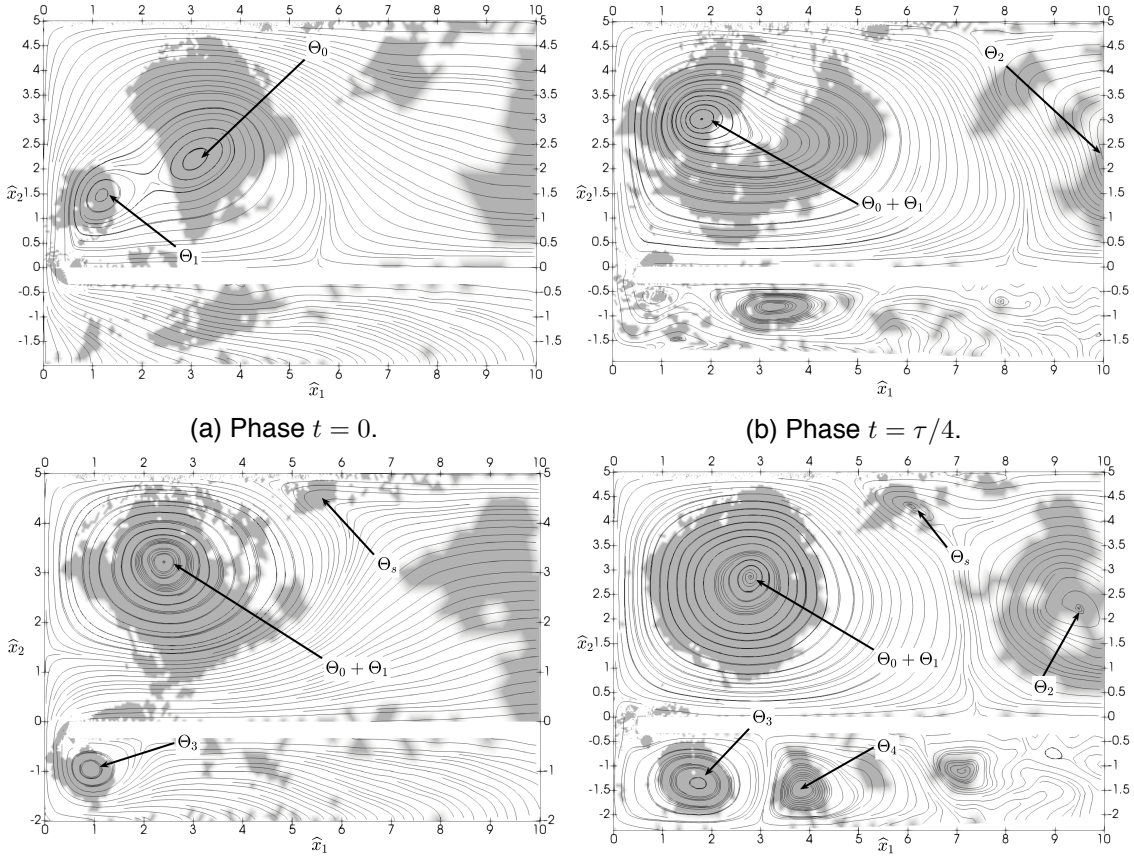

(a) Phase $t = 0$.

(b) Phase $t = \tau/4$.

(c) Phase $t = \tau/2$.

(d) Phase $t = 3\tau/4$.

Figure 5.14: Phase and span-wise averaged velocity streamlines for the slotted configuration at $Re = 500$ with the regions with $Q > 0$ highlighted in the background (right-hand half of the computational domain).

$t = \tau/2$), where heat transfer occurs. Eventually another coherent structure, Θ_4, appears due to the aforementioned process (Fig. 5.14d, $t = 3\tau/4$).

The conditions at the SJA outlet are important in order to understand the jet dynamics. In this line, span-wise and phase averaged stream-wise velocity profiles at the SJA neck are shown in Fig. 5.15. Although there is a similarity when comparing the stream-wise velocity profiles (due to having considered the same JFC), the flow is not symmetrical between the ejection and suction strokes. During the ejection ($t = 0$), the stream-wise velocity shows a sinusoidal profile due to the effect of the SJA neck, while during the suction ($t = \tau/2$) the profile is nearly uniform. Moreover, during the transition between ejection and suction ($t = \tau/4$ and $t = 3\tau/4$), the flow is reversed at the vicinity of the wall, having implications for the development of models for the flow at the SJA outlet. This behavior is in line to what is observed in [15] when modeling the SJA cavity.

5.2.2 Circular configuration

A clock-wise rotating vortex ϑ_1 has also been identified in the circular configuration, albeit it appears much smaller than the slotted counterpart (see Fig. 5.16). Another major vortex appears, denoted as ϑ_0, and corresponds to the impinging main vortex of the previous cycle, as it is further seen. This vortex differs from ϑ_2 of the slotted configuration in the sense that ϑ_2 appears due to the interaction of the flow far from the jet centerline with the bottom wall. Moreover, the potential core and the trailing jet are visible in the vicinity of the jet centerline in the circular configuration, but are not present in the slotted configuration.

As with the slotted configuration, the dynamics of the flow can be better detected when the phase averaged flow is inspected. In this sense Fig. 5.17 displays the phase averaged flow for the circular configuration. Its dynamics are significantly different. Following the impingement and during the suction part of the cycle, the vortex Θ_1 sweeps the surface until about $\widehat{x}_1 = 3$, with the effect of the trailing jet mostly seen until about $\widehat{x}_1 = 1$ (Fig. 5.17c, right). As the vortex Θ_1 sweeps the impingement surface, it starts to lose coherence and eventually separates from the impingement area. At the start of the next expulsion cycle (Fig. 5.17a, $t = 0$), Θ_1 becomes Θ_0 and the dynamics repeat themselves.

The condition at the SJA outlet of the circular configuration are inspected in Fig. 5.18 by means of phase averaged stream-wise velocity profiles. There is an asymmetry between the flow between the ejection and suction strokes, as in the slotted configuration. In the circular configuration, the flow during the ejection ($t = 0$) and during the suction ($t = \tau/2$) is nearly "plug-like". However, during the transition between ejection and suction ($t = \tau/4$ and $t = 3\tau/4$), the flow is reversed at the vicinity of the wall, much like the slotted configuration, hence also having implications for the development of models for the flow at the SJA outlet.

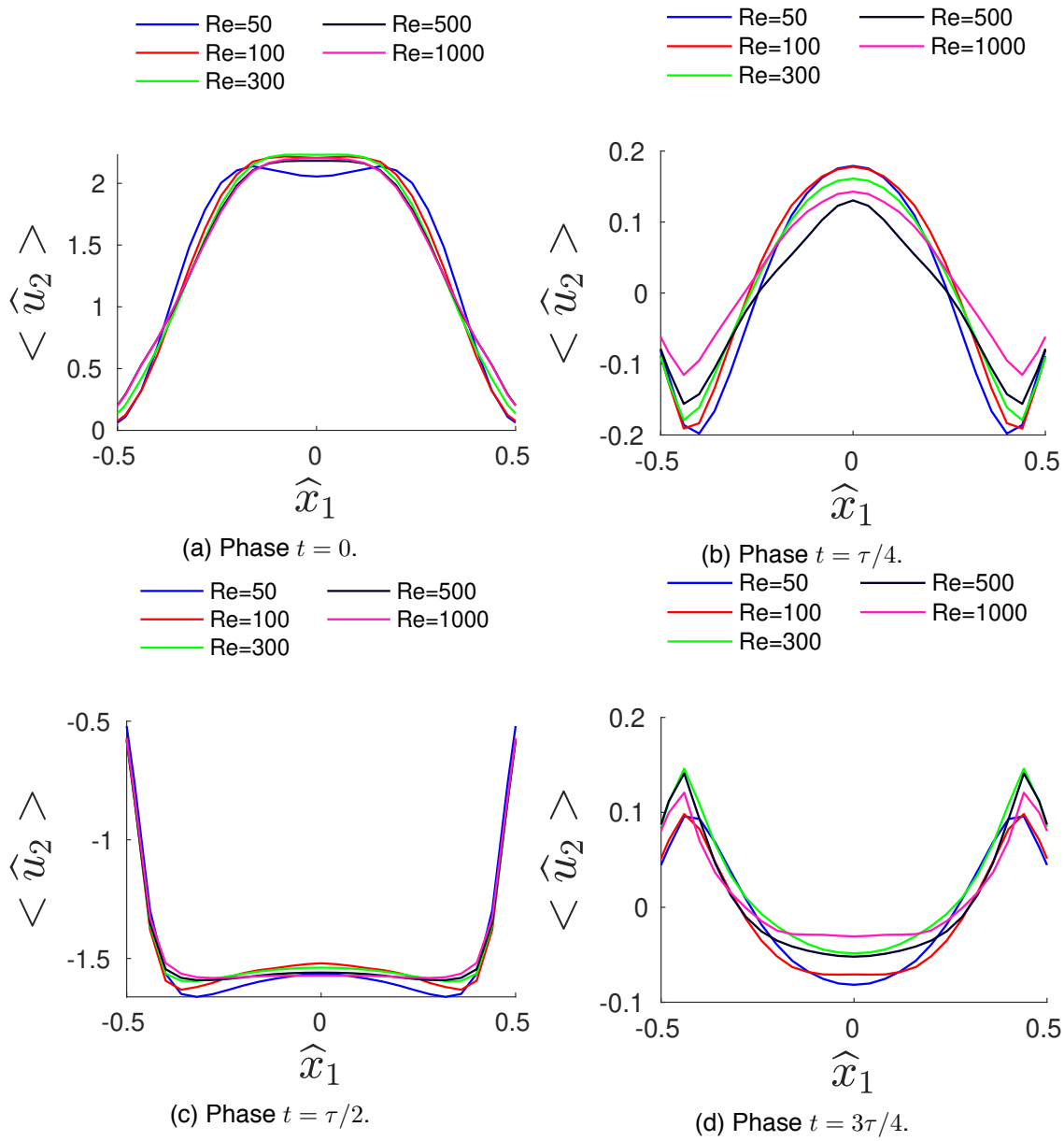

(a) Phase $t = 0$.

(b) Phase $t = \tau/4$.

(c) Phase $t = \tau/2$.

(d) Phase $t = 3\tau/4$.

Figure 5.15: Phase and span-wise averaged velocity profiles at the actuator orifice for the slotted configuration at all the Reynolds studied.

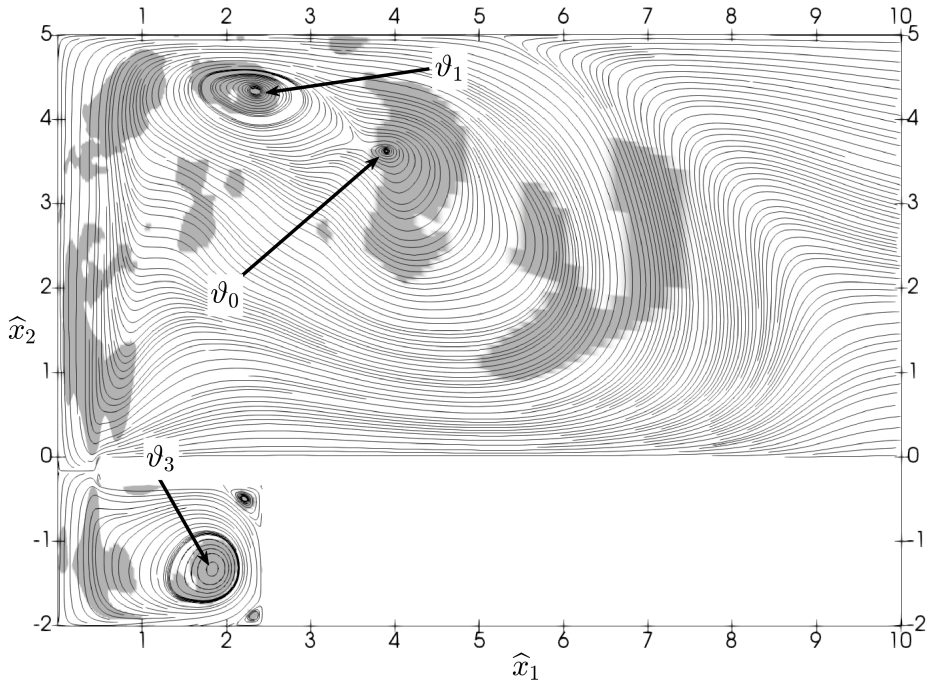

Figure 5.16: Time averaged velocity streamlines for the circular configuration at $Re = 500$ with the regions with $Q > 0$ highlighted in the background (right-hand half of the computational domain).

5.3 Comparison of the slotted and circular configurations

The results presented in Section 5.1 and Section 5.2 show fundamental differences on the flow morphology between the slotted and circular configurations. The first striking difference is at $Re = 50$, where in the slotted configuration, vortex stretching causes loss of coherence of the vortex dipoles. In the circular configuration, the Kelvin-Helmholtz instability is not present and there is no visible trailing jet thus the main vortex ring keeps its coherence. This results in less mixing and lower SJA expulsion and ingestion temperatures of the circular configuration; whereas mixing is enhanced in the slotted configuration.

The time-averaged and phase-averaged flows are also different for both configurations. While in the slotted configuration, two vortices appear side by side, in the circular configuration there is one big vortex. This phenomenon is due to the difference in width of the cavities, which is being imposed by the JFC. On the phase-averaged flow, the vortex dynamics of the circular configuration show a clear contrast with the dynamics of the slotted configuration. In the former, no mixing between Θ_1 and Θ_0 is observed nor the appearance of Θ_2, in contrast to what is observed in the latter. In contrast, the time dynamics of both configurations are similar, with a low broadband frequency appearing in the energy spectrum of the signals at the same frequency, roughly corresponding to 7 actuator cycles.

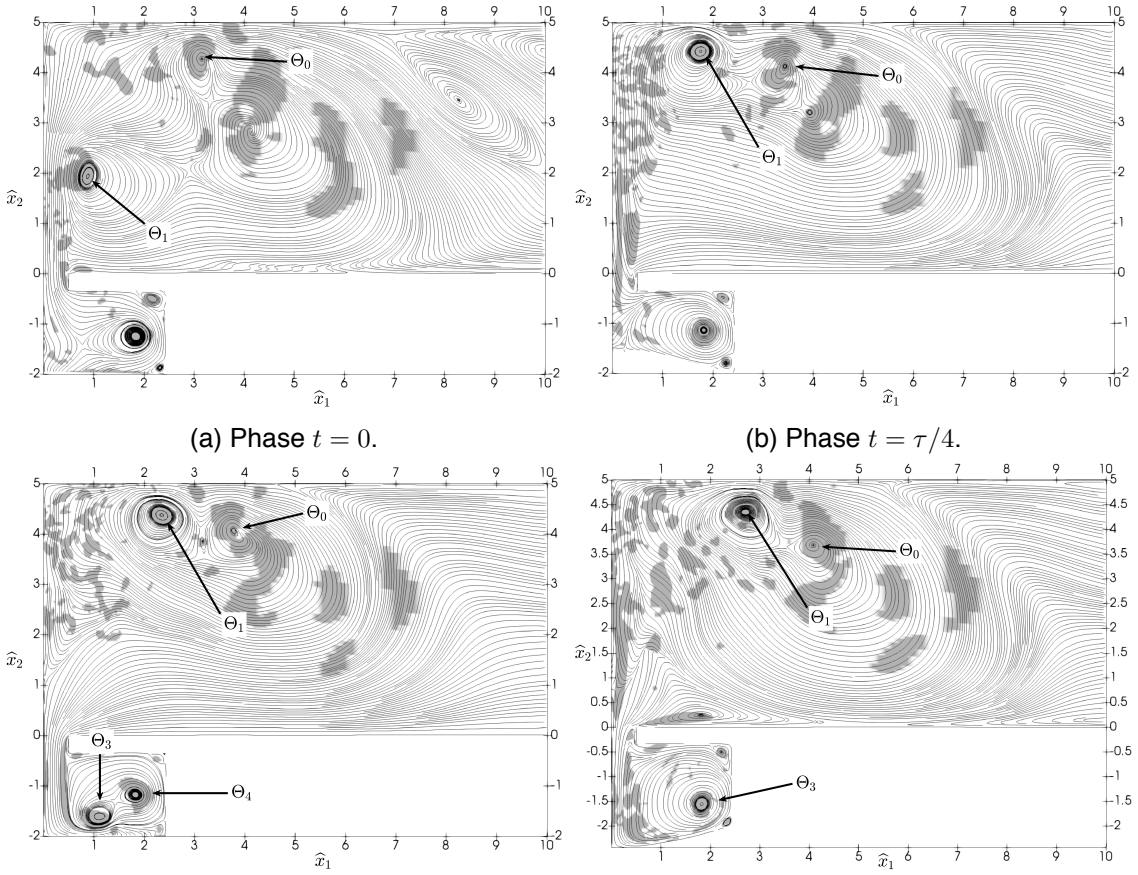

(a) Phase $t = 0$.

(b) Phase $t = \tau/4$.

(c) Phase $t = \tau/2$.

(d) Phase $t = 3\tau/4$.

Figure 5.17: Phase averaged velocity streamlines for the circular configuration at $Re = 500$ with the regions with $Q > 0$ highlighted in the background (right-hand half of the computational domain).

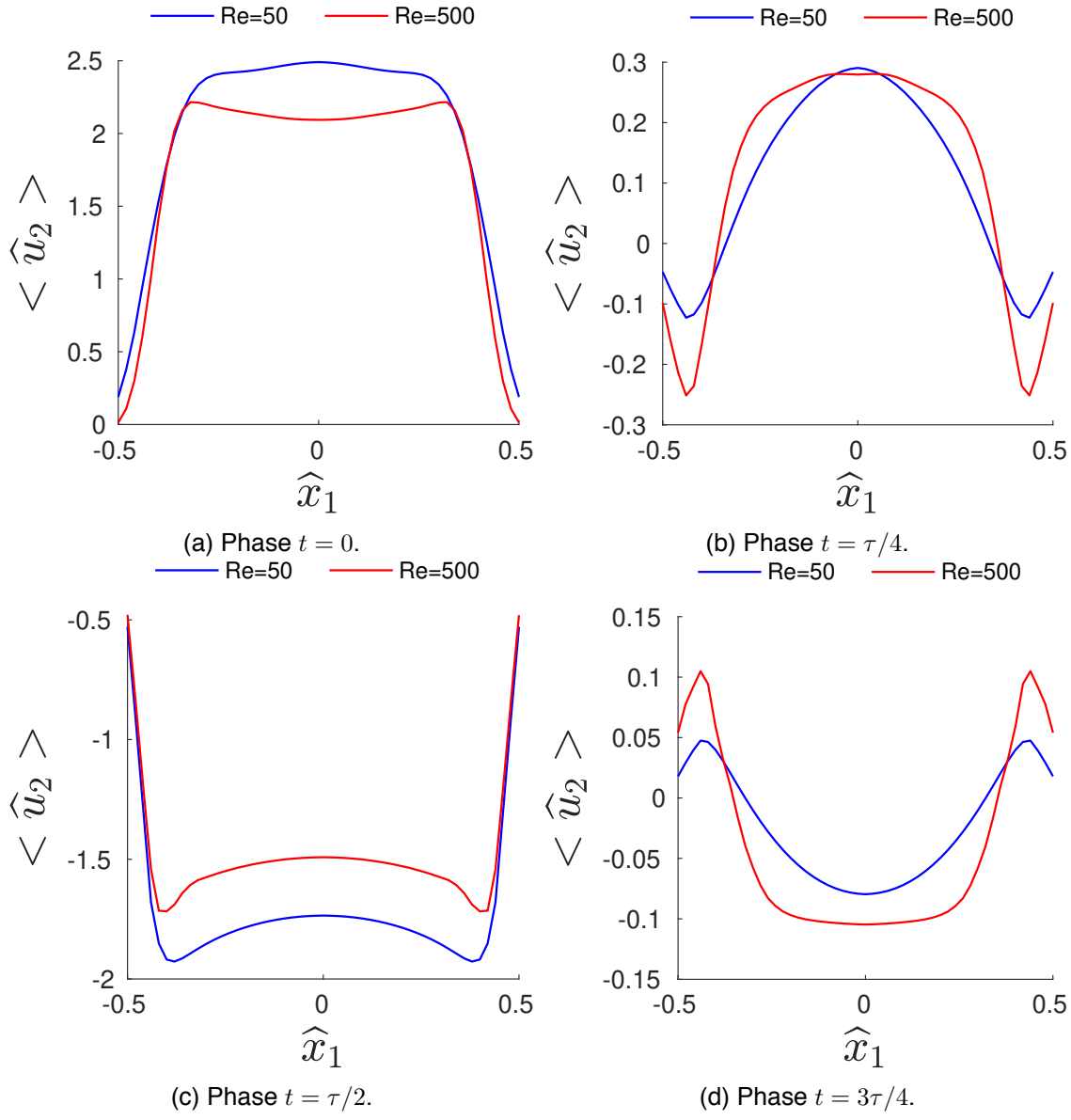

(a) Phase $t = 0$.

(b) Phase $t = \tau/4$.

(c) Phase $t = \tau/2$.

(d) Phase $t = 3\tau/4$.

Figure 5.18: Phase averaged velocity profiles at the actuator orifice for the circular configuration at all the Reynolds studied.

In [108], visualizations of impinging synthetic jets are presented for different JFC on PIV data by using a parameter (s) that is reported to be efficient for the identification of the vortex trajectories. It helps to characterize the strength of a synthetic jet vortex ring and to quantify the swirling and shearing strength of a vortex. It is defined as the negative value of the discriminant of complex eigenvalues of the local velocity gradient tensor [109], i.e.,

$$s = -\frac{1}{4}\left(\left(\frac{\partial \overline{u}_1}{\partial x_1}\right)^2 + \left(\frac{\partial \overline{u}_2}{\partial x_2}\right)^2\right) + \frac{1}{2}\frac{\partial \overline{u}_1}{\partial x_1}\frac{\partial \overline{u}_2}{\partial x_2} - \frac{\partial \overline{u}_1}{\partial x_2}\frac{\partial \overline{u}_2}{\partial x_1} \tag{5.2}$$

and allows to disregard much of the weaker turbulent vorticity. This parameter has been used in the present work to compare the time-averaged flow of both configurations in Fig. 5.19. The difference of the jet morphology for the two configurations studied is again stressed: the slotted configuration has a wide structure that corresponds to the coalescence of the expelled vortices with a wide vortex path, whereas the axisymmetric configuration has narrower vortex path that becomes wider at the impingement. This has been identified due to the higher velocity of the fluid in the trailing jet that impacts upon the vortex and is in good agreement with what has been observed for high JFC synthetic jets [28, 108]. These effects have implications in the jet width as it is further discussed.

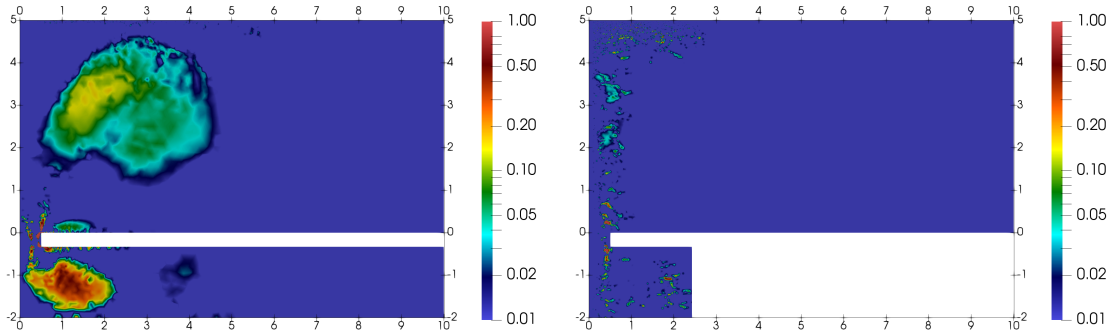

(a) Slotted configuration. (b) Circular configuration.

Figure 5.19: Time averaged distributions of the swirl and shear strength parameter s (Eq. 5.2, right-hand half of the computational domain).

The spatial distribution of the phase averaged turbulent kinetic energy ($\langle k \rangle$) at the expulsion stroke ($t = 0$) is plotted in Fig. 5.20. It is defined as half of the trace of the Reynolds stress tensor

$$\langle k \rangle = \frac{1}{2}\left\langle u_i' u_i' \right\rangle \tag{5.3}$$

where $u_i' = u_i - \langle u_i \rangle$. Note that, as defined in Section 4.2, the operator $\langle \cdot \rangle$ denotes a phase average, instead of the operator $\overline{\cdot}$ that denotes a time average. The different jet morphologies from both configurations are again emphasized. The jet formed in the slotted configuration is clearly of turbulent nature, starting in the region of the orifice at $\widehat{x}_1 = 0.5$, where vortex stretching starts to

occur, up to $\widehat{x}_2 = 2$. Also, notice a certain widening as the energy is being transported downstream towards the impingement. On the other hand, the jet formed in the axisymmetric configuration concentrates its turbulent energy on the trailing jet that rises from the actuator lips to the position of the main vortex ring. Moreover, it has lower turbulence levels that are more concentrated in the region of the actuator orifice ($\widehat{x}_1 = 0.5$), in contrast to its slotted counterpart. In addition, a zone of low turbulent kinetic energy near the jet centerline on the axisymmetric configuration that corresponds to the potential core is also observed.

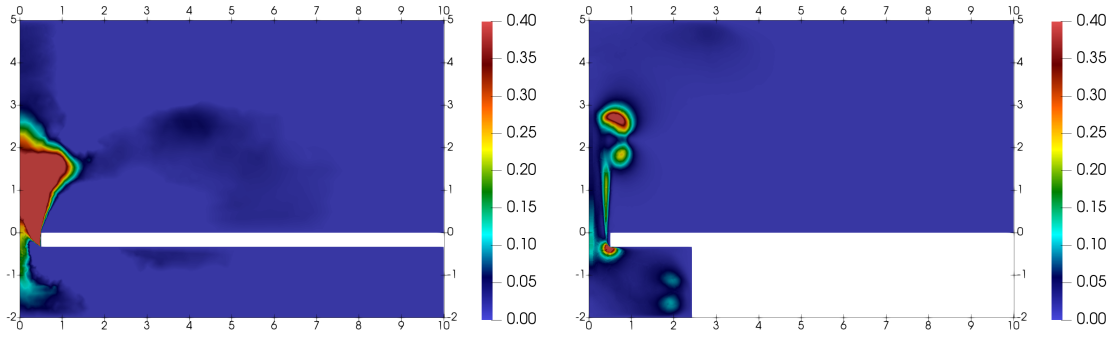

(a) Slotted configuration.

(b) Circular configuration.

Figure 5.20: Distribution of the turbulent kinetic energy (Eq. 5.3) at the expulsion stroke $t = 0$ (right-hand half of the computational domain).

The temporal evolution of the vertical position of the aforementioned Θ_1 vortex is plotted in Fig. 5.21 for both configurations to further analyze the vortex dynamics. It can be seen that, for the circular configuration, the impingement is reached at $t/\tau \approx 0.4$, whereas for the slotted configuration it occurs at $t/\tau \approx 0.5$. This is due to the vortex Θ_1 being delayed by the interaction with Θ_0, which occurs at about $t/\tau \approx 0.4$ only for the slotted configuration. The vortex Θ_1 remains at $\widehat{x}_2 > 4$ as it sweeps the impingement surface until it loses all its coherence on the axisymmetric configuration, while Θ_1 merges with Θ_0 and remains at $\widehat{x}_2 \approx 3$ on the slotted configuration. As a result, the vortex Θ_1 in the circular configuration reaches the impingement surface before the slotted one. This has an impact on the jet formation, which is defined as an outward velocity along the jet axis that corresponds to the generation and escape of a vortex ring [32]. This definition is relevant and is tied to the data shown in Fig. 5.21. As it can be seen, the advection velocity of the vortices in the circular configuration is higher than in the slotted configuration. Therefore, the critical value of the JFC is higher in the slotted configuration. In other words, the circular configuration allows lower JFC than the slotted configuration. Also, at the same jet ejection velocity and orifice diameter, the formation of vortex rings of the circular configuration can occur at higher frequencies than the formation of vortex dipoles of the slotted configuration.

Another important jet parameter to analyze is the jet half-width or wake, represented in Fig. 5.22

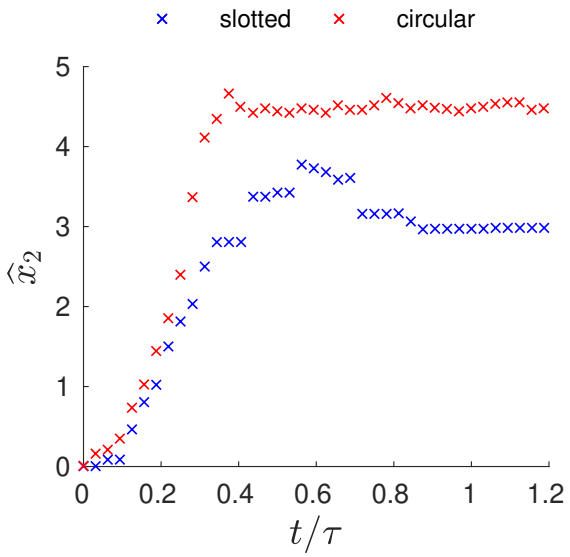

Figure 5.21: Temporal evolution of the vertical position of the Θ_1 vortex for both configurations.

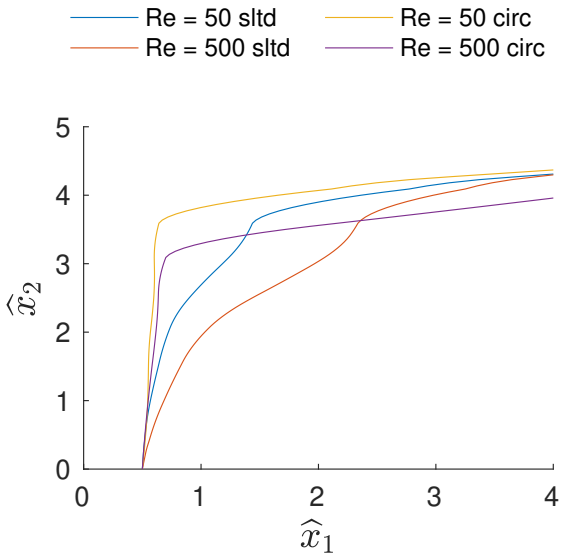

Figure 5.22: Jet half-width with the domain height for both configurations at $Re = 50$ and $Re = 500$.

for both configurations studied. As it can be seen, the slotted configuration jet is wider than its counterpart on the circular configuration. This is again due to the morphology of the vortex rings and vortex dipoles. Notice that the zone up to $\widehat{x}_2 = 1$ for $Re = 50$, the jet widths of the slotted and circular configurations are equal. This is due to laminar vortices being advected from the orifice in both configurations that undergo equal trajectories.

Summarizing:

- The jet in the circular configuration is more concentrated on the jet centerline compared with its slotted counterpart, where an interaction between the vortices Θ_0 and Θ_1 is observed. This results in a wider jet on the slotted configuration.
- The vortices on the circular configuration reach the impingement before the slotted ones, which results in a more abrupt change of width slope in the jet upper part (as a result of Θ_1 or Θ_s sweeping the impingement surface).
- The effect of the vortex shedding on the main structures at the vicinity of the orifice and the higher turbulence levels cause a widening of the jet on the slotted configuration, which is not observed in the circular configuration.
- The jet width of the slotted configuration increases with Re as a result of an increased mixing between Θ_0 and Θ_1. On the axisymmetric configuration, it is similar for both Re as the main vortex ring does not lose its coherence until after the impingement.

6

Heat Transfer Analysis of Impinging Synthetic Jets

The heat transfer performance of a synthetic jet is tightly related to its flow morphology. For this reason, the discussions presented in this chapter are related to those on Chapter 5 and need to be understood together. This chapter starts with a discussion on the instantaneous and the averaged temperature. In order to analyze the temperature field is necessary to understand the heat transfer capabilities of a synthetic jet. This section is split between the slotted and circular configurations, as done for the flow analysis. A discussion of the temporal analysis of the temperature signals is also included. Then, the instantaneous and averaged heat transfer is analyzed. The thermal footprints and then the heat transfer performance are analyzed for each configuration studied. Finally, this chapter ends with a comparison of the heat transfer capabilities of slotted and circular synthetic jets.

6.1 Instantaneous and time and phase averaged temperature

Before analyzing the heat transfer performance of the synthetic jet actuator, it is worth analyzing the instantaneous and time and phase averaged temperature profiles. These profiles maintain a close relation with the heat transfer performance and are of help in understanding the heat transfer capabilities of synthetic jets.

6.1.1 Slotted configuration

The instantaneous dimensionless temperature at the SJA outlet is shown in Fig. 6.1 for the slotted configuration at all Reynolds numbers studied. The outlet temperature is quite hot, with about $\widehat{T} \approx 0.1$ for $Re = 50,\ 100$ and about $\widehat{T} \approx 0.2$ for $Re > 100$. Moreover, the peak to peak temperature variation is large for all Reynolds numbers studied, although the amplitude of the fluctuations decreases with Reynolds due to the enhanced mixing in both cavities. The fluid cannot be cooled completely inside the cavity, even assuming that the whole cavity boundaries are at T_∞. This results in a decrease of the cooling efficiency of the jet, as seen by Vukasinovic and Glezer [55]. However, as previously seen, this effect stabilizes with time and a stationary state can be reached.

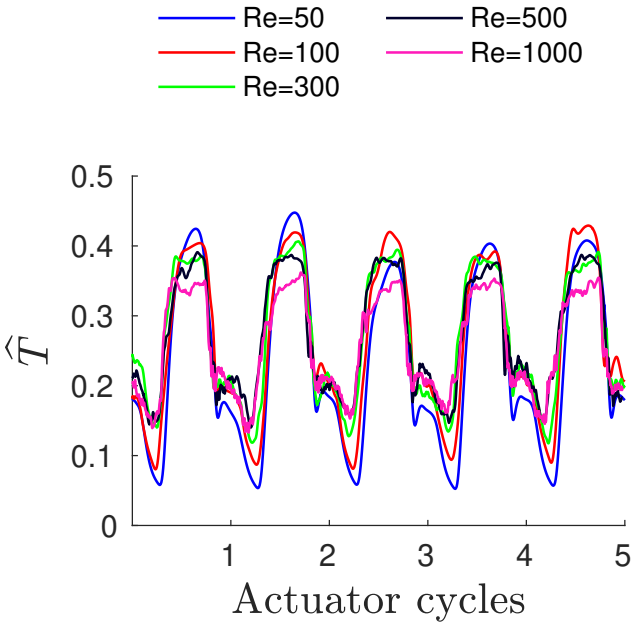

Figure 6.1: Time evolution of the span-wise averaged temperature at the SJA outlet for the slotted configuration.

The temperature conditions at the SJA outlet are important to understand the heat transfer mechanisms. In this line, span-wise and phase averaged temperature profiles at the SJA neck are shown in Fig. 6.2. A notable difference of temperature between ejection and suction parts of the cycle is again observed. In addition, the temperature field becomes more uniform with the Reynolds number, due to the increase in turbulent mixing. This fact strongly supports the validity of an uniform model for the outlet temperature profile for turbulent Reynolds numbers $Re > 100$.

An expression for the temperature at the SJA outlet with the Reynolds number can be obtained from space averaging the data in Fig. 6.2. The correlation, shown in Fig. 6.3, is

$$\left\langle \widehat{T} \right\rangle = aRe^b \tag{6.1}$$

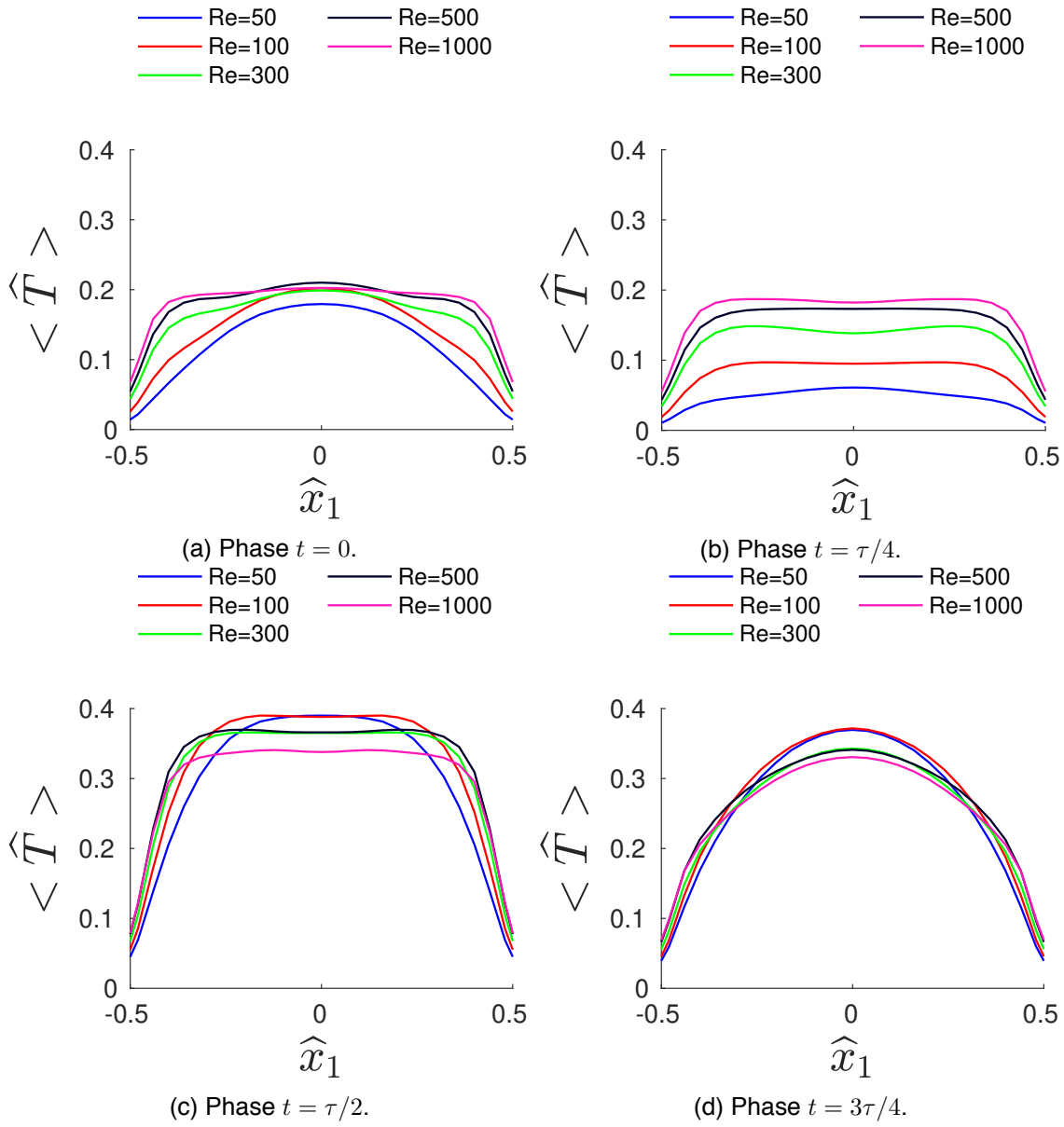

(a) Phase $t = 0$.

(b) Phase $t = \tau/4$.

(c) Phase $t = \tau/2$.

(d) Phase $t = 3\tau/4$.

Figure 6.2: Phase and span-wise averaged temperature profiles at the actuator orifice for the slotted configuration at all the Reynolds studied.

where the coefficients are $a = 0.075$ and $b = 0.137$.

The agreement is fair for all Reynolds numbers (relative error below 6%) although the result from the correlation is more representative of the flow at $Re > 100$ as the temperature at the outlet presents a flatter profile at larger Reynolds numbers. This data can be used to generate a boundary condition for the temperature at the SJA outlet for JFC $= 3$ and a $H/d = 5$. Nevertheless, for other H/d ratios or actuator geometries the outlet temperatures could differ significantly.

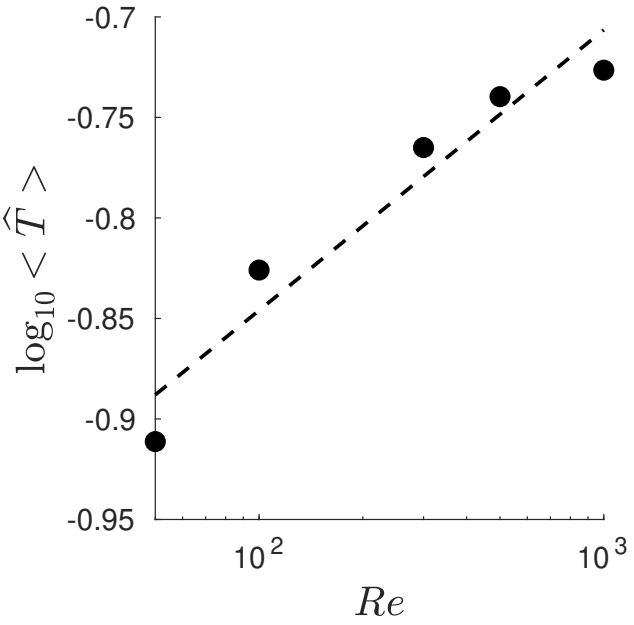

Figure 6.3: Phase and space-averaged SJA outlet temperature during suction for the slotted configuration at different Reynolds numbers. The dashed line correspond to the correlation in Eq. 6.1.

6.1.2 Circular configuration

The temperature of the main vortex ring in the circular configuration is slightly higher than the trailing jet and the potential core as it is being mixed with the recirculating fluid. Nevertheless, both the slotted jet and the circular trailing jet have similar temperatures, probably due to the intense mixing created by the vortex stretching and the Kelvin-Helmholtz instability respectively. During the suction part of the cycle, the presence of the potential core in the circular configuration results in less mixing in the SJA neck and thus higher suction temperature. However, the fluid is rapidly cooled in the circular configuration as the amount of surface with higher velocities is increased. These can be seen in Fig. 6.4, where the variation of dimensionless temperature at the SJA outlet is plotted for the circular configuration. Moreover, a strong difference is observed in Fig. 6.4 for $Re = 50$ and $Re = 500$. This difference is due to the change of regime and the appearance of a trailing jet at $Re = 500$ as discussed in Section 5.1.

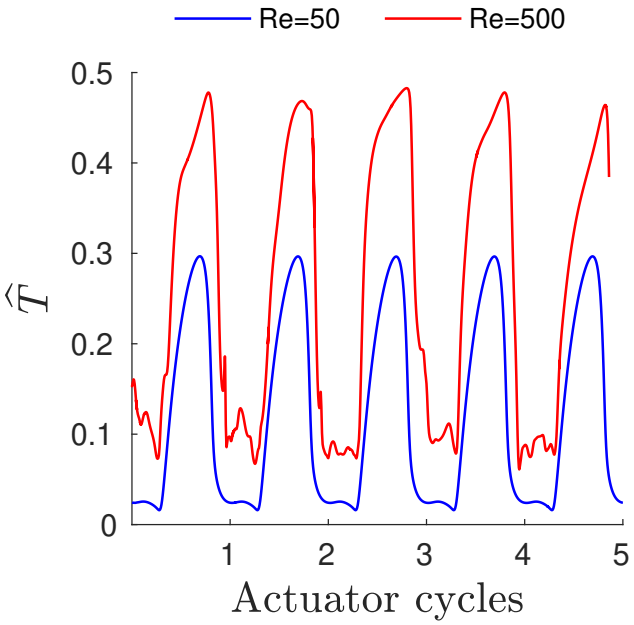

Figure 6.4: Time evolution of the temperature at the SJA outlet for the circular configuration.

As in the slotted configuration, the temperature profiles at the SJA outlet are analyzed in Fig. 6.5. Again, a noticeable difference on the temperature can be observed between the cases at $Re = 50$ and $Re = 500$. Moreover, there is a contrast on the profiles between ejection and suction parts of the cycle independently of the Reynolds number. The temperature at the jet centerline ($\widehat{x}_1 = 0$) is slightly lower than in the surroundings, which is indicative of less mixing occurring on the circular configuration. In this case, the use of a uniform model for the outlet temperature profile cannot be entirely accurate.

6.1.3 Frequency analysis of the temperature

It is also interesting to identify the frequencies related to the temperatures in the low velocity zones. To do so, the same set of numerical probes presented in Section 5.1.3 is used to record the temporal variation of the temperature during the whole simulation.

The signal of different probes at $Re = 500$ located at the same vertical distance from the bottom wall $\widehat{x}_2 = 2.5$ but at different $\widehat{x}_1$ distance from the jet centerline are plotted in Fig. 6.6. The energy spectrum of these signals is plotted in Fig. 6.7. As can be seen from the figures and analogously to the analysis of the velocity probes, the signal of probe located in the centerline of the jet is dominated by the periodicity of the ejection and suction events. However, when analyzing points away from the jet centerline, the footprint of the cyclic ejection/suction event becomes confused with the background noise, as well as the low frequency modulation appearing on the velocity

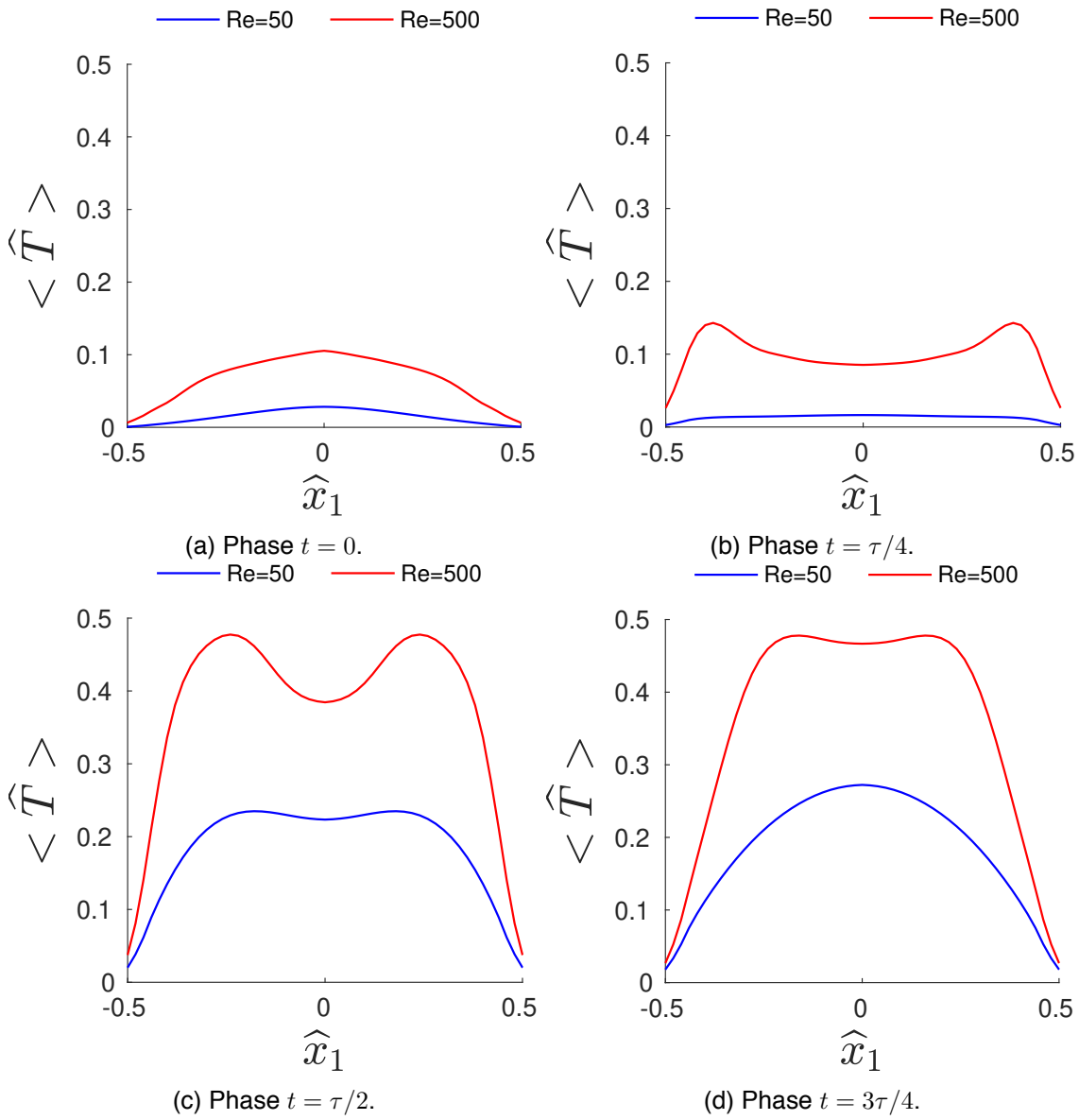

(a) Phase $t = 0$.

(b) Phase $t = \tau/4$.

(c) Phase $t = \tau/2$.

(d) Phase $t = 3\tau/4$.

Figure 6.5: Phase averaged temperature profiles at the actuator orifice for the circular configuration at all the Reynolds studied.

spectra. This is indicative of the complexity of the temperature field and is likely to have implications in the heat transfer capabilities of both configurations.

6.2 Instantaneous and time-averaged heat transfer

The instantaneous local Nusselt number at the hot wall is defined as

$$Nu = \left.\frac{\partial \widehat{T}}{\partial \widehat{x}_2}\right|_{\widehat{x}_2=H/d} \tag{6.2}$$

and is evaluated for both the slotted and circular configurations. The Nusselt number represents the dimensionless heat transfer and is used to measure the cooling performance of the SJA.

6.2.1 Slotted configuration

The instantaneous local Nusselt number at the hot wall is shown in Figs. 6.8, 6.9, 6.10 and 6.11 for various phase instants at all the Reynolds numbers considered. The thermal footprint can be clearly seen on the hot wall, which intensifies with the Reynolds number, as expected. The maximum heat transfer occurs at the moment of the impingement ($t = \tau/4$) and lasts until the start of the suction cycle at $t = \tau/2$. The high Nusselt number regions spread along the heated wall, reaching more homogeneous values thanks to the effect of Θ_s sweeping the wall. The footprint of the turbulent (or transitional for the lower Reynolds number) large-scale elongated vortices can also be seen in the image as regions of high and low heat transfer coefficient following the vortex patterns. The span-wise size of these vortices decreases as the Reynolds number increases. However, the footprint of these structures is lost when averaging the signal and the span-wise and time averaged Nusselt distribution is symmetric.

The time and span-wise averaged local Nusselt number ($\overline{Nu}$) is shown in Fig. 6.12. It is presented for each Reynolds number considered, as well as the results from [20] at $Re = 508$, $Sk = 12.7$ (equivalent to JFC $= 3.15$) for an open configuration. As can be seen, for $Re = 500$, near the stagnation point the agreement with the experimental results is quite good, despite the difference in the configuration and JFC. However, the Nusselt number decays significantly faster than in the open configuration for distances roughly larger than the jet wake. This is due to the aforementioned effect of Θ_s merging into ϑ_2. While in the open configuration Θ_s can freely sweep the heated wall and produce a heat transfer enhancement effect, in the confined configuration this is prevented by ϑ_2.

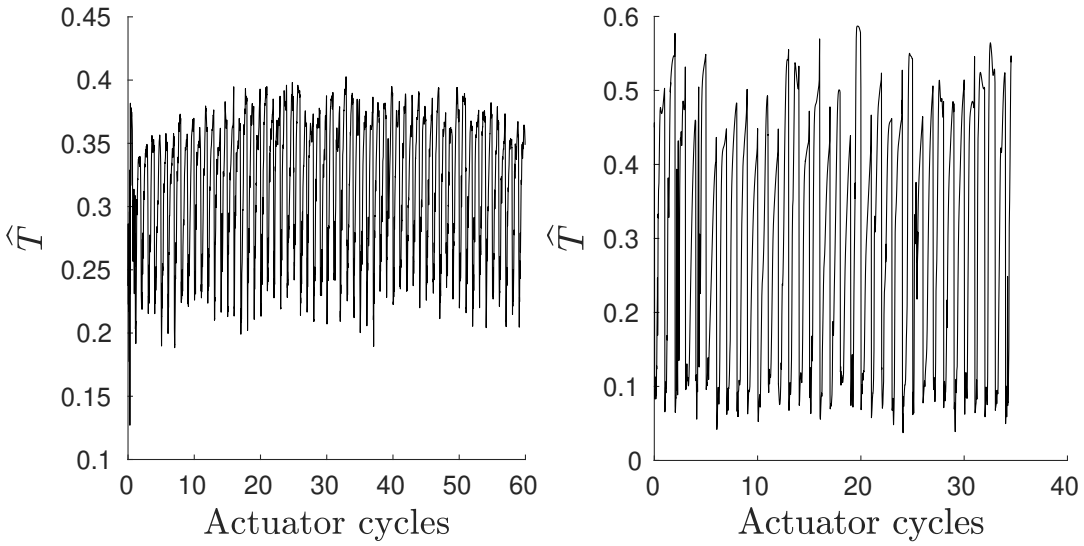

(a) Probe location: $\widehat{x}_1 = 0$, $\widehat{x}_2 = 2.5$.

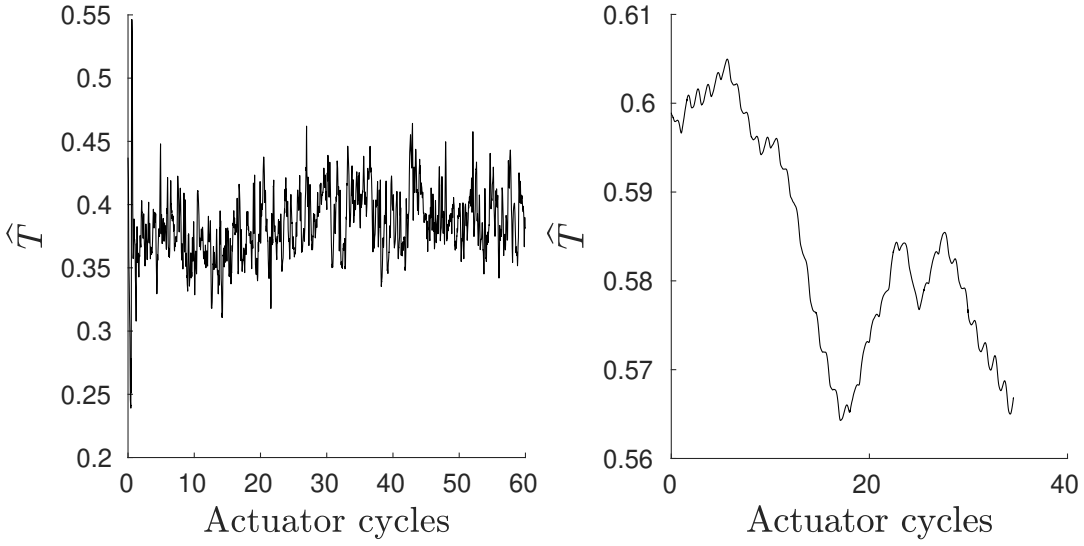

(b) Probe location: $\widehat{x}_1 = 5$, $\widehat{x}_2 = 2.5$.

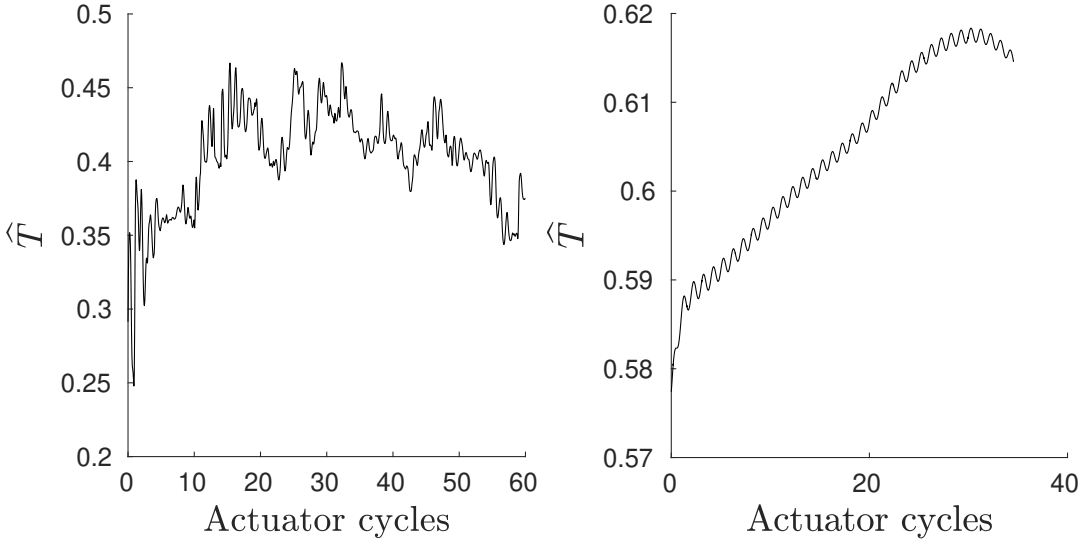

(c) Probe location: $\widehat{x}_1 = 10$, $\widehat{x}_2 = 2.5$.

Figure 6.6: Temporal evolution of the span-wise (axisymmetric) averaged temperature for the slotted (left) and circular (right) configurations at $Re = 500$.

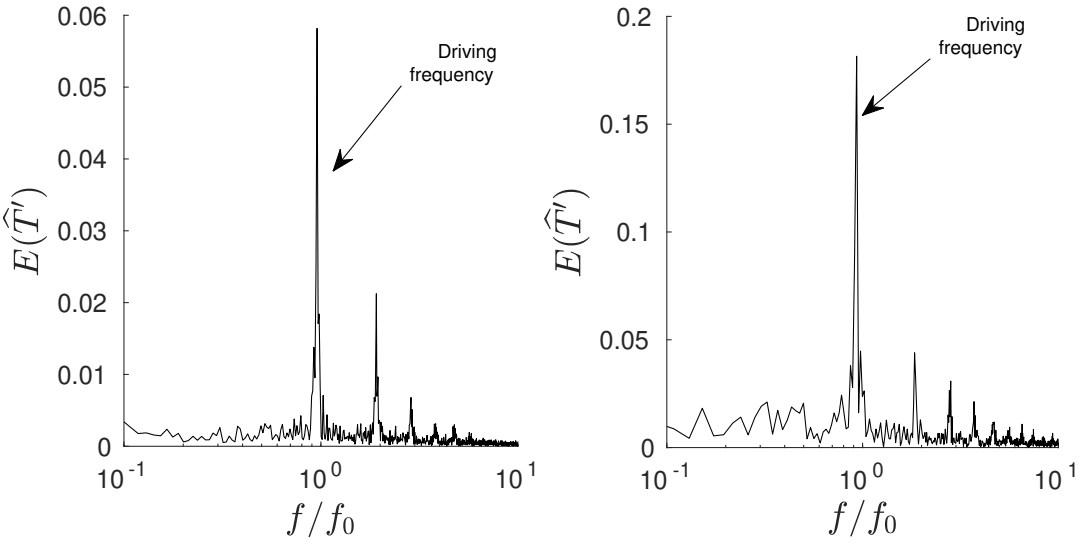

(a) Probe location: $\widehat{x}_1 = 0$, $\widehat{x}_2 = 2.5$.

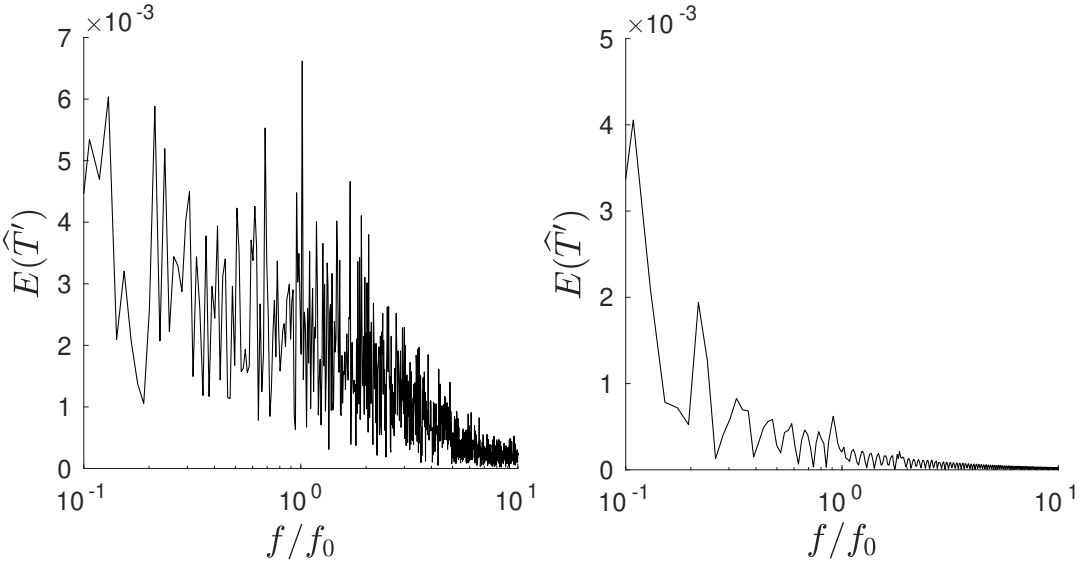

(b) Probe location: $\widehat{x}_1 = 5$, $\widehat{x}_2 = 2.5$.

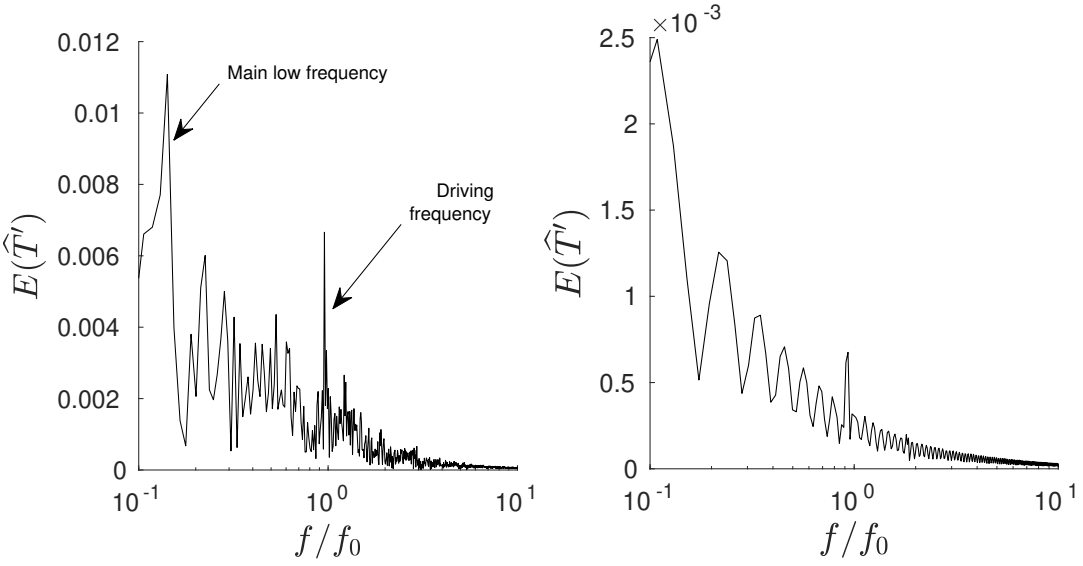

(c) Probe location: $\widehat{x}_1 = 10$, $\widehat{x}_2 = 2.5$.

Figure 6.7: Energy spectrum of the span-wise (axisymmetric) averaged temperature for the slotted (left) and circular (right) configurations at $Re = 500$.

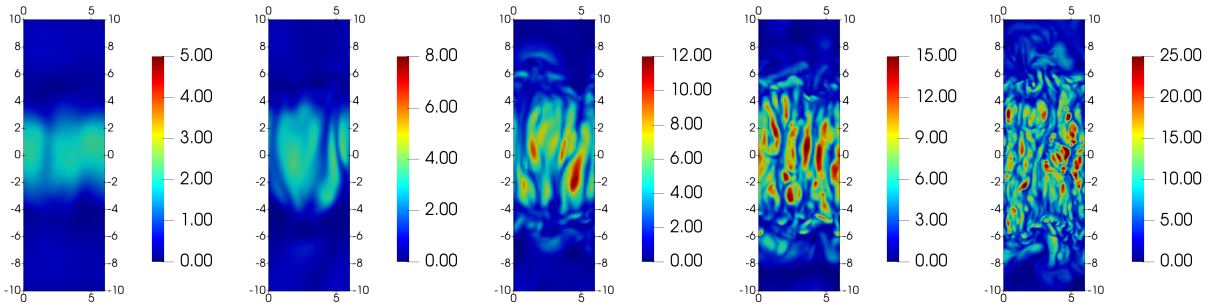

(a) $Re = 50$. (b) $Re = 100$. (c) $Re = 300$. (d) $Re = 500$. (e) $Re = 1,000$.

Figure 6.8: Instantaneous local Nusselt number at the hot wall for the slotted configuration at phase $t = 0$ and all the Reynolds numbers considered.

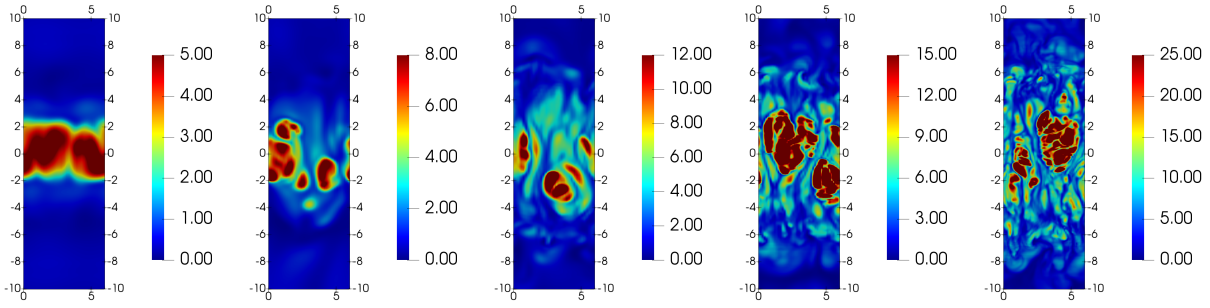

(a) $Re = 50$. (b) $Re = 100$. (c) $Re = 300$. (d) $Re = 500$. (e) $Re = 1,000$.

Figure 6.9: Instantaneous local Nusselt number at the hot wall for the slotted configuration at phase $t = \tau/4$ and all the Reynolds numbers considered.

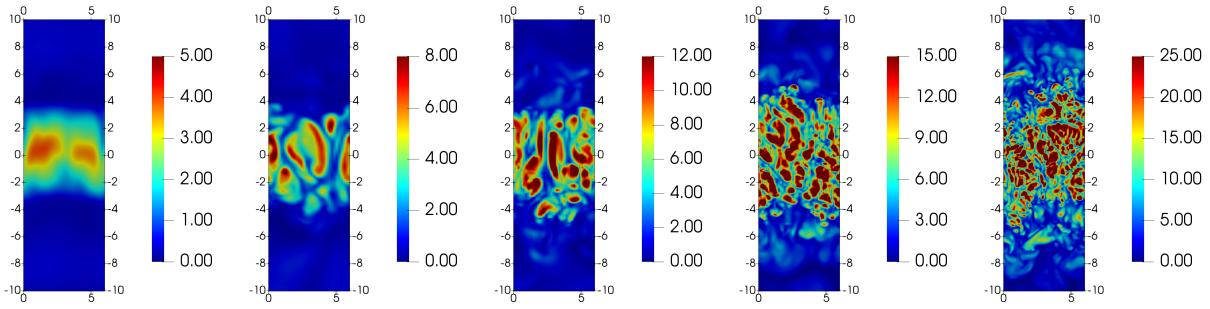

(a) $Re = 50$. (b) $Re = 100$. (c) $Re = 300$. (d) $Re = 500$. (e) $Re = 1,000$.

Figure 6.10: Instantaneous local Nusselt number at the hot wall for the slotted configuration at phase $t = \tau/2$ and all the Reynolds numbers considered.

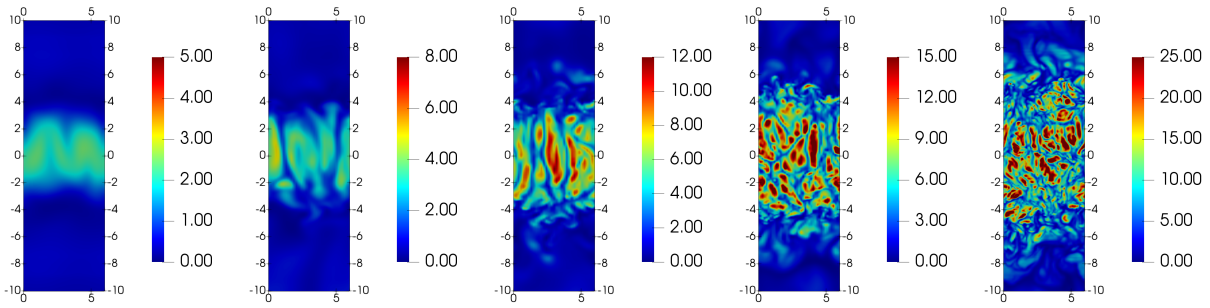

(a) $Re = 50$. (b) $Re = 100$. (c) $Re = 300$. (d) $Re = 500$. (e) $Re = 1,000$.

Figure 6.11: Instantaneous local Nusselt number at the hot wall for the slotted configuration at phase $t = 3\tau/4$ and all the Reynolds numbers considered.

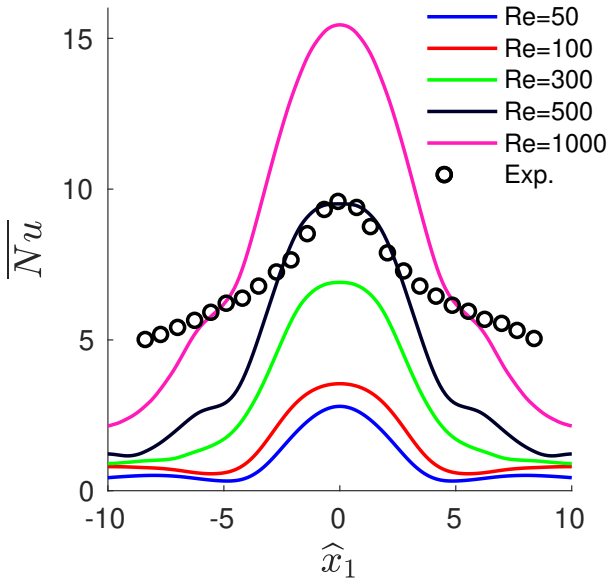

Figure 6.12: Time and span-wise averaged Nusselt number for the slotted configuration at various Reynolds number. The dashed line corresponds to the jet wake half-width for $Re = 500$. The black circles are the experimental results from [20] (open configuration) at $Re = 508$, $Sk = 12.7$.

The time and space averaged overall Nusselt number ($\overline{Nu}_{avg}$), integrated between $\widehat{x}_1 = \pm 5$, for different Reynolds numbers is shown in Fig. 6.13. A correlation is proposed following the work in [52]

$$\frac{\overline{Nu}_{avg}}{\overline{Pr}^{0.42}} = aRe^m \tag{6.3}$$

where $a = 0.115$ and $m = 0.682$. As a means of comparison, the experimental points for the open configuration tested in [20] at JFC $= 3.15$ are plotted in Fig. 6.13. Note that in the figure only the experimental data for $H/d = 5$ is included.

The results obtained from the numerical simulations are in good agreement with the experimental data obtained in opened configurations. Indeed, much of the heat transfer capability of the jet is contained around the jet core, at about $\widehat{x}_1 = \pm 5$, as seen in Fig. 6.12. Hence the averaged data (both in time and space) is expected to be similar in both the open and closed configurations. In fact, the numerical data presented in this work is closely similar to the experimental data when far from the possible influences of the boundary conditions. This also helps to validate the obtained results. Note, however, that the flow configuration is different. This is visible when analyzing points far from the jet core. The faster decay of the Nusselt number in the closed configuration yields a trend slightly under the experimental data, as seen in Fig. 6.13. Notice also that this difference would be increased if the spatial integration interval was increased, e.g., between $\widehat{x}_1 = \pm 10$.

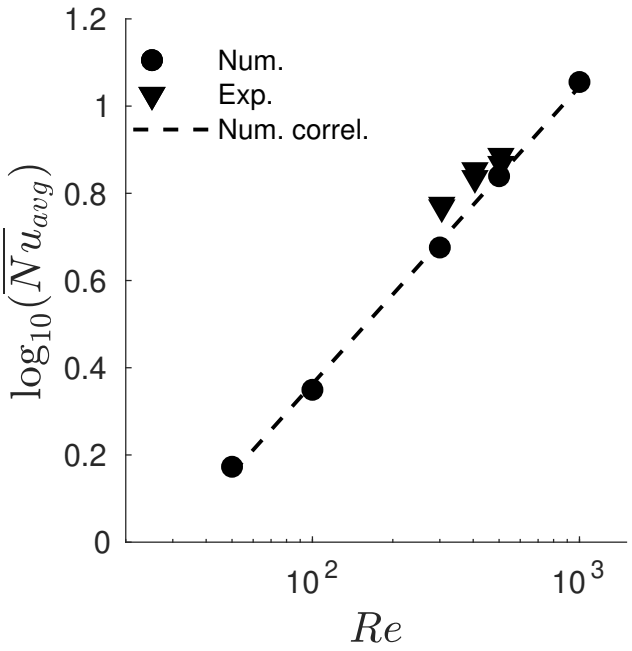

Figure 6.13: Nusselt number correlation with Reynolds number for the slotted configuration. The dashed line corresponds to the correlation presented in Eq. 6.3. The triangles correspond to the experimental points presented in [20] for an open configuration at $Sk = 12.7$ (JFC $= 3.15$).

6.2.2 Circular configuration

The instantaneous local Nusselt number at the hot wall is also shown for the circular configuration in Figs. 6.14, 6.15, 6.16 and 6.17 for various phase instants at $Re = 50$ and $Re = 500$ along with preliminary results at $Re = 100$ and $Re = 300$. The thermal footprint can also be clearly seen on the hot wall and intensifies with the Reynolds number, as expected. Moreover, the maximum heat transfer also occurs at the moment of the impingement ($t = \tau/4$) lasting until the suction cycle at $t = \tau/2$. The first striking difference between the two Reynolds numbers is that the heat transfer is completely symmetric at $Re = 50$ and $Re = 100$, which is indicative of laminar flow. This fact does not occur for $Re = 300$ or $Re = 500$, nor for the slotted configuration at any of the Reynolds numbers studied. This fact is due to the lack of trailing jet and Kelvin-Helmholtz instabilities in the flow at $Re < 300$. In contrast, the effect of the small structures generated by the Kelvin-Helmholtz instability are seen in the footprint at $Re > 100$, more clearly at $Re = 500$. A characteristic of the circular configuration is that the highest heat transfer occurs at the jet centerline and then spreads radially on the heated wall. This is a clear contrast with the slotted configuration that presents a more homogeneous footprint. Analogously to the span-wise average on the slotted configuration, when averaging the signal the effect of this instabilities is lost and a symmetric distribution of the Nusselt number is achieved.

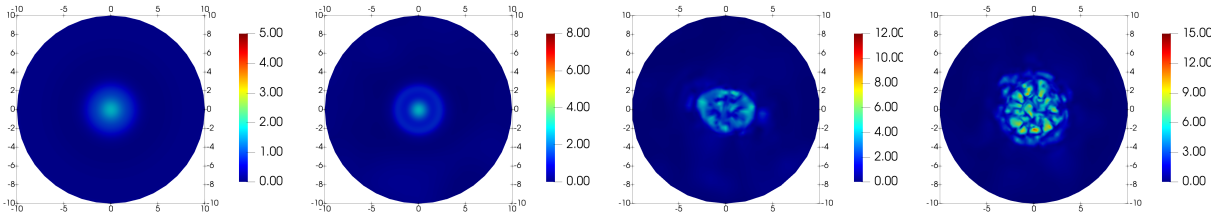

(a) $Re = 50$. (b) $Re = 100$. (c) $Re = 300$. (d) $Re = 500$.

Figure 6.14: Instantaneous local Nusselt number at the hot wall for the circular configuration at phase $t = 0$ and all the Reynolds numbers considered.

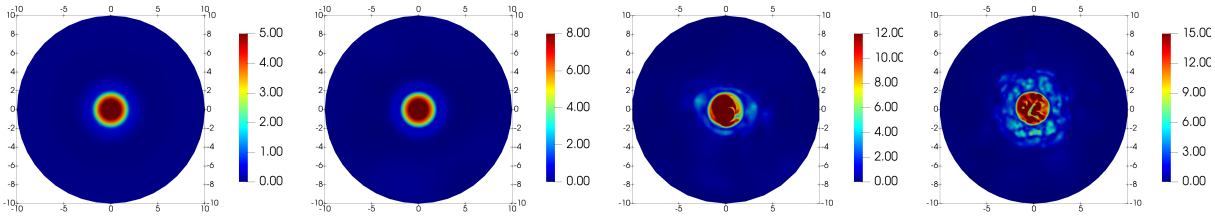

(a) $Re = 50$. (b) $Re = 100$. (c) $Re = 300$. (d) $Re = 500$.

Figure 6.15: Instantaneous local Nusselt number at the hot wall for the circular configuration at phase $t = \tau/4$ and all the Reynolds numbers considered.

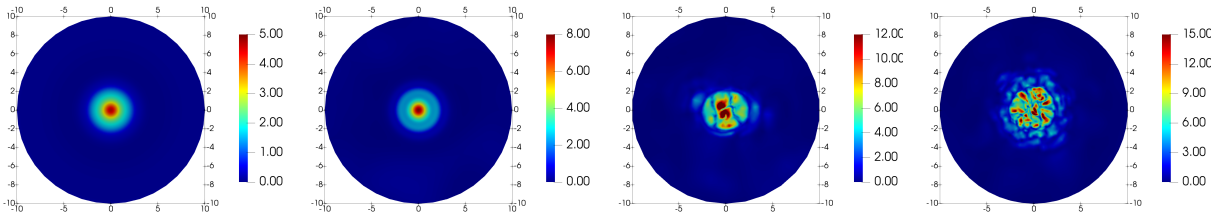

(a) $Re = 50$. (b) $Re = 100$. (c) $Re = 300$. (d) $Re = 500$.

Figure 6.16: Instantaneous local Nusselt number at the hot wall for the circular configuration at phase $t = \tau/2$ and all the Reynolds numbers considered.

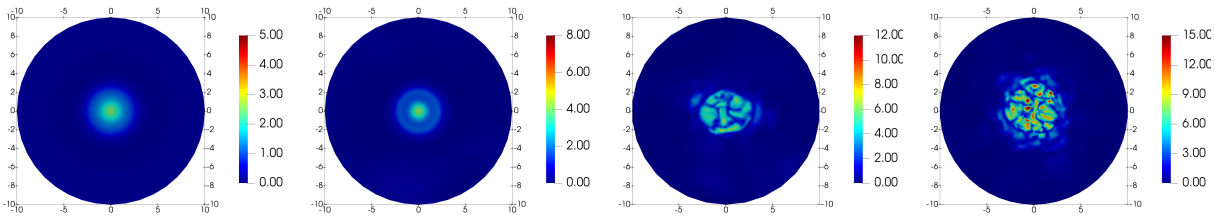

(a) $Re = 50$. (b) $Re = 100$. (c) $Re = 300$. (d) $Re = 500$.

Figure 6.17: Instantaneous local Nusselt number at the hot wall for the circular configuration at phase $t = 3\tau/4$ and all the Reynolds numbers considered.

The time and radial averaged local Nusselt number ($\overline{Nu}$) is shown in Fig. 6.18 for the circular configuration. It is presented for each Reynolds number studied. The effect of the Reynolds number in the heat transfer performance can be observed. Moreover, it can also be seen that the heat transfer peak is located at the jet centerline and rapidly decays. This effect is related to what is mentioned in Section 5.2 and Section 5.3: the circular configuration does not present a clear θ_s vortex that sweeps the hot wall. Instead, θ_1 sweeps the hot wall, however, separation from the heated wall occurs at a lower $\widehat{x}_1$ in the circular configuration. As much of the turbulence is concentrated near the jet vicinity, so is the Nusselt number.

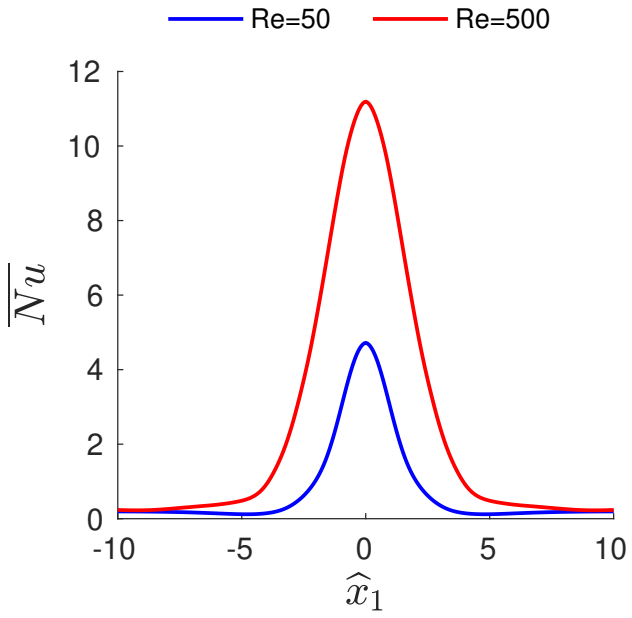

Figure 6.18: Time averaged Nusselt number for the circular configuration at $Re = 50$ and $Re = 500$.

6.3 Comparison of the slotted and circular configurations

The results in Section 6.1 and Section 6.2 also show differences on the temperature field and heat transfer performance between the two cavity configurations studied. A closer look on the time variation of the temperature at the SJA orifice at $Re = 500$, shown in Fig. 6.19, reveals that although the mean temperature of the SJA orifice is similar for both cavity configurations, the peak to peak variations of temperature are higher in the circular cavity configuration. In the slotted configuration, the small structures ingested interact with the fluid ingested resulting in softer variations of the SJA outlet temperature. This is related with the increased mixing in the slotted configuration described in Section 5.3. The temporal dynamics of the temperature signal at the low velocity areas is similar, with very low amplitudes and almost no mixing. The circular synthetic jet does not affect the zones further from the jet vicinity, hence the spectra of the signals mostly show background noise.

The thermal footprint at the hot wall is also different for both configurations at the Reynolds numbers studied. Mixing and dispersion over the hot wall is clearly visible in the slotted configuration, even for $Re = 50$. In the circular configuration, however, the thermal footprint is mostly concentrated in the vicinity of the jet centerline and does not spread much further. This is the result of the flow dynamics explained in Chapter 5. Vortex shedding and the appearance of θ_s vortex in the slotted configuration increase the turbulent transition and the jet mixing, resulting in a wider jet width. Hence the thermal footprint is also wider. The small structures generating the trailing jet in the circular configuration are mostly concentrated in the vicinity of the jet centerline, thus a narrower jet width is produced and a smaller thermal footprint is obtained.

These ideas are further strengthened when plotting the time (and span-wise) averaged Nusselt number at the hot wall for both configurations, as in Fig. 6.20. It can be seen that the profiles for the circular configuration are narrower than those for the slotted configuration. When the jet is turbulent, e.g., at $Re = 500$, the turbulent kinetic energy is mostly concentrated in the jet centerline and induces high mixing, which results in a higher Nu at the jet centerline. Whereas for the slotted configuration, the turbulent kinetic energy is more spread within the jet and results in a flatter Nu profile at the impingement. Moreover, the effect of θ_s yields a slower decay of Nu than in the circular configuration. At $Re = 50$ the jet is laminar with almost no mixing for the circular configuration, with no visible trailing jet. This effect visibly reduces Nu at the impingement, compared with the slotted configuration, in which some mixing occurs.

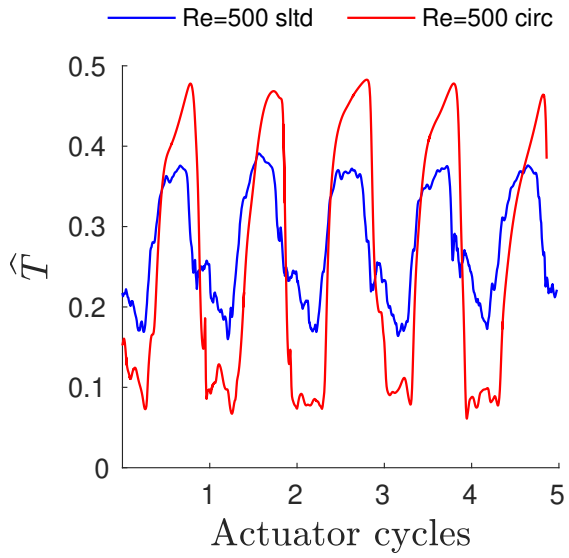

Figure 6.19: Comparison of the time evolution of the temperature at the SJA outlet for both configurations.

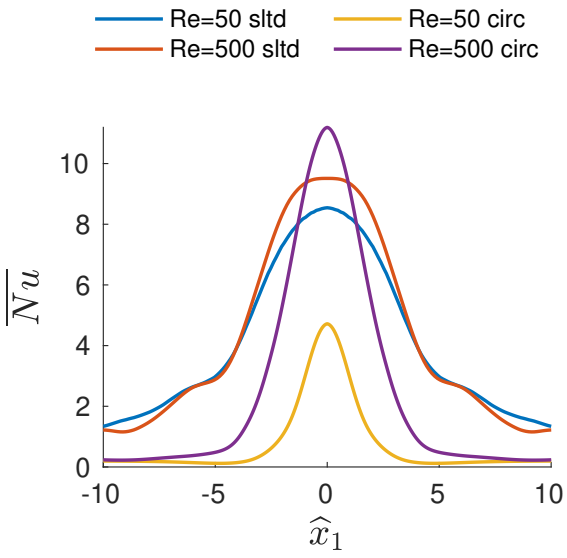

Figure 6.20: Time (and span-wise) averaged Nusselt number for both configurations at $Re = 50$ and $Re = 500$.

7

Conclusions and Future Work

This chapter summarizes the results presented in this dissertation and presents some points that can be the target of further work and research. Finally, it includes a relation of the publications derived from this thesis.

7.1 Conclusions

The dynamics of the flow and the heat transfer capabilities of synthetic jet actuators (SJA) enclosed between two large parallel plates and impinging into a hot plate have been studied. Two different geometric configurations have been considered: a slotted and a circular jet. The former has been analyzed at $Re = 50;\ 100;\ 300;\ 500;\ 1,000$ and JFC $= 3$, while the latter has been analyzed at $Re = 50$ and 500 with the same JFC. For the lower Reynolds numbers DNS of the flow have been performed, whereas for $Re > 100$, high fidelity large-eddy simulations (LES) using the WALE SGS have been carried out. The numerical methodology used in this work is based on state-of-the-art energy preserving spatial discretization and high order temporal integration schemes. Convergence to the solution has been thoroughly validated using successive refinements on the computational grids. The objective was to provide insight on the flow and heat transfer capabilities of synthetic jets and to analyze the influence of the geometrical configuration on the jet flow.

A second objective was to present a reliable and simplified model of the SJA with boundary conditions that take into account the interaction of the fluid inside the actuator and the moving membrane.

Therefore, the governing parameters have been analyzed and expressed in terms of design parameters, such as driving frequency, amplitude and geometric relations. In this formulation, which accounts for the time-periodic movement of the SJA membrane using an ALE method, the actuator frequency f_0 and velocity U_0 are coupled. Under this circumstances, a mathematical expression is found that confirms what has already been observed experimentally: the jet formation only depends on the amplitude and the geometric configuration of the actuator (Eq. 2.42)

$$\text{JFC} = \frac{2}{\pi}\left(\frac{\overline{A}}{d}\right)\left(\frac{S_W}{S_d}\right).$$

Moreover, it allows for a detailed study both inside and outside the actuator cavity and to obtain an accurate representation of the velocity and temperature at the SJA outlet.

Two simplified actuator geometries, a rectangular with a homogeneous domain in the x_3 direction and a circular, have been studied with an orifice to cavity height of $H/d = 5$. The resulting flows are quite complex, and a large number of actuator cycles needs to be integrated in order to reach a statistically stationary state. It has been found that, for the studied configurations, the far flow field is dominated by frequencies about 7 times lower than the driving frequency, resulting in the overall system having slow temporal scales. The flow is inherently three dimensional in the slotted configuration, even for the lowest Reynolds numbers considered. This has an effect on the size of the vortices and the Nusselt number.

The differences on the jet morphology of the two studied configurations have been thoroughly identified by means of the Q-criterion and the swirling and shearing strength parameter (Figs. 5.1 and 5.5 to Figs. 5.4 and 5.8 and Fig. 5.19). Fundamental differences are found between the flow of both configurations. The vortex dipoles of the slotted configuration have been found to lose coherence early at the roll-up stage, thus creating a highly turbulent jet that advects downstream towards the impingement while it widens on the cross-stream direction. Its external flow is dominated by two major structures, ϑ_1 and ϑ_2, that have counterparts inside the actuator, ϑ_3 and ϑ_4. The largest of them, (i.e., ϑ_1), has been identified in both open and enclosed configurations and is the result of the coalescence of the vortices expelled by the actuator. However, the second structure (i.e., ϑ_2), is specific of the slotted enclosed configuration and appears as a result of the flow interacting with the bottom wall. It plays a major role in limiting the jet's heat transfer enhancement mechanism, which results in a higher decay of the Nusselt number far from the stagnation point when compared with the slotted open configuration. On the other hand, the vortex rings in the circular configuration are able to maintain their coherence, even after the impingement. The trailing jet contains most of the jet's turbulent energy. This results in less jet widening and vortex interaction and a more intense impingement on the jet centerline, as evidenced by the Nusselt number. The circular configuration also shows the ϑ_1 vortex and also another vortex, ϑ_0, that corresponds to the impinging vortex of

the previous cycle. In addition, the external flow of the circular configuration is also dominated by the trailing jet and the potential core. The analysis of the position of the vortices advected from the actuator orifice on both configurations yields that the vortices on the circular configuration reach the impingement area before their slotted counterparts. On the slotted configuration, the interaction of the vortex advected from the orifice, Θ_1 with the vortex expelled on the previous cycle Θ_0 delays the downstream motion of Θ_1. This is in good agreement with the circular jet being concentrated in the jet centerline and having a lower critical JFC than the slotted.

The effects of the flow morphologies described on the heat transfer have been identified in the temperature field and the Nusselt number. The Nusselt number at the jet centerline for the circular configuration is higher than the slotted, however, the decay on the Nusselt is lower for the slotted configuration. This has been found to be the effect of the circular jet having its energy more concentrated on the jet centerline, while the slotted is more spread with a different vortical configuration. The model proposed allows to compute accurate velocity and temperature profiles at the actuator orifice (slotted Figs. 5.15 and 6.2, circular Figs. 5.18 and 6.5), values that are generally unknown when considering other SJA models, and that have an impact on the heat transfer. The analysis of the conditions at the outlet has shown that:

- the outlet dimensionless temperature is about 1/10 to 1/5 (even about 1/2.5 in the circular configuration) of the temperature difference between the hot and cold plates depending on the Reynolds number;
- there is a similarity between the different Reynolds numbers considered at the same JFC;
- a strong asymmetry appears in the flow between ejection and suction phases;
- uniform-like temperature outlet profiles have been obtained for $Re > 100$, thus supporting the validity of a uniform outlet temperature model.

Due to the aforementioned outlet jet temperatures, the imposition of an outlet temperature equal to the cold temperature in numerical simulations might result in an overestimation of the Nusselt number in the hot wall. Correlations of outlet dimensionless temperature (Eq. 6.1)

$$\left\langle \widehat{T} \right\rangle = 0.075 Re^{0.137},$$

and Nusselt number (Eq. 6.3)

$$\frac{\overline{Nu}_{avg}}{Pr^{0.42}} = 0.115 Re^{0.682},$$

have been obtained for the slotted enclosed configuration and an orifice to plate ratio of $H/d = 5$. The former can be used as a model for the outlet jet temperature in the slotted closed configuration for the aforementioned height ratio.

7.2 Future Work

The following discussion presents some points that are target of further research or might be worth of investigation. They aim to further expand the model presented in this dissertation and further explore the synthetic jet flow governing parameters, as well as geometric implications (e.g., orifice shapes other than slotted and circular).

Circular configuration. More Reynolds numbers can be analyzed for the circular configuration (e.g., $Re = 100$, 300, and 1000). Correlations of outlet temperature and Nusselt number could then be obtained that could work as a model for the outlet jet temperature. Then, these correlations and models could be compared with those presented in this work and in [17].

Another challenge with the circular configuration is to be able to match the Reynolds numbers achieved in experimental analysis with high fidelity numerical simulations. This would allow for validating the numerical results with experimental data.

Analysis at different JFC. The jet formation criteria plays an important role in the morphology of the jet and its interaction with the external flow (be it a crossflow or an impingement). Some implications of changing the jet formation criteria have been analyzed in this work and a brief description is provided at the end of Section 2.4.

Further research on this topic can benefit in providing further insight into the reason behind the change of morphology of the jet, for both the slotted and circular configurations, and its implications on the Nusselt number. The correlations presented on this work could be extended in order to include the effect of the Reynolds number as well as the jet formation criteria.

Proper Ortogonal Decomposition (POD) and Dynamic Mode Decomposition (DMD). Throughout this work, the high computational cost of the simulations performed is stressed. On the one hand, high fidelity models such as LES used in this work require quite a dense mesh, not as dense as DNS would require but much denser than RANS. On the other hand, a large number of actuator cycles are required to find a stationary state. Even with the techniques mentioned in this work, converging to a solution is expensive.

For this reason, methods for obtaining simplified approximate models for fluid flows seem convenient in this case. These methods, such as POD or DMD, can be fed with the numerical simulations performed in this work in order to obtain a simpler surrogate model. Moreover, these models can provide insight about the fundamental mechanisms that describe a particular flow [110], thus they

might be used to analyze the reason behind the flow differences between the two studied configurations.

7.3 Publications derived of this work

The following section contains a relation of publications derived of this dissertation and that have been authored by the present author.

Journal papers

A. Miró, M. Soria, J. C. Cajas, and I. Rodríguez, "Numerical study of heat transfer from a synthetic impinging jet with a detailed model of the actuator membrane," Int. J. Therm. Sci., vol. 136, no. October 2018, pp. 287--298, Feb. 2019.

Conference papers

A. Miró, M. Soria, C. Moulinec, J. C. Cajas, and Y. Fournier, "Numerical investigations on rectangular and circular synthetic jet impingement," in Tenth International Conference on Computational Fluid Dynamics (ICCFD10), 2018, pp. 1--18.

A. Miró, M. Soria, I. Rodríguez, and J. C. Cajas, "Numerical Investigations of Synthetic Jet Actuators," in Proceedings of the 17th International Conference on Computational and Mathematical Methods in Science and Engineering, 2017, pp. 1--12.

Conference posters

A. Miró, M. Soria, J. M. Bergada, and D. del Campo, "Simulation of fluidic oscillators with Code_Saturne." EDF, Code_Saturne User's meeting, Paris, 2016.

Bibliography

[1] S G. Sawant, B. George, L.S. Ukeiley, and D.P. Arnold. Microfabricated Electrodynamic Synthetic Jet Actuators. *Journal of Microelectromechanical Systems*, 27(1):95--105, 2018.

[2] G. Minelli, E.A. Hartono, V. Chernoray, L. Hjelm, and S. Krajnović. Aerodynamic flow control for a generic truck cabin using synthetic jets. *Journal of Wind Engineering and Industrial Aerodynamics*, 168:81--90, 2017.

[3] Q. Zhao, Y. Ma, and G. Zhao. Parametric analyses on dynamic stall control of rotor airfoil via synthetic jet. *Chinese Journal of Aeronautics*, 30(6):1818--1834, 2017.

[4] K. Bauer, C. Karch, A. Heilmann, and M. Blechschmidt. Novel Design of a Synthetic Jet Actuator for Flow Control. In *55th AIAA Aerospace Sciences Meeting*, pages 1--10, 2017.

[5] A. Glezer and M. Amitay. Synthetic Jets. *Annual Review of Fluid Mechanics*, 34:503--529, 2002.

[6] L. Kral, J. Donovan, A. Cain, and A. Cary. Numerical simulation of synthetic jet actuators. In *4th Shear Flow Control Conference*, volume 97-1824, page 15, 1997.

[7] S. Mallinson, G. Hong, and J. Reizes. Some characteristics of synthetic jets. In *30th Fluid Dynamics Conference*, volume 3651, page 10, 1999.

[8] S. G. Mallinson, C. Y. Kwok, and J. A. Reizes. Numerical simulation of micro-fabricated zero mass-flux jet actuators. *Sensors and Actuators, A: Physical*, 105(3):229--236, 2003.

[9] C.L. Rumsey, T.B. Gatski, W.L. Sellers III, V.N. Vasta, and S.A. Viken. Summary of the 2004 Computational Fluid Dynamics Validation Workshop on Synthetic Jets. *AIAA Journal*, 44: 194--207, 2006.

[10] B. L. Smith and A. Glezer. The formation and evolution of synthetic jets. *Physics of Fluids*, 10(9):2281--2297, 1998.

[11] U. Ingård and S. Labate. Acoustic circulation effects and the nonlinear impedance of orifices. *The Journal of the Acoustical Society of America*, 22(2):211--218, 1950.

[12] E.P. Mednikov and B.G. Novitskii. Experimental study of intense acoustic streaming. *Soviet Physics Acoustics*, 21:245--249, 1975.

[13] IV Lebedeva. Experimental study of acoustic streaming in the vicinity of orifices. *Soviet Physics Acoustics*, 26:599--602, 1980.

[14] L.N. Cattafesta III and M. Sheplak. Actuators for active flow control. *Annual Review of Fluid Mechanics*, 43:247--272, 2011.

[15] R. B. Kotapati, Mittal, and L. N. Cattafesta III. Numerical study of a transitional synthetic jet in quiescent external flow. *Journal of Fluid Mechanics*, 581:287--321, 2007.

[16] L. Silva-Llanca and A. Ortega. Vortex dynamics and mechanisms of heat transfer enhancement in synthetic jet impingement. *International Journal of Thermal Sciences*, 112:153--164, 2017.

[17] A. Miró, Manel Soria, J.C. Cajas, and I. Rodríguez. Numerical study of heat transfer from a synthetic impinging jet with a detailed model of the actuator membrane. *International Journal of Thermal Sciences*, 136:287--298, 2019.

[18] M. A. Feero, P. Lavoie, and P. E. Sullivan. Influence of cavity shape on synthetic jet performance. *Sensors and Actuators, A: Physical*, 223:1--10, 2015.

[19] A. Miró, M. Soria, C. Moulinec, J. C. Cajas, and Y. Fournier. Numerical investigations on rectangular and circular synthetic jet impingement. In *Tenth International Conference on Computational Fluid Dynamics (ICCFD10)*, pages 1--18, 2018.

[20] L. Silva-Llanca, A. Ortega, and I. Rose. Experimental convective heat transfer in a geometrically large two-dimensional impinging synthetic jet. *International Journal of Thermal Sciences*, 90:339--350, 2015.

[21] O. Ghaffari, S.A. Solovitz, M. Ikhlaq, and M. Arik. An investigation into flow and heat transfer of an ultrasonic micro-blower device for electronics cooling applications. *Applied Thermal Engineering*, 106:881--889, 2016.

[22] Y. Wang, G. Yuan, Y Yoon, M.G. Allen, and S.A. Bidstrup. Large eddy simulation (LES) for synthetic jet thermal management. *International Journal of Heat and Mass Transfer*, 49: 2173--2179, 2006.

[23] J. Uribe, A. Revell, C. Moulinec, V. Kitsios, A. Ooi, and J. Soria. COMPUTATION OF FLOW AROUND A NACA 0015 AEROFOIL WITH ZNMF JET CONTROL: POTENTIAL SAVINGS OF AN UNSTRUCTURED MESH? In *Sixth International Symposium on Turbulence and Shear Flow Phenomena*, pages 1281--1286, 2009.

[24] D. Velasco, O. López Mejia, and S. Laín. Numerical simulations of active flow control with synthetic jets in a Darrieus turbine. *Renewable Energy*, 113:129--140, 2017.

[25] M. Hatami, F. Bazdidi-Tehrani, A. Abouata, and A. Mohammadi-Ahmar. Investigation of geometry and dimensionless parameters effects on the flow field and heat transfer of impingement synthetic jets. *International Journal of Thermal Sciences*, 127:41--52, 2018.

[26] O. Ghaffari, Stephen A. Solovitz, and M. Arik. An investigation into flow and heat transfer for a slot impinging synthetic jet. *International Journal of Heat and Mass Transfer*, 100:634--645, 2016.

[27] J. Kordík, V. Timchenko, and N.A. Ismail. The predominant effect of stroke length on velocity profiles at the exit of axisymmetric synthetic jet actuators. *International Journal of Heat and Fluid Flow*, 66:197--208, 2017.

[28] C.S. Greco, G. Paolillo, A. Ianiro, G. Cardone, and L. de Luca. Effects of the stroke length and nozzle-to-plate distance on synthetic jet impingement heat transfer. *International Journal of Heat and Mass Transfer*, 117:1019--1031, 2018.

[29] I. Rodríguez, O. Lehmkuhl, R. Borrell, and A. Oliva. Direct numerical simulation of a NACA0012 in full stall. *International Journal of Heat and Fluid Flow*, 43:194--203, 2013.

[30] J. E. Cater and J. Soria. The evolution of round zero-net-mass-flux jets. *Journal of Fluid Mechanics*, 472:167--200, 2002.

[31] Y. Utturkar, R. Holman, R. Mittal, B. Carroll, M. Sheplak, and L.N. Cattafesta III. A Jet Formation Criterion for Synthetic Jet Actuators. In *41st Aerospace Sciences Meeting and Exhibit*, pages 1--9, 2003.

[32] R. Holman, Y. Utturkar, R. Mittal, B. L. Smith, and L. N. Cattafesta III. Formation Criterion for Synthetic Jets. *AIAA Journal*, 43(10):2110--2116, 2005.

[33] L. D. Mangate and M. B. Chaudhari. Heat transfer and acoustic study of impinging synthetic jet using diamond and oval shape orifice. *International Journal of Thermal Science*, 89: 100--109, 2015.

[34] C.M. Crispo, C.S. Greco, F. Avallone, and G. Cardone. On the flow organization of a chevron synthetic jet. *Experimental Thermal and Fluid Science*, 82:136--146, 2017.

[35] L. Silva-Llanca, J. Paul d'Alençon, and A. Ortega. Vortex dynamics-driven heat transfer and flow regime assessment in a turbulent impinging synthetic jet. *International Journal of Thermal Sciences*, 121:278--293, 2017.

[36] Q. Gallas. *On the Modeling and Design of Zero-Net Mass Flux Actuators*. PhD thesis, University of Florida, 2005.

[37] Daniel T. H. New and Simon C. M. Yu. *Vortex Rings and Jets*. Springer Singapore, 2015.

[38] Y.D. Afanasyev. Formation of vortex dipoles. *Physics of Fluids*, 18(3):1--9, 2006.

[39] S.I. Voropayev, Y.D. Afanasyev, and I.A. Filippov. Horizontal jets and vortex dipoles in a stratified fluid. *Journal of Fluid Mechanics*, 227:543--566, 1991.

[40] C.Y. Lee and D.B. Goldstein. Two Dimensional Synthetic Jet Simulation. *AIAA Journal*, 40 (3):510--516, 2002.

[41] C. Yao, F. J. Chen, and D. Neuhart. Synthetic Jet Flowfield Database for Computational Fluid Dynamics Validation. *AIAA Journal*, 44:3153--3157, 2006.

[42] J. C. R. Hunt, A. A. Wray, and P. Moin. Eddies, Streams, and Convergence Zones in Turbulent Flows. In *Proceedings of the Summer Program 1988*, 1989.

[43] J.O. Dabiri, S.P. Colin, J.H. Costello, and M. Gharib. Flow patterns generated by oblate medusan swimmers: in situ observation and analysis. *Journal of Experimental Biology*, 208: 1257--1265, 2005.

[44] K. Mohseni and R. Mittal. *Synthetic jets: fundamentals and applications*. CRC Press, 2014.

[45] C. S. Greco, G. Cardone, and J. Soria. On the behaviour of impinging zero-net-mass-flux jets. *Journal of Fluid Mechanics*, 810:25--59, 2017.

[46] M. Gharib, E. Rambod, and K. Shariff. A universal time scale for vortex ring formation. *Journal of Fluid Mechanics*, 360:121--140, 1998.

[47] P. Valiorgue, T. Persoons, A. McGuinn, and D. B. Murray. Heat transfer mechanisms in an impinging synthetic jet for a small jet-to-surface spacing. *Experimental Thermal and Fluid Science*, 33:597--603, 2009.

[48] A. Pavlova and M. Amitay. Electronic Cooling Using Synthetic Jet Impingement. *Journal of Heat Transfer*, 128(9):897--907, 2006.

[49] G. Eschmann, A. Kuntze, W. Uffrecht, E. Kaiser, and S. Odenbach. Experimental and numerical investigation of heat transfer coefficients in gaseous impinging jets. First test of a recent sensor concept for steady and unsteady flow. *International Journal of Thermal Sciences*, 96:290--304, 2015.

[50] M. A. Pakhomov and V. I. Terekhov. RANS modeling of flow structure and turbulent heat transfer in pulsed gas-droplet mist jet impingement. *International Journal of Thermal Sciences*, 100:284--297, 2016.

[51] T. Guan, J.Z. Zhang, and Y. Shan. Convective heat transfer by a row of tab-excited impinging jets on a wedge-shaped concave surface. *International Journal of Thermal Sciences*, 100: 37--53, 2016.

[52] L. Silva-Llanca and A. Ortega. Convective Heat Transfer in an Impinging Synthetic Jet : a Numerical Investigation of a Canonical Geometry. *Journal of Heat Transfer*, 135:7--9, 2013.

[53] Y. Utturkar, M. Arik, C. E. Seeley, and M. Gursoy. An Experimental and Computational Heat Transfer Study of Pulsating Jets. *Journal of Heat Transfer*, 130:1--10, 2008.

[54] K. Habibi, S. Amiri, and M. Ashjaee. Study of mixed convection characteristics of confined planar jet impingement using the direct temperature gradient interferometric method. *International Journal of Thermal Sciences*, 71:205--215, 2013.

[55] J. Vukasinovic and A. Glezer. Spot-Cooling by Confined, Impinging Synthetic Jet. In *Heat Transfer: Volume 3*, pages 469--476, 2003.

[56] H. Xia and N. Qin. Dynamic Grid and Unsteady Boundary Conditions for Synthetic Jets Flow. In *43rd AIAA Aerospace Sciences Meeting and Exhibit*, pages 1--9, 2005.

[57] D. P. Rizzetta, M. R. Visbal, and M. J. Stanek. Numerical Investigation of Synthetic-Jet Flowfields. *AIAA Journal*, 37(8):919--927, 1999.

[58] E. Montazer, M. Mirzaei, E. Salami, T. A. Ward, F. I. Romli, and S. N. Kazi. Optimization of a synthetic jet actuator for flow control around an airfoil. *IOP Conference Series: Materials Science and Engineering*, 152(1):012023, 2016.

[59] W. Zhang and R. Samtaney. A direct numerical simulation investigation of the synthetic jet frequency effects on separation control of low-Re flow past an airfoil. *Physics of Fluids*, 27 (5):055101, 2015.

[60] R. Raju, E. Aram, R. Mittal, and L. Cattafesta. Reduced-Order Models of Zero-Net Mass-Flux Jets for Large-Scale Flow Control Simulations. In *26th AIAA Applied Aerodynamics Conference*, pages 1--14, 2008.

[61] A. Miró, M. Soria, I. Rodríguez, and J. C. Cajas. Numerical Investigations of Synthetic Jet Actuators. In *Proceedings of the 17th International Conference on Computational and Mathematical Methods in Science and Engineering*, pages 1--12, 2017.

[62] L.D. Kral. Active flow control technology. In *ASME FED, Technical Brief*, pages 1--28, 2000.

[63] D. Greenblatt and I.J. Wygnanski. The control of flow separation by periodic excitation. *Progress in Aerospace Sciences*, 36(7):487--545, 2000.

[64] G.B. Schubauer and H.K. Skramstad. Laminar-boundary-layer oscillations and transition on a flat plate. Technical report, National Aeronautics and Space Administration Washington DC, 1948.

[65] Sebastian Fricke, Vlad Ciobaca, Jochen Wild, and David Norman. *Advances in Simulation of Wing and Nacelle Stall*. Springer International Publishing, 2016.

[66] N.A. Buchmann, C. Atkinson, and J. Soria. Influence of znmf jet flow control on the spatio-temporal flow structure over a naca-0015 airfoil. *Experiments in Fluids*, 54(3):1--14, 2013.

[67] P. Spalart, L. Hedges, M. Shur, and A. Travin. Simulation of active flow control on a stalled airfoil. *Flow, Turbulence and Combustion*, 71(1-4):361--373, 2003.

[68] D. You and P. Moin. Active control of flow separation over an airfoil using synthetic jets. *Journal of Fluids and Structures*, 24(8):1349--1357, 2008.

[69] R. Rudnik. Stall behaviour of the eurolift high lift configurations. In *46th AIAA Aerospace Sciences Meeting and Exhibit*, page 836, 2008.

[70] D.S. Kercher, J.B. Lee, O. Brand, M.G. Allen, and A. Glezer. Microjet cooling devices for thermal management of electronics. *IEEE Transactions on Components and Packaging Technologies*, 26(2):359--366, 2003.

[71] F.O. Edis, N. Erbas, O. Baysal, and A.R. Aslad. Micro Synthetic Jets And Their Interaction With A Cross Flow In Slip Regime. *Recent Advances in Space Technologies*, pages 582--586, 2003.

[72] T. T. Chandratilleke and D. Rakshit. Thermal performance of a double-action pulsed jet CPU cooler. *Proceedings of the 2013 IEEE 15th Electronics Packaging Technology Conference, EPTC 2013*, pages 353--357, 2013.

[73] Y. Yu, T.W. Simon, M. Zhang, T. Yeom, M.T. North, and T. Cui. Enhancing heat transfer in air-cooled heat sinks using piezoelectrically- driven agitators and synthetic jets. *International Journal of Heat and Mass Transfer*, 68:184--193, 2014.

[74] N. Erbas, M. Koklu, and O. Baysal. Synthetic Jets for Thermal Management of Microelectronic Chips. *Proceedings of IMECE2005*, pages 1--5, 2005.

[75] Barcelona Supercomputing Center. MareNostrum3 User's Guide. `https://www.bsc.es/support/MareNostrum3-ug.pdf`, 2016.

[76] Barcelona Supercomputing Center. MareNostrum4 User's Guide. `https://www.bsc.es/user-support/mn4.php`, 2017.

[77] Intel Corporation. Intel products catalog. `https://www.intel.com/content/www/us/en/homepage.html`.

[78] C.Y.Y. Lee, M.L. Woyciekoski, and J.B. Copetti. Experimental study of synthetic jets with rectangular orifice for electronic cooling. *Experimental Thermal and Fluid Science*, 78:242--248, 2016.

[79] Y. Chen, S. Liang, K. Aung, A. Glezer, and J. Jagoda. Enhanced mixing in a simulated combustor using synthetic jet actuators. In *AIAA, Aerospace Sciences Meeting and Exhibit, 37 th, Reno, NV*, 1999.

[80] H. Wang and S. Menon. Fuel-air mixing enhancement by synthetic microjets. *AIAA Journal*, 39(12):2308--2319, 2001.

[81] Y. H. Liu, S. Y. Tsai, and C. C. Wang. Effect of driven frequency on flow and heat transfer of an impinging synthetic air jet. *Applied Thermal Engineering*, 75:289--297, 2015.

[82] J. Agashe, D. Arnold, and L. Cattafesta. Development of Compact Electrodynamic Zero-Net Mass-Flux Actuators. In *47th AIAA Aerospace Sciences Meeting including The New Horizons Forum and Aerospace Exposition*, pages 2009--1308, 2009.

[83] R. D. Blevins and R. Plunkett. Formulas for natural frequency and mode shape. *Journal of Applied Mechanics*, 47:461, 1980.

[84] P. Mane, K. Mossi, A. Rostami, R. Bryant, and N. Castro. Piezoelectric Actuators as Synthetic Jets: Cavity Dimension Effects. *Journal of Intelligent Material Systems and Structures*, 18 (11):1175--1190, 2007.

[85] F. Bazdidi-Tehrani, M. Hatami, and A. Abouata. Effects of inlet and outlet boundary conditions on the flow field of synthetic jets. In *Proceedings of the Institution of Mechanical Engineers, Part E: Journal of Process Mechanical Engineering*, volume 231, pages 107--118, 2017.

[86] B. Smith and G. Swift. Synthetic jets at large Reynolds number and comparison to continuous jets. In *15th AIAA Computational Fluid Dynamics Conference*, volume 2001-3030, page 20, 2001.

[87] BSC-CNS. Alya multiphysics code. `http://www.bsc.es/computer-applications/alya-system`, 2014.

[88] F. Archambeau, N. Méchitoua, and M. Sakiz. Code saturne: A finite volume code for the computation of turbulent incompressible flows-industrial applications. *International Journal on Finite Volumes*, 1(1), 2004.

[89] M. Vázquez, G. Houzeaux, S. Koric, A. Artigues, J. Aguado-Sierra, R. Arís, D. Mira, H. Calmet, F. Cucchietti, H. Owen, et al. Alya: Multiphysics engineering simulation toward exascale. *Journal of Computational Science*, 14:15--27, 2016.

[90] Y. Fournier, J. Bonelle, C. Moulinec, Z. Shang, A.G. Sunderland, and J.C. Uribe. Optimizing Code_Saturne computations on Petascale systems. *Computers & Fluids*, 45(1):0045--7930, 2011.

[91] Stephen B. Pope. *Turbulent Flows*. Cambridge University Press, 2000.

[92] W.P. Jones and B.E. Launder. The prediction of laminarization with a two-equation model of turbulence. *International Journal of Heat and Mass Transfer*, 15(2):301--314, 1972.

[93] B.E. Launder and B.I. Sharma. Application of the energy-dissipation model of turbulence to the calculation of flow near a spinning disc. *Letters in Heat and Mass Transfer*, 1(2): 131--137, 1974.

[94] D.C. Wilcox. *Turbulence modeling for CFD*. DCW industries La Canada, CA, 1998.

[95] F.R. Menter, M. Kuntz, and R. Langtry. Ten years of industrial experience with the sst turbulence model. *Turbulence, Heat and Mass Transfer*, 4(1):625--632, 2003.

[96] D. Mira, X. Jiang, C. Moulinec, and D. R. Emerson. Numerical investigation of the effects of fuel variability on the dynamics of syngas impinging jet flames. *Fuel*, 103:646--662, 2013.

[97] D.K. Lilly. A proposed modification of the germano subgrid-scale closure method. *Physics of Fluids A: Fluid Dynamics*, 4(3):633--635, 1992.

[98] F. Nicoud and F. Ducros. Subgrid-scale stress modelling based on the square of the velocity gradient tensor. *Flow, Turbulence and Combustion*, 62:183--200, 1999.

[99] H. Tennekes and J.L. Lumley. *A first course in turbulence*. MIT press, 1972.

[100] R.W.C.P. Verstappen and A.E.P. Veldman. Symmetry-preserving discretization of turbulent flow. *Journal of Computational Physics*, 187(1):343--368, 2003.

[101] F.X. Trias, O. Lehmkuhl, A. Oliva, C.D. Pérez-Segarra, and R.W.C.P. Verstappen. Symmetry-preserving discretization of Navier-Stokes equations on collocated unstructured grids. *Journal of Computational Physics*, 258:246--267, 2014.

[102] O. Lehmkuhl, G. Houzeaux, M. Avila, H. Owen, M. Vazquez, and D. Mira. A low dissipation finite element scheme for the large eddy simulation on complex geometries. In *19h International Conference on Finite Elements in Flow Problems-FEF*, 2017.

[103] S. Charnyi, T. Heister, M.A. Olshanskii, and L.G. Rebholz. On conservation laws of Navier–Stokes Galerkin discretizations. *Journal of Computational Physics*, 337:289--308, 2017.

[104] F. Capuano, G. Coppola, L. Rández, and L. De Luca. Explicit Runge – Kutta schemes for incompressible flow with improved energy-conservation properties. *Journal of Computational Physics*, 328:86--94, 2017.

[105] F.X. Trias and O. Lehmkuhl. A Self-Adaptive Strategy for the Time Integration of Navier-Stokes Equations. *Numerical Heat Transfer, Part B: Fundamentals*, 60(2):116--134, 2011.

[106] D. Pastrana, J.C. Cajas, O. Lehmkuhl, I. Rodríguez, and G. Houzeaux. Large-eddy simulations of the vortex-induced vibration of a low mass ratio two-degree-of-freedom circular cylinder at subcritical Reynolds numbers. *Computers & Fluids*, 0:1--15, 2018.

[107] J. Jeong and F. Hussain. On the identification of a vortex. *Journal of Fluid Mechanics*, 285: 69--94, 1995.

[108] A. McGuinn, R. Farrelly, T. Persoons, and D. B. Murray. Flow regime characterisation of an impinging axisymmetric synthetic jet. *Experimental Thermal and Fluid Science*, 47:241--251, 2013.

[109] R.J. Adrian, K.T. Christensen, and Z.C. Liu. Analysis and interpretation of instantaneous turbulent velocity fields. *Experiments in fluids*, 29(3):275--290, 2000.

[110] Clarence W. Rowley and Scott T.M. Dawson. Model Reduction for Flow Analysis and Control. *Annual Review of Fluid Mechanics*, 49(1):387--417, 2017.